

University of Naples Federico II

Industrial Engineering Department



**Doctoral Dissertation:**

Production of Selective Solar Absorbers for Evacuated Thermal  
Collectors and Measurements of their Radiative Properties

**Tutor**

Prof. Eng. Marilena Musto

**Supervisor**

Dr. Roberto Russo

**Candidate:**

Dr. Carmine D'Alessandro

XXXIV PhD Cycle

# Index

Nomenclature .....	3
Introduction .....	5
1. Technologies of the Evacuated Flat Panel.....	7
1.1. Vacuum Envelopes for Solar Thermal Collectors.....	7
1.2. Selective Solar Absorbers Fundamentals .....	12
1.3. Optical Characterization of Selective Solar Absorbers .....	17
2. Measurement of Radiative Properties Under Realistic Operational Conditions.....	23
2.1. Experimental setup of the novel calorimetric test facility .....	25
2.2. Design of the LED-based Solar Simulator .....	27
2.3. Calorimetric Equation.....	37
2.4. Measurement Algorithm of the Calorimetric Test .....	40
2.5. Experimental results: Optical and Calorimetric Approaches .....	42
2.6. Numerical 3D Thermal Simulations .....	47
3. Production of Novel Selective Solar Absorbers.....	52
3.1. Optics Fundamentals for the Multilayer Selective Coating .....	52
3.2. Proposed Architecture of the Multilayer Absorber.....	55
3.3. Basics of Magnetron Sputtering.....	58
3.4. Laboratory Sputtering Machine to Deposit the Proposed Coating Materials... 60	
3.5. Deposition and Testing of the Proposed Absorbers .....	65
3.6. Estimation of the Annual Converted Energy.....	70
4. Coating Deposition by Roll-to-Roll Sputtering Machine .....	78
4.1. Roll-to-Roll Industrial Sputtering Machine.....	78
4.2. Design of the Novel Magnet Pack.....	82
4.3. Tests of the Proposed Magnet Pack for Cr and Cr <sub>2</sub> O <sub>3</sub> Layers .....	88
4.4. SiO <sub>2</sub> Deposition: RF and DC Reactive Sputtering .....	92
Conclusion.....	99
Bibliography.....	101

## Nomenclature

$A_{\text{abs}}$	area of the flat plate absorber (m <sup>2</sup> )
$A_{\text{gross}}$	gross area of the panel (m <sup>2</sup> )
$A_{\text{net}}$	net absorbing area of the panel (m <sup>2</sup> )
$\alpha$	spectrally averaged solar absorptance
$\alpha_K$	accommodation coefficient
$\alpha_{\text{LED}}$	spectrally averaged LED light absorptance
$\alpha_{\text{LED-OPT}}$	spectrally averaged LED light absorptance measured by optical analysis
$\alpha_{\text{light}}$	spectrally averaged absorptance under solar or LED spectrum
$\alpha_{\text{Sun}}$	spectrally averaged solar radiation absorptance
$\alpha_{\text{Sun-OPT}}$	spectrally averaged solar radiation absorptance measured by optical analysis
$\alpha_\lambda$	spectral absorptivity
$\vec{B}$	magnetic field (T)
$c$	speed of light (m s <sup>-1</sup> )
$C$	concentration factor of solar irradiation
$c_p$	heat capacity (J g <sup>-1</sup> K <sup>-1</sup> )
$c_{p-th}$	heat capacity of the bolt to fasten the thermocouple probe (J g <sup>-1</sup> K <sup>-1</sup> )
$\gamma$	ratio of the specific heats of the gas
$d$	gas particle diameter (m)
$D_{\text{Arrh}}$	pre-exponential Arrhenius coefficient
$D_{\text{wire}}$	diameter of the connecting wire (m)
$\delta$	characteristic geometric size of the chamber (m)
$\Delta T$	temperature difference (K)
$\vec{E}_{\text{static}}$	electrostatic field (N C <sup>-1</sup> )
$E_{\text{BB}}$	spectral emission of the Black Body (W m <sup>-2</sup> nm <sup>-1</sup> )
$E_{\text{max}}$	maximum illumination intensity (W m <sup>-2</sup> )
$E_{\text{mean}}$	mean illumination intensity (W m <sup>-2</sup> )
$E_{\text{min}}$	minimum illumination intensity (W m <sup>-2</sup> )
$\varepsilon$	spectrally averaged thermal emittance
$\varepsilon_{\text{eff}}$	effective thermal emittance
$\varepsilon_{\text{eff-abs}}$	effective thermal emittance of the couple absorber-glass
$\varepsilon_{\text{eff-plates}}$	effective thermal emittance of two infinite parallel plates
$\varepsilon_{\text{eff-sub}}$	effective thermal emittance of the couple substrate-vessel
$\varepsilon_{\text{eff-TOT}}$	total effective thermal emittance of the absorber
$\varepsilon_{\text{wire}}$	thermal emittance of the connecting wire
$\varepsilon_\lambda$	spectral emissivity
$\vec{F}_{\text{Lorentz}}$	Lorentz force (N)
$G_{\text{Sun}}$	spectral solar radiation (W m <sup>-2</sup> nm <sup>-1</sup> )
$\eta_{\text{abs}}$	absorber efficiency
$\eta_{\text{abs-eff}}$	effective absorber efficiency
$h$	Planck's constant (eV s)
$\theta_i$	angle of the incident ray (rad)
$\theta_t$	angle of the transmitted ray (rad)
$I_{\text{sample}}$	spectral reflected light intensity of the sample (W nm <sup>-1</sup> )
$I_{\text{ref}}$	spectral reflected light intensity of the calibrated reference (W nm <sup>-1</sup> )

$k$	extinction coefficient of electromagnetic waves through the matter
$K_{\text{all}}$	thermal conductance parameter of the overall system ( $\text{W K}^{-1}$ )
$k_{\text{B}}$	Boltzmann's constant ( $\text{J K}^{-1}$ )
$K_{\text{cond}}$	thermal conduction parameter of the overall evacuated panel ( $\text{W K}^{-1}$ )
$K_{\text{diff}}$	diffusion coefficient for coating degradation
$K_{\text{E}}$	kinetic energy of gas particles (J)
$k_{\text{gas}}$	thermal conductivity of the gas ( $\text{W m}^{-1} \text{K}^{-1}$ )
$k_{\text{gas-0}}$	thermal conductivity of the gas at ambient pressure ( $\text{W m}^{-1} \text{K}^{-1}$ )
$Kn$	Knudsen number
$k_{\text{wire}}$	thermal conductivity of the connecting wire ( $\text{W m}^{-1} \text{K}^{-1}$ )
$l$	mean free path of gas particles (m)
$\lambda$	electromagnetic wavelength (nm)
$m_{\text{abs}}$	absorber's mass (g)
$m_{\text{gas}}$	mass of the single gas particle (g)
$m_{\text{th}}$	mass of the bolt to fasten the thermocouple probe (g)
$n$	refractive index
$N$	number of gas particles
$p$	gas pressure (Pa)
$P_{\text{in}}$	incident radiative power ( $\text{W m}^{-2}$ )
$P_{\text{light}}$	irradiation incident over the glass of the calorimetric test facility ( $\text{Wm}^{-2}$ )
$q_e$	electric charge of the electron (C)
$\dot{q}_{\text{gas}}$	conductive heat exchange through the gas ( $\text{W m}^{-2}$ )
$q_{\text{h}}$	net heat directed to the pipes of the panel ( $\text{W m}^{-2}$ )
$\dot{Q}_{\text{heater}}$	electric power of the heater (W)
$\dot{Q}_{\text{S}}$	heat loss through the connecting wire (W)
$R$	ideal gas constant ( $\text{J mol}^{-1} \text{K}^{-1}$ )
$R_{\text{p}}$	fraction of the reflected light parallel to the incident plane
$R_{\text{s}}$	fraction of the reflected light orthogonal to the incident plane
$\rho_{\text{sample}}$	spectral reflectivity of the calibrated reference
$\rho_{\lambda}$	spectral reflectivity
$\sigma$	Stefan-Boltzmann constant ( $\text{W m}^{-2} \text{K}^{-4}$ )
$T$	absolute temperature (K)
$t$	relative time (s)
$T_{\text{abs}}$	absorber's temperature (K)
$T_{\text{amb}}$	ambient temperature (K)
$T_{\text{gla}}$	glass' temperature (K)
$T_{\text{i}}$	temperature of the gas particle before the collision with the wall (K)
$T_{\text{r}}$	temperature of the gas particle after the collision with the wall (K)
$T_{\text{stag}}$	stagnation temperature of the absorber (K)
$T_{\text{ves}}$	vessel's temperature (K)
$T_{\text{w}}$	temperature of the wall (K)
$\tau_{\text{gla}}$	glass transparency
$\tau_{\lambda}$	spectral transmissivity
$\bar{v}$	average speed of gas particles ( $\text{m s}^{-1}$ )
$V$	volume of the chamber ( $\text{m}^3$ )
$w$	weighting factor

## Introduction

In Europe the amount of energy demanded for only heating and cooling is half of the total [1]. Within the industrial sector, process heat is the most relevant and the specific mid-temperature range 100 °C – 200 °C weights 21% of the overall industrial demand of heating and cooling. Solar thermal receivers are the most feasible solution to renewably respond to such a demand, and some technologies are already available to be applied at large scale [2]. The choice of the proper receiver mainly depends on the nominal operating temperature, as it drives the thermal losses of the absorber (component demanded to convert the solar radiation into heat), and all the available technical arrangements for solar collectors differ for the way those losses are minimized.

At operating temperatures below 100 °C, the traditional unconcentrated flat panel proved to be effective and widely used for sanitary hot water, but above that temperature threshold, the extensive convective and conductive thermal losses within the envelope make impossible its employment. The common pathway to reach higher temperatures is the adoption solar light concentration. The presence of reflectors directing the light towards the absorber allows the reduction of its exposed surface, minimizing its contribution to thermal losses. The most used architectures adopt cylindrical, or even flat, absorbers encapsulated coaxially into evacuated glass tubes and surrounded by external parabolic reflectors [3]. The main drawbacks for these kind of solutions are reduced optical efficiency due to the presence of reflectors, low fill factor of the gross area and, typically, the need for an active solar tracking system [4].

In recent years a novel architecture able to overcome those limits is emerging: the flat collector hosting an unconcentrated plate absorber working under vacuum insulation. The reduced encumbrance, larger fill factor, wider acceptance angle of the solar radiation, and no need for any tracking system make this solution more appealing than traditional evacuated tube collectors. Originally, the idea was presented by Eaton and Blum (1975) [5] who applied a moderate vacuum at pressure of 1 mbar to a flat plate collector. The suppression of internal convective motions sensibly reduced thermal losses limiting the heat transfer of residual gases only to conduction. Filling the envelope with Krypton at pressure of 50 mbar, the efficiency reached even 45% at 150 °C of absorber temperature [6]. Moss et al. tested a small-scale prototype of flat plate thermal collector without concentration, and a further reduction of internal pressure, below  $5 \times 10^{-3}$  mbar, minimized thermal conduction of residual gases to a negligible level [7]. They also showed the potential to guarantee a larger quantity of annually converted energy with respect to concentrated evacuated tubes, more than 60%, due to a wider acceptance angle to collect more diffuse solar light and a larger fill factor of the gross area.

Besides, two companies proposed commercial flat panels working under high-vacuum insulation, SRB Energy in 2005 [8] and TVP Solar SA in 2008 [9], but only the second is still active. A recent study reports the great performances of their technology showing experimental results from a 50 m<sup>2</sup> plant of TVP Solar SA panels by four-months testing under ordinary operation [10]. The global efficiency reached 50% at 150 °C of absorber temperature, being unrivalled among mid-temperature solar thermal collectors. That interesting performance could have even been improved if the proper absorber had been installed. TVP Solar SA panels were equipped with Mirotherm® from Alanod [11] which is a selective solar thermal absorber designed to work for low-temperature applications. The choice for this kind

of absorber was forced by the lack of commercial absorbers properly designed to operate unconcentrated at mid-temperatures up to 200 °C. Indeed, shifting from the traditional not evacuated to the evacuated flat panel, the main thermal loss moves from the contribution of convection and conduction of the gas surrounding the absorber to the radiative emission of the absorber itself. As it is discussed in the following section 1.1, which summarizes the basic technologies for flat vacuum enclosures, when the pressure of residual gas is below a certain threshold even the gas conduction can be neglected [6], giving to this kind of solar panel a new paradigm for the thermal losses. The scope of the presented work is to produce a properly designed solar thermal absorber with a controlled thermal emittance, suited to operate at mid-temperatures under high vacuum insulation without concentration.

Basic features of solar thermal absorbers are analysed in paragraph 1.2, then in 1.3 their traditional optical characterization is described. It consists of the measurement of the absorber's radiative properties, such as the solar light absorptance and thermal emittance, through the analysis of reflectivity. The main limit of this approach are the boundary conditions of room pressure and temperature during the measurement, whereas the real operation of the absorber is completely different since high vacuum and temperatures up to 200 °C might significantly change its radiative response. In chapter 2, a novel experimental facility is described to calorimetrically test absorbers under real operating conditions, overcoming the limits of the optical approach. It consists of a panel-like vacuum chamber containing the absorber while exposed to the solar irradiation in outdoor tests. Indoor tests were conducted too by use of a novel low-cost solar simulator, properly designed for the purpose.

The following step was the production of novel absorbers designed to work for mid-temperature applications (100 °C – 200 °C). The manufacturing of these absorbers was carried in laboratory by Sputtering Physical Vapour deposition of a multi-layered coating based on Cr, Cr<sub>2</sub>O<sub>3</sub>, and SiO<sub>2</sub> over commercial copper substrates. This deposition technique was preferred to others because of its broad employment at industrial scale for commercial low-temperature flat absorbers. Details of the depositions carried out in laboratory are the subject of chapter 3 together with the experimental characterization of the produced absorbers and the expected improvement on the panel performance.

To assess the feasibility of depositing each material of the proposed multi-layered coating with an industrial machine, experimental tests were conducted at TVP Solar SA laboratories (Geneva, Switzerland) during the six-months period of experience abroad. Contextually, a novel magnet pack was designed to overcome all the limits of the commercial alternative in terms of lifetime and maintenance procedure, introducing an innovative geometry of the magnetic field.

# 1. Technologies of the Evacuated Flat Panel

This chapter provides fundamentals of the technologies in use for the evacuated solar thermal flat panel. Each paragraph focuses on a specific aspect of the panel to illustrate the scenario surrounding the absorber and its role to improve the overall performance. In the following section 1.1 are reported some technical solutions about the hermetic flat envelope and the impact on thermal losses of different levels of vacuum. Then in paragraph 1.2, features of solar absorbers are described together with the most used manufacturing processes. In the paragraph 1.3, last of the chapter, the two most common optical characterization facilities to test solar absorbers are described and their limits discussed, paving the way to the chapter 2.

## 1.1. *Vacuum Envelopes for Solar Thermal Collectors*

Two are the typical designs of vacuum enclosures for flat collectors: one is the symmetrical enclosure with a glass pane on the back as well as on the front [12, p. 1], and the other is a metallic vessel body closed by the front glass [13]. Both solutions are feasible for mid-temperature applications, but the second is more appealing for industrial process heat since the back of the panel is not architecturally significant. Even if the first solution has no metallic envelope, the vacuum sealing inevitably occurs between the glass and a metallic surface. To close the volume within the two glass panes a metallic frame support is adopted thanks to its elasticity and resistance against mechanical and thermal stress. For both solutions, the exit ports of the inlet and outlet pipes carrying the operating fluid are sealed by a metal-to-metal welding on the metallic frame, for the first, or the rear body of the envelope, for the second.

One of the possible techniques to obtain the glass-metal vacuum sealing is ultrasonic soldering. It consists of depositing thin layers of molten metals directly on the glass as sealing material while the ultrasonic vibration removes the external oxide layer of the substrate allowing the molten solder to wet and bound to it. An example is bonding by Indium [14], but its relatively low melting point of 156 °C and its limited availability make it not feasible for large scale use for solar panels. Other materials as Tin alloys [15], or Cobalt-Nickel-Iron alloys [16] revealed to be more effective and perfectly feasible. Another approach is the frit glass bonding, where a glass-based paste is kept at its melting temperature while in contact with the glass and metal surface. The chemical affinity of the materials is what drives the sticking with no need for ultrasonic process [17]. In general, what is demanded to such vacuum sealings, in addition to vacuum tightness, are controlled degassing during operation and low soldering temperature. When such a temperature overcomes 250 °C, tempered glasses typically start to lose their mechanical properties and weaken, compromising the resistance against implosion.

Another important requirement of evacuated flat envelopes is the need for an active system to pump the gases released into the vacuum environment by every internal surface over years of operation, otherwise there would be an increase of the internal pressure above unacceptable values. Once the panel has been fully evacuated and then hermetically closed, there is no access to the internal of the panel and eventually the mechanical pumping would not be feasible. The only possible pathway is the adoption of a chemical getter pump hosted inside the collector and thermally activated by temperatures around 300 °C, perfectly

compatible with the solar irradiation and vacuum insulation. These devices actively absorb residual gases to guarantee high vacuum for the whole service life [8], [9].

The other important component of this kind of panels is the supporting structure to make the envelope resist the external ambient pressure. Envelope and supporting structure must be designed to minimize the mechanical stress on the vacuum sealing, which is the extremely vulnerable to tangential forces, and to sustain the glass from the inside to avoid the implosion. The most adopted solution to sustain the glass and the bottom of the vessel is the pin rack structure. It allows the glass and the bottom to sustain each other by loading the mechanical force exerted by the ambient pressure to the opposite side of each. Shape, size, horizontal and vertical pitch are part of the designing process of the pin rack structure together with the design of the whole vacuum envelope. Because glass and vessel are mechanically connected by the pin rack, the absorber, which inevitably is in the middle, has holes to host each single pin. This has a negative impact on the net operating area of the absorber affecting the overall conversion efficiency of the device. The optimization of shape and size of such holes is mandatory as smaller the holes, higher the probability of contact with the absorber and bigger the thermal losses, contextually a larger pitch of the structure would be not enough to avoid glass implosion. [12].

In **Fig. 1.1** are shown two examples of evacuated flat panels with the stainless-steel vessel, **(a)** is the only commercial evacuated flat collector still produced and available for large scale applications, from TVP Solar SA [9]; **(b)** is a prototype aimed at research activity presented by Moss et al. [13]. The pipes carrying the working fluid are welded to the rear of the absorber and are mechanically fixed on a structure fixed on the bottom of the vessel. Minimization of contact points between the pipes and their supporting structure is key to control the relative conductive thermal losses.

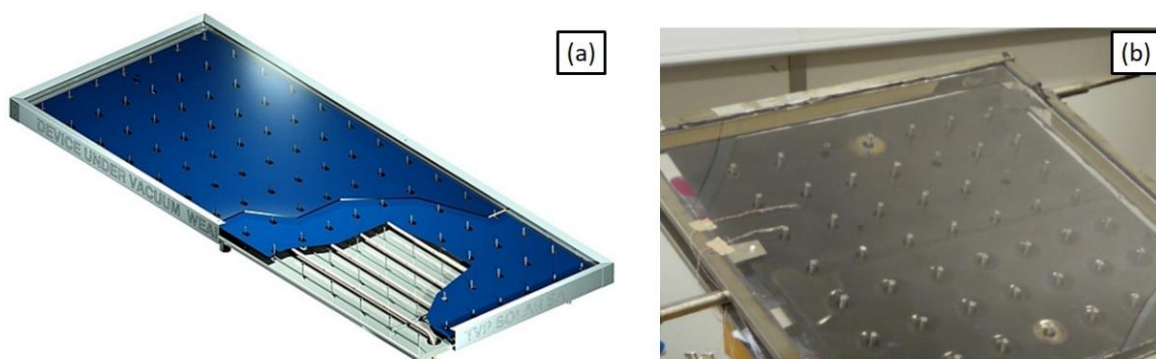


**Fig. 1.1** Two examples of solar thermal flat panels for mid-temperature applications are shown. (a) The commercial device from TVP Solar SA [9] and (b) the prototype studied by Moss et al. in 2018 [13].

All the technical solutions for this particular type of solar collector, cited and described so far, were conceived to respond to the demand for vacuum insulation of the absorber to minimize the thermal losses due to the presence of the internal gas. To thermally analyse this aspect, the Boltzmann's kinetic theory of perfect gas [18] is an effective instrument to analytically estimate the impact of the internal gas on the thermal losses as function of the level of pressure. It is based on hypothesis of gas particles approximated as spheres with fixed

diameter, the collisions to the walls and other particles are perfectly elastic and no chemical reaction occurs, the direction of displacement is random and along straight lines, and the kinetic energy is the only form of energy analysed. Under these hypotheses, the kinetic energy  $K_E$  of each particle is linearly proportional to the gas temperature  $T$  as reported in eq. 1.1.

$$K_E = \frac{1}{2} m_{gas} \overline{v^2} = \frac{3}{2} k_B T \quad 1.1$$

Where  $m_{gas}$  and  $\overline{v^2}$  are the mass and average squared speed of each particle, respectively, and  $k_B$  is the Boltzmann's constant. The pressure is the force exerted on the container's walls by particles collisions and it depends on  $K_E$ , the number of contained particles  $N$  and the container's volume  $V$ , as shown in eq. 1.2.

$$p = \frac{2}{3} \frac{N K_E}{V} \quad 1.2$$

The mean free path  $l$  between two consecutive collisions is function of pressure  $p$ , temperature  $T$ , and particle diameter  $d$ , see eq. 1.3.

$$l = \frac{k_b T}{\sqrt{2} \pi d^2 p} \quad 1.3$$

Another way to express the mean free path  $l$  is through the Knudsen number  $Kn$ . It is a dimensionless parameter and is the ratio between the mean free path  $l$  and the characteristic geometric size  $\delta$  of the container, see eq. 1.4.

$$Kn = \frac{l}{\delta} = \frac{k_b T}{\sqrt{2} \pi d^2 p \delta} \quad 1.4$$

These presented parameters are basics of the kinetic theory, and the thermal conductivity of the gas is modelled accordingly. Assumed to have two parallel walls at two different temperatures and a perfect gas in between, the heat transfer is modelled as a momentum transfer of particles, since those close to the hot surface have more translational energy  $K_E$  than those close to the cold, as expressed in 1.1. Each particle collision, to the walls or to other particles, is cause of momentum transfer, and the hypothesis of perfectly elastic collisions is enough to model the thermal particle-particle interaction, whereas the particle-wall lacks information since no relation between the transferred momentum to the wall and the wall temperature has been modelled yet. To fill this gap, a new parameter is introduced and it is known as accommodation coefficient  $\alpha_K$  [19]. It regulates the transferred energy from/to the particle after a single collision to the wall and it is expressed as the ratio between the actual and the maximum temperature change of the particle, see eq. 1.5.

$$\alpha_K = \frac{T_r - T_i}{T_w - T_i} \quad 1.5$$

$T_i$  and  $T_r$  are the temperature of the particle before and after the collision with the wall, while  $T_w$  is the wall temperature. Based on these assumptions, the model returns an analytical expression for the thermal conductivity of the gas  $k_{gas}$ , and it is written in the following eq. 1.6 as function of the Knudsen number  $Kn$ , the accommodation coefficient  $\alpha_K$ , the ratio of the specific heats  $\gamma$ , and the thermal conductivity of the gas at atmospheric pressure  $k_{gas-0}$ . Traditionally, the dependence of  $\alpha_K$  and  $\gamma$  is enclosed in the coefficient  $\beta = (2-\alpha_K)(9\gamma-5)/[2\alpha_K(\gamma+1)]$ .

$$k_{gas} = \frac{k_{gas-0}}{1 + 2\beta Kn} \quad 1.6$$

Thermal conductivity of the gas  $k_{gas}$  is inversely proportional to  $Kn$ , which is in turn inversely proportional to pressure, returning the expected proportionality between thermal conductance and pressure.

Starting from eq. 1.6, some quantitative considerations can be done to realize how the pressure can affect the thermal loss due to presence of the internal gas. In **Fig. 1.2(a)**  $k_{gas}$  is reported as function of pressure for three  $\delta$  values of 0.01 m, 0.05 m and 0.1 m. These values are representative of the typical distances between the absorber and the surrounding walls, glass and bottom of the envelope, for the evacuated solar flat collector [8], [9], [12], [13]. From pressure of  $10^4$  mbar down to 10 mbar there is no change in  $k_{gas-0}$  for all the three distances. The physical interpretation of this behaviour is that every pressure alteration causes a variation of the number of collisions per unit of volume which is balanced by the variation in the opposite direction of the mean free path (continuous matter domain) [19]. In the range  $10^{-5} - 10$  mbar,  $k_{gas}$  reduce exponentially with pressure and the lower  $\delta$ , the lower  $k_{gas}$ . From  $10^{-5}$  mbar to lower pressures  $k_{gas}$  keeps below 1% of the ambient  $k_{gas-0}$  for all the three  $\delta$ . Such a strong reduction leads to the condition for which the mean free path of particles becomes smaller than  $\delta$ , so the number of collisions between particles is negligible with respect to particles and walls (molecular domain) [20]. When this happens, thermal conduction of gas is strongly reduced and, as consequence, any convective motion is prevented. On the other hand, the condition of continuous matter might undergo convective motions impacting on the total exchanged heat which depends on  $k_{gas}$  corrected by the Nusselt number. This is not deeply investigated since our application of high vacuum panels has always molecular domain.

Neglecting the presence of any convective motion, the total exchanged heat  $\dot{q}_{gas}$  in  $Wm^{-2}$  can be modelled through the Fourier formulation of conduction expressed in the following eq. 1.7, assumed that the heat transfer occurs perpendicularly to the absorber towards the glass and the bottom of the vessel, and being  $\delta$  the characteristic distance absorber-glass and absorber-vessel.

$$\dot{q}_{gas} = -k_{gas} \frac{\Delta T}{\delta} \quad 1.7$$

$\Delta T$  is the temperature difference between the absorber and its surrounding, as the glass and the vessel. **Fig. 1.2(b)** shows the resulting loss at four internal pressures  $10^{-5}$ ,  $10^{-4}$ ,  $10^{-3}$  and  $10^{-2}$  mbar combined with the three  $\delta$  as 0.01 m, 0.05 m, and 0.10 m under the conservative

hypothesis of accommodation coefficient  $\alpha_K = 1$ . For the pressure of  $10^{-2}$  mbar, shown with rhomboidal dots, there is a strong variation on  $k_{gas}$  with the characteristic length  $\delta$  and the higher  $\delta$ , the lower  $\dot{q}_{gas}$ . This seems to be the opposite of what results from Fig. 1.2(a), but the contradiction lays on the role of  $\delta$  in the eq. 1.7. In Fig. 1.2(b) at  $\Delta T = 100$  K and pressure of  $10^{-2}$  mbar,  $\dot{q}_{gas}$  shifts from  $18 \text{ Wm}^{-2}$  ( $\delta = 0.10$  m) to  $29 \text{ Wm}^{-2}$  ( $\delta = 0.05$  m), while in Fig. 1.2(a)  $k_{gas}$  decreased from  $1.82 \times 10^{-2} \text{ Wm}^{-1}\text{K}^{-1}$  ( $\delta = 0.10$  m) to  $1.47 \times 10^{-2} \text{ Wm}^{-1}\text{K}^{-1}$  ( $\delta = 0.05$  m). The increase of  $\dot{q}_{gas}$  of +60% for a reduction of  $k_{gas}$  of -20% derives from the fact that, being  $\delta$  at the denominator of eq. 1.7, its halved value from 0.10 m to 0.05 m doubles the contribution to  $\dot{q}_{gas}$ .

The reference value of solar irradiance is notoriously  $1 \text{ kWm}^{-2}$ , and for an internal pressure of  $10^{-2}$  mbar the thermal loss is unacceptable for the proper vacuum insulation, Fig. 1.2(b), with values of the order of tens of  $\text{Wm}^{-2}$  when  $\Delta T$  overcomes 100 K. For instance, considered  $\dot{q}_{gas}$  of the order of  $25 \text{ Wm}^{-2}$ , the corresponding fraction of the incident solar irradiance would be of 5%, as  $\dot{q}_{gas}$  must be multiplied by a factor of two to account both the sides of the absorber, one facing the glass and the other facing the bottom. At a lower pressure of  $10^{-3}$  mbar, the trend is similar but the values and range of variation of  $\dot{q}_{gas}$  with  $\delta$  are sensibly reduced, being the loss still of the order of few tens of  $\text{Wm}^{-2}$ . For sake of clarity, at pressures of  $10^{-4}$  mbar and  $10^{-5}$  mbar, only the curves related to  $\delta = 0.05$  m are reported because those resulting for the other two lengths ( $\delta = 0.01$  m and 0.1 m) are overlapped to that of  $\delta = 0.05$  m. At pressure of  $10^{-4}$  mbar, the loss does not exceed  $5 \text{ Wm}^{-2}$  even for  $\Delta T$  as high as 400 K and even considering the two sides of the absorber in the calculation of  $\dot{q}_{gas}$ , the total amount would not exceed  $10 \text{ Wm}^{-2}$ , i.e., 1% of the reference solar irradiation. This threshold is quite common among evacuated solar collectors [6], [7], [20] and this is the reason why evacuated flat panels need high vacuum (pressure below  $10^{-4}$  mbar), otherwise its thermal loss would be substantial. A further reduction of the pressure down to  $10^{-5}$  mbar reduces the loss of residual gas to a not appreciable level.

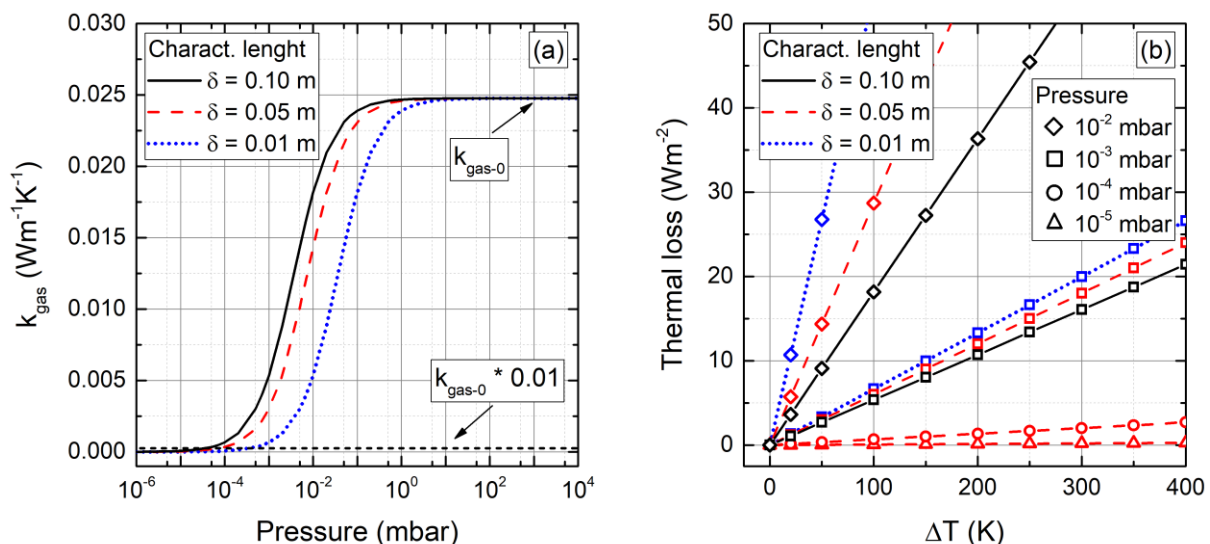


**Fig. 1.2** Impact of gas pressure and absorber-surrounding distance  $\delta$  on thermal conduction in flat plate solar collectors. (a) Thermal conductivity of the internal gas  $k_{gas}$ , calculated through eq. 1.6, is expressed in  $\text{Wm}^{-1}\text{K}^{-1}$  and reported as function of pressure for the characteristic lengths  $\delta = 0.01$  m, 0.05 m and 0.10 m. (b) Thermal loss of the residual gases is reported in  $\text{Wm}^{-2}$  relatively to the same three  $\delta$  at four pressure levels  $10^{-5}$ ,  $10^{-4}$ ,  $10^{-3}$ , and  $10^{-2}$  mbar as function of the temperature difference absorber-surrounding  $\Delta T$ .

## 1.2. Selective Solar Absorbers Fundamentals

Flat plate solar thermal collectors, independently from the presence of vacuum insulation, are equipped with a solar absorber. This component converts the solar radiation into heat and transfers it toward the pipes containing the working fluid through thermal conduction. High thermal conductivity of the absorber is mandatory to reduce the temperature gradient between the absorber and the fluid, which is cause of loss on the overall conversion performance. For this reason, absorbers designed for flat collectors are always made of copper or aluminium, since a thickness as small as few tenths of millimetre is enough to guarantee the proper heat transfer [21]. Being metals notoriously reflective, the surface exposed to the glass, dedicated to solar radiation absorption, is commonly coated by absorbing materials reaching fractions of total absorbed solar light above 90% [22]. The common temperature range of application for this kind of absorbers is below 100 °C, as they are used in flat collectors for domestic purposes, like water heating. Their maximum reachable temperature is limited by convection of air between the absorber-glass space and by conduction through the insulation material placed below the absorber to fill the gap with the vessel bottom. Because of the limited operating temperature, the radiative emission in the Infra-Red wavelengths of the absorber is just a secondary contribution to losses which are mainly driven by conductive and convective mechanisms. Nonetheless, the absorber design is aimed at maximizing the solar radiation absorptance and simultaneously limiting the emitted thermal radiation to negligible levels [23].

In literature, these devices are known as Selective Solar Absorbers, where the selectivity refers to the high values of absorptance in the solar wavelengths, and low emittance in the IR range, obtaining a peculiar shape of the spectral emissivity. According to the Kirchhoff 's law of radiation, in steady-state condition of thermal equilibrium, the spectral emissivity  $\varepsilon_\lambda$  regulates both absorption and emission mechanisms, as formulated by eq. 1.8, where spectral absorptivity  $\alpha_\lambda$  is equal to  $\varepsilon_\lambda$ .

$$\alpha_\lambda = \varepsilon_\lambda \quad 1.8$$

Because of this,  $\varepsilon_\lambda$  regulates the overall radiative performance of the absorber that is enclosed into two parameters: the spectrally averaged solar absorptance  $\alpha$  and spectrally averaged thermal emittance  $\varepsilon$  over the wavelengths  $\lambda$  of interest. These are reported in the following eq. 1.9 and 1.10, respectively.

$$\alpha = \frac{\int_{0.30 \mu m}^{4.0 \mu m} G_{Sun}(\lambda) \varepsilon_\lambda d\lambda}{\int_{0.30 \mu m}^{4.0 \mu m} G_{Sun}(\lambda) d\lambda} \quad 1.9$$

$$\varepsilon(T_{abs}) = \frac{\int_{0.30 \mu m}^{100 \mu m} E_{bb}(\lambda, T_{abs}) \varepsilon_\lambda d\lambda}{\sigma T_{abs}^4} \quad 1.10$$

Where the light absorptance  $\alpha$  is integrated over the wavelength range  $0.30 - 4.0 \mu\text{m}$ , typical of the solar irradiation  $G_{\text{Sun}}$ , and  $\varepsilon$  over the wider range of the whole interval of thermal wavelengths  $0.30 - 100 \mu\text{m}$ . The emitted spectral radiation is governed by the Planck's law of Black Body emission  $E_{\text{BB}}$  and is reported as eq. 1.11.

$$E_{bb}(\lambda, T_{\text{abs}}) = \frac{2\pi hc^2}{\lambda^5} \cdot \frac{1}{\exp\left(\frac{hc}{\lambda k_B T_{\text{abs}}}\right) - 1} \quad 1.11$$

The integration of  $E_{\text{BB}}$  over all the wavelengths is equal the denominator of eq. 1.10. This relation is well known as the Stefan-Boltzmann's law and expresses the equivalence of the integral of  $E_{\text{BB}}$  with the product of the Stefan's constant  $\sigma$  to the fourth power of the absorber temperature  $T_{\text{abs}}$ .

In **Fig. 1.3**, spectral emissivity of three commercial flat plate solar thermal absorbers is reported on the left axis as function of wavelength. They are Mirotherm<sup>®</sup> and Sunselect<sup>®</sup> (from Alanod [11]), and TiNOx-Energy<sup>®</sup> (from Almeco [24]). They are all obtained by Physical Vapour Deposition (PVD) of a proprietary coating over a metallic substrate. The first has an aluminium substrate, the second has copper, and the third, depending on the needs of the customer, can be obtained by applying the coating on both copper and aluminium. In the same figure, the solar spectrum, standard ASTM G173, is shown together with the spectral emission of the Black Body, eq. 1.11, for three absorber temperatures, 100 °C, 200 °C and 300 °C, right axis.

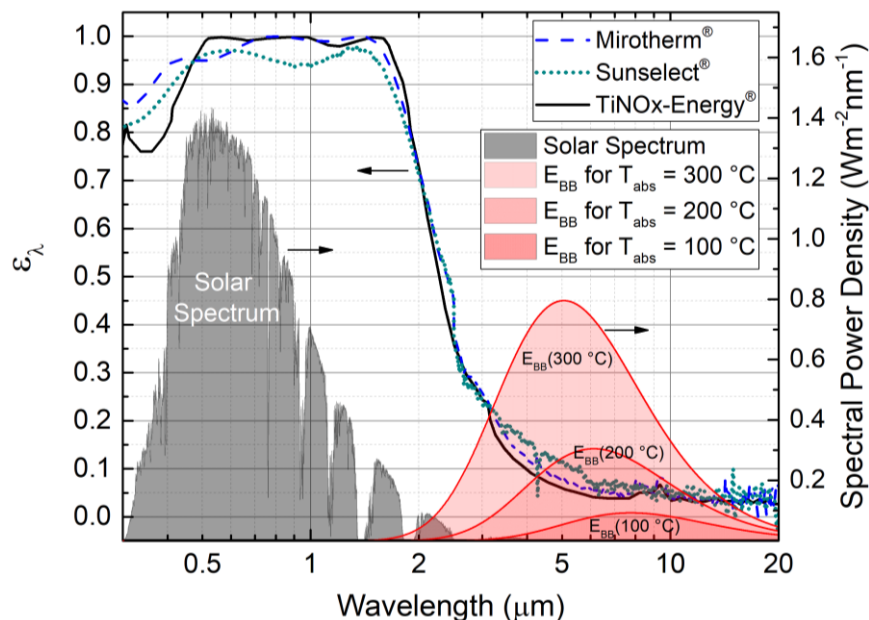


**Fig. 1.3** Spectral emissivities of three commercial flat plate solar thermal absorbers are reported as function of the wavelength, left axis. Mirotherm<sup>®</sup> and Sunselect<sup>®</sup> are from Alanod, the first has an aluminium and the second a copper substrate. TiNOx-Energy<sup>®</sup>, from Almeco, is available with both copper and aluminium substrate. The solar spectrum, standard ASTM G173, is shown together with the Planck's law spectral emission of the Black Body, eq. 1.11, for three temperatures 100, 200 and 300 °C, right axis.

The three reported spectral emissivity curves  $\varepsilon_\lambda$  are those declared by the datasheet of each commercial, and what emerges is that they share the same characteristic shape of emissivity curve, shifting from high values of emissivity in the solar spectrum to low emissivity in the IR range. It is worth noticing that the reduction of emissivity starts at the same wavelength, roughly  $1.8 \mu\text{m}$ , for all the three absorbers and they continue following quite the same rate of reduction with  $\lambda$ .

Eq. 1.9 defines the solar absorptance as a parameter with no dependence with the absorber temperature  $T_{\text{abs}}$ , eventually it would derive from the dependence of  $\varepsilon_\lambda$  with  $T_{\text{abs}}$  and, for easiness of discussion, here it is neglected and will be deeply discussed following. On the contrary, eq. 1.10 shows an analytical dependence of  $\varepsilon$  with  $T_{\text{abs}}$ , as  $E_{\text{BB}}$  increases and shifts towards shorter wavelengths as  $T_{\text{abs}}$  increases, as depicted in **Fig. 1.3**. What commonly is reported in commercial datasheets is the value of solar absorptance  $\alpha$ , around 0.95, and the upper limit of thermal emittance  $\varepsilon$  at  $100 \text{ }^\circ\text{C}$ , roughly of the order to 0.10. This radiative response is perfectly in line with the demand of plate absorbers for unconcentrated solar panels for domestic water heating. In case of higher operating temperature, thermal emittance significantly increases, as the  $E_{\text{BB}}$  spectral emission matches the increase of the spectral emissivity  $\varepsilon_\lambda$  in the range  $2 - 5 \mu\text{m}$ , see **Fig. 1.3**. For this reason, temperature is a key parameter in the design of a selective absorber and the proper importance must be given to the role of  $\alpha$  and  $\varepsilon$ . A very deep analysis was conducted about this subject by Cao et al. in 2014 [25]. They came out with a formula to quantitative estimate the relative importance of  $\alpha$  and  $\varepsilon$  for all the possible solar thermal applications and introduced two important concepts that guided the designing activity of the novel absorbers presented in this thesis: absorber efficiency  $\eta_{\text{abs}}$ , eq. 1.12, and weighting factor  $w$ , eq. 1.13.

$$\eta_{\text{abs}} = \frac{q_h}{G_{\text{Sun}}C} = \alpha - w\varepsilon \quad 1.12$$

$$w = \frac{\sigma(T_{\text{abs}}^4 - T_{\text{amb}}^4)}{G_{\text{Sun}}C} \quad 1.13$$

The absorber efficiency  $\eta_{\text{abs}}$  is postulated as the ratio between the heat directed to the pipes  $q_h$  of the collector and the total solar irradiance  $G_{\text{Sun}}$  incident over the absorber, considering the presence of the concentration factor  $C$  due to the presence of reflectors, see eq. 1.12.  $\eta_{\text{abs}}$  is also expressed as combination of  $\alpha$  and  $\varepsilon$  through weighting factor  $w$  which fixes the relative importance between the two parameters.  $w$  is defined as the ratio between the maximum exchangeable heat via radiation with the ambient at temperature  $T_{\text{amb}}$  and the solar radiation incident over the absorber,  $G_{\text{Sun}}$  times  $C$ . In other words,  $w$  quantifies the relative importance of the emission mechanism against the light absorption.

In the following **Fig. 1.4**,  $w$  calculated by eq. 1.13 is shown versus  $T_{\text{abs}}$  for three different levels of concentration  $C = 1, 10$  and  $100$  at fixed  $T_{\text{amb}}$  of  $25 \text{ }^\circ\text{C}$  and  $G_{\text{Sun}}$  of  $1 \text{ kWm}^{-2}$ . The region  $w > 1$  is marked by the yellow background. As expected, for a fixed  $C$ , the increase of  $T_{\text{abs}}$  produces the increase of  $w$  while for a fixed  $T_{\text{abs}}$ , an increase of  $C$  reduces  $w$ . From this graph it is possible to focus the situation about the plate absorbers for unconcentrated panels. The lack of reflectors limits the use of **Fig. 1.4** just to the curve  $C = 1$ . In case of traditional not-evacuated flat panels, the maximum reachable temperature is around  $100 \text{ }^\circ\text{C}$ , matching values of  $w$  sensibly lower than 1. On the other hand, thanks to the high vacuum insulation, the

operating temperature can reach values up to 200 °C and  $w$  increases up to 2. This profound change of  $w$  cannot happen for any other solar devices working with concentration, as the absorption mechanism is always more important than emission ( $w < 1$ ).

This also explains the overlap of the shift of the spectral emissivity curves for the three reported commercial absorbers. Their nominal operating temperature is below the threshold of 100 °C, and the maximum of the absorber efficiency is always reached enhancing  $\alpha$  at the expense of  $\epsilon$ . The introduction in the market of the evacuated flat plate panel working without concentration up to 200 °C is relatively recent, and the lack of plate absorbers designed to work under these new condition of  $w > 1$  pushed the research toward their study and optimization.

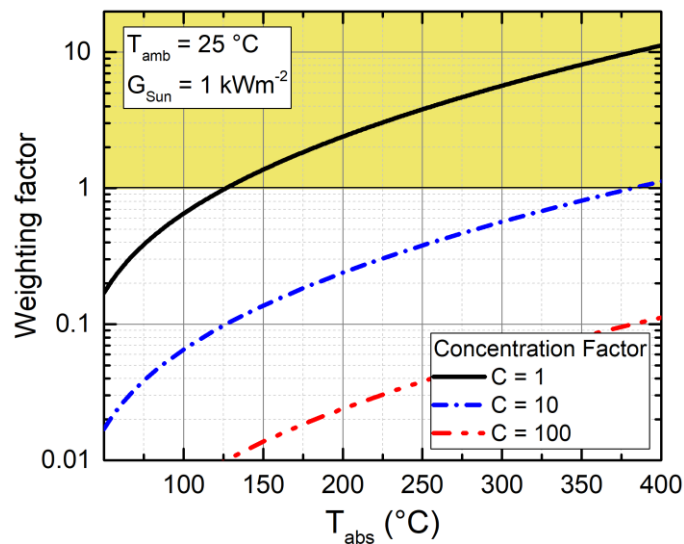


**Fig. 1.4** The weighting factor  $w$  calculated by eq. 1.13 is shown as function of the absorber temperature  $T_{abs}$  for three concentration factors  $C = 1, 10$  and  $100$  for a fixed ambient temperature  $T_{amb} = 25$  °C and solar irradiance  $G_{Sun}$  of  $1 \text{ kWm}^{-2}$ . The yellow zone stresses the points where  $w$  is bigger than 1, that is the unique condition of evacuated flat plate panels without concentration.

The design and production of novel absorbers optimized to work at  $w > 1$  lead to the analysis of the most adopted manufacturing processes. Six are the basic techniques to build a selective solar absorber. They are well known in literature [26], [27] and a summary scheme is reported in **Fig. 1.5**.

The first is the deposition of a layer of Intrinsic Selective Material over the reflective substrate, **Fig. 1.5(a)**. The bare substrate, because of its high reflectivity at all the wavelengths of interest, has very low solar absorptance and thermal emittance, so that the deposited layer on top is demanded to be absorptive in the solar range and transparent in the IR. Such a transparency is key to minimize the thermal emittance to take advantage of the high reflectivity of the substrate, which is usually a metal foil like copper, aluminium, or even stainless-steel coated with highly reflective metals like gold. Example candidates of intrinsic selective materials are  $\text{In}_2\text{O}_3$ ,  $\text{V}_2\text{O}_5$ ,  $\text{SnO}_2$  and  $\text{HfC}$ .

Based on the same concept there is another basic structure, the semiconductor layer over the metallic substrate with an anti-reflection layer on top, **Fig. 1.5(b)**. The typical band gap of semiconductors ranges from 1.0 to 2.5  $\mu\text{m}$  of wavelength and only radiation with shorter wavelength than the gap can be absorbed. For this reason, the additional layer of antireflective coating, usually oxides with a low refractive index, is needed to reach sufficient values of solar radiation absorptance. This phenomenon is driven by the mechanism of multiple reflections of the incident electromagnetic waves at the interfaces and is deeply discussed in the following sections.

The most used approaches to build a selective absorber feasible for a large production scale with effective radiative performances are the multi-layer coating, **Fig. 1.5(c)**, and the cermet composite coating, **Fig. 1.5(d)**, both deposited over a metallic substrate. The first is a 1-D architecture with the alternation of nanometric dielectric and metallic layers, while the second consists of metallic nanoparticles embedded in a dielectric layer. For both, the selectivity is obtained thanks to the interaction of the coating with the incident electromagnetic radiation by multiple reflections among all the layers of the multilayer and the metal particles of the cermet. High solar absorption is reached because the order of magnitude of the geometrical dimensions of those structures are comparable to solar wavelengths, whereas the same nanometric patterns are too small to interact with larger electromagnetic wavelengths of the mid- and far- IR, acquiring a progressive transition from the absorptive behaviour at shorter wavelengths to a good transparency at longer wavelengths where the thermal radiation occurs.

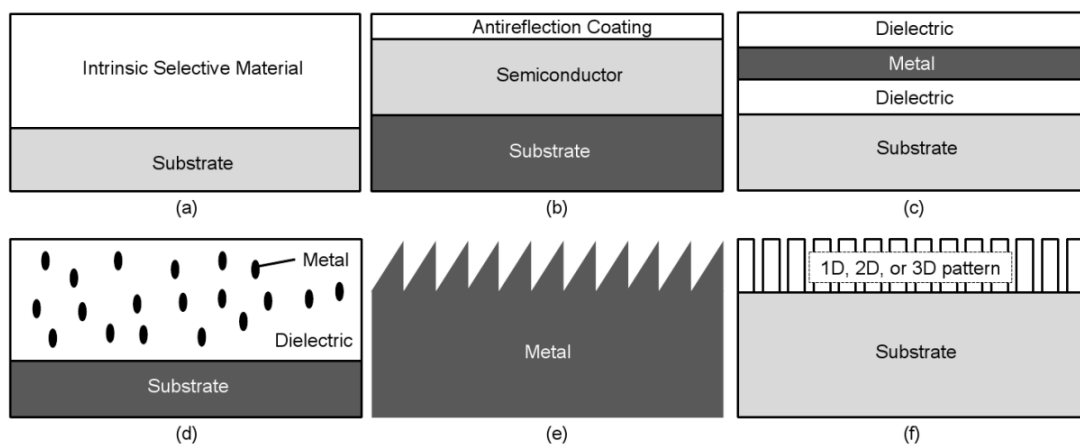


**Fig. 1.5** Six basic architectures for selective solar absorbers is presented. (a) Nanometric single layer of intrinsic selective material over metallic substrate. (b) Nanometric single semiconductor layer + antireflection coating over the metallic substrate. (c) Nanometric multi-layer coating, metal and dielectric alternation, over the metallic substrate. (d) Cermet layer, nanometric metal particles embedded in dielectric matrix, over the metallic substrate. (e) Nanometric patterns over the surface of a metal. (f) Deposition of nanometric structure over the metallic substrate [27].

Another basic method to obtain a selective absorber is impressing nano-scale geometrical patterns over the surface of a metal, **Fig. 1.5(e)**. Also in this case, the interaction with the solar light happens thanks to the nanometric dimension of the superficial texture, and even if the material of the surface is extremely reflective, it can reach acceptable values of absorptance.

At longer wavelengths, the nanometric patterns are “invisible” for the electromagnetic radiation, exhibiting the high reflectivity of the material.

The sixth technique, **Fig. 1.5(f)**, consists of the adoption of meta-materials deposited over the metallic substrate. Such meta-materials are 1D, 2D or 3D nanometric structures, whose selectivity depends on the interaction of the light wavelengths with those patterns.

The proposed list of architectures of selective absorbers is basic and useful to realize the right distinction between all the possible approaches. Indeed, great performances can be obtained by the combination of two or more of them. For instance, the coatings of three commercial absorbers presented before are multi-cermet layers with an anti-reflecting coating based on chromium oxide for Mirothem® and Sunselect®, and titanium oxynitride for TiNOx-Energy®, mixing the basic concept of **Fig. 1.5(b)-(c)-(d)**. These nanometric coatings can be deposited via two different Physical Vapour Deposition techniques, which are Sputtering and Electron Beam. These are perfectly suited for large scale industrial production as most of the final cost of the produced absorber is accountable to the substrate itself, being the amount of deposited materials extremely contained (thicknesses of the order of nanometres) and the costs to sustain the deposition process are distributed over kilometres of coils manufactured in the same run. In the paragraph 3.3, more details are reported about Sputtering, being the adopted process to deposit the proposed absorbers.

### 1.3. Optical Characterization of Selective Solar Absorbers

Spectral emissivity  $\varepsilon_\lambda$  is the key parameter controlling the performance of the absorber in terms of solar absorptance  $\alpha$  and thermal emittance  $\varepsilon$ , as seen through eq. 1.9 and 1.10. Production and design of selective solar absorbers cannot exempt from the measurement of those radiative properties, which, generally, is carried out via optical analysis of reflectivity of the absorber’s surface.

The optical interaction of the absorber with an incident electromagnetic wave of length  $\lambda$  is defined by the following eq. 1.14.

$$\alpha_\lambda + \rho_\lambda + \tau_\lambda = 1 \quad 1.14$$

It is basically an energy balance equation, where  $\alpha_\lambda$ ,  $\rho_\lambda$  and  $\tau_\lambda$  are absorptivity, reflectivity, and transmissivity of the absorber for the investigated wavelength  $\lambda$ . These parameters are the fraction of the absorbed, reflected, and transmitted intensity of the incident light, respectively. Eq. 1.14 is general and can be rewritten as eq. 1.15 for the specific case of solar thermal absorbers ( $\tau_\lambda = 0$  for opaque bodies like solar absorbers), imposed  $\alpha_\lambda = \varepsilon_\lambda$  due to the Kirchhoff’s law.

$$\varepsilon_\lambda = 1 - \rho_\lambda \quad 1.15$$

Because of this complementary relation, emissivity can be indirectly measured through the analysis of reflectivity. Eq. 1.15 is the basis of the two most used techniques to characterize absorbers: optical reflectometers and Fourier Transform Infra-Red spectrophotometers (FTIR). The use of the proper one depends on the wavelength range of the analysis, as the first can be used for the visible near-IR, while the second for the mid- to far-IR. This difference comes from the fact that the first measures directly the reflected light intensity, whereas the second measures a laser-generated interferogram and reconstructs the reflected light intensity

over the wavelengths through the Fourier transform. The reason of this distinction leads to the feature of photodetectors to have higher sensitivity at shorter wavelengths, so there is need for data transformation when the photoelectric signal intensity has high noise-to-signal ratio, as happens in mid- and far-IR. The calculation of the spectral reflectivity  $\rho_\lambda$  is possible thanks to the measurement of the reflected light by the investigated sample and the comparison of that of a calibrated reference.

In **Fig. 1.6(a)**, the conceptual scheme of a traditional reflectometer is depicted. It can be divided into two parts, the Integrating Sphere (IS) and the Optical Spectrum Analyser (OSA). The Integrating Sphere is a closed chamber whose internal walls are covered by highly reflective materials, and there are three apertures. One is to expose the sample surface to the cavity, another to host a lamp which illuminates exclusively the sample's aperture, and the third is a tiny hole to collect a little fraction of the light bouncing within the chamber. This amount of spilled light is conducted to an OSA through an optic fibre to quantitatively measure the light intensity at every wavelength. The internal geometry of the cavity is designed to measure the intensity of the light reflected in all the directions, giving to the diffuse and specular component of reflection the same weight by use of shielding baffles between the sample's aperture and the spilling hole. In **Fig. 1.6(b)**, an example of the spectral light intensity, outcome of the measurement procedure, is reported as function of the wavelength. The light intensity reflected by the sample (blue line) is between two curves belonging to the white and the black calibrated references, respectively with constant reflectivity around 0.99 and 0.01. In general, the choice of the proper reference mainly depends on the kind of investigated sample. When it is expected to measure highly reflective materials, the adoption of the white reference is recommended, otherwise, for highly absorbent samples, the black reference is to be considered. Because of the quite constant reflectivity of the references along the wavelengths, it is possible to recognize the spectrum of the lamp just observing the reference curves, like the white reference curve in **Fig. 1.6(b)**. For this specific case, it is a halogen lamp with emission in the visible to near-IR range.

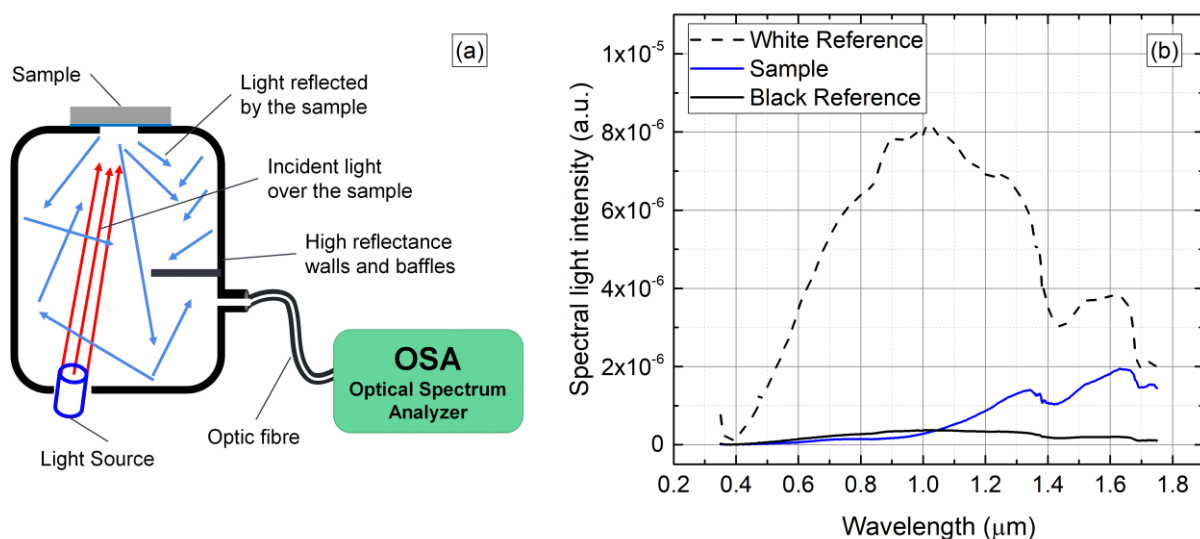


**Fig. 1.6** (a) The conceptual scheme of operation of reflectometers using an integrating sphere coupled to an Optical Spectrum Analyzer is shown. (b) The measured light intensities reflected by the sample, the white and black references are reported as function of the wavelength.

Once the spectrums of the reflected light, by the sample,  $I_{\text{sample}}$ , and by the reference,  $I_{\text{ref}}$ , have been measured, the spectral reflectivity  $\rho_{\lambda}$  can be evaluated according to eq. 1.16.

$$\rho_{\lambda} = \frac{I_{\text{sample}}}{I_{\text{ref}}} \rho_{\text{ref}} \quad 1.16$$

Where  $\rho_{\text{ref}}$  is the calibrated reflectivity of the adopted reference. This equation reveals that any eventual contribution due to the reflectivity of the internal walls, internal geometry of the cavity, transparency of the optic fibre, spectrum of the lamp and even the deterioration of every component is excluded because this measurement is always relative to the response of the calibrated reference.

In **Fig. 1.7(a)**, it is shown the Integrating Sphere, from Ocean Optics [28], used in this research activity to measure the reflectivity of produced samples in the visible and near-IR range. It is equipped with a halogen lamp and two optic fibres, one for the actual measurement of the spilled light, labelled as “S”, while the one labelled “R” is useful to check the time stability of the lamp. The two references, the white and the black, are shown in **Fig. 1.7(b)**. The “S” cable is connected to the spectrum analyser Ando AQ6315B, shown in **Fig. 1.7(c)**, which returns the measurement of the trapped light in the range 350 – 1750 nm.

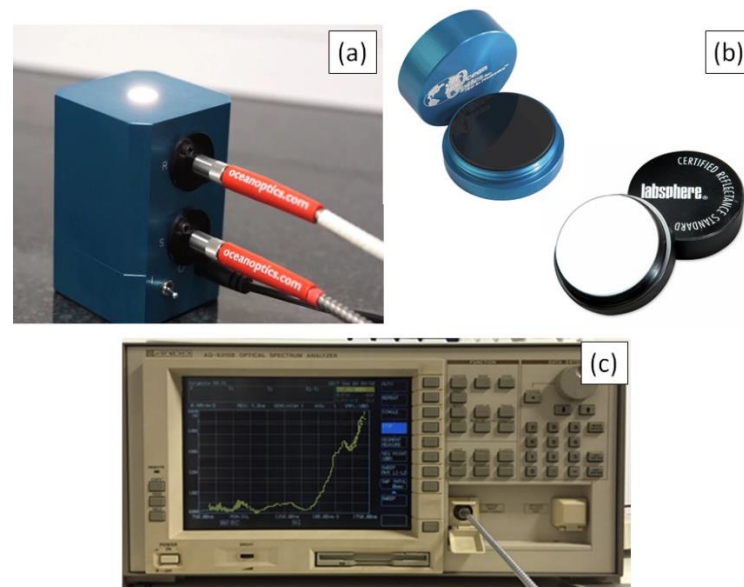


**Fig. 1.7** (a) The integrated sphere used in this work is shown during its operation. (b) The black and white references are reported, respectively on the left and right. The integrating sphere and the references are from Ocean Optics [28]. (c) The spectrum analyser Ando AQ6315B measures the trapped light by the optic fibre “S” in the range 350 – 1750 nm.

To carry out reflectivity measurements in the mid- and far-IR range, the FTIR spectroscopy is needed. Because of the larger wavelength of the light, photodetectors are not as responsive as they are for shorter wavelengths. For this reason, a more sophisticated approach is needed to reconstruct the curve of the spectral reflected light, but, once it has been acquired, the measurement procedure follows the same approach described for the reflectometers, i.e., measuring a calibrated reference and adopting eq. 1.16 to calculate the reflectivity curve. What actually makes the FTIR spectrophotometer different from a reflectometer is only how  $I_{\text{sample}}$  and  $I_{\text{ref}}$  are measured, while for all the other components, they

are very similar. Indeed, also the FTIR is be equipped with an integrating sphere to collect both diffuse and specular reflected light.

In **Fig. 1.8(a)**, the layout of the illumination system of an FTIR device is schemed. The IR source irradiates a Beam Splitter which splits the light into two components directing them toward two different mirrors, one is stationary the other is oscillating harmonically in the same direction of the light. The light reflected by the mirrors is directed again toward the Beam Splitter, and as before, the light is split again and part of it goes to a fourth direction (red arrow directed downwards in the figure) as the sum of half of the beam coming from the stationary and half of the oscillating mirror. Because of the component from the moving mirror, this recombined beam is a time dependent signal as the oscillation of the mirror shifts its reflected wave in space and provokes the alternation of constructive and destructive interference between the two components, as shown in **Fig. 1.8(b)**. The spectrum of the recombined beam changes in time, at each wavelength the variation is periodic between a maximum and a minimum with a frequency which depends on the length of the wave and the speed of the mirror oscillation. Thanks to the Fourier Transform, this periodic signal can be converted in a sum of harmonics whose amplitudes are proportional to the variation of light intensity at each wavelength, reconstructing the whole spectral light intensity of the signal. The need for a periodic time dependent light is due to the low sensitivity of photodetectors. To guarantee a low noise-to-signal ratio, these detectors are demanded to measure only the difference between the minimum and maximum at each wavelength, then the Fourier Transform is demanded to convert the signal into a spectral intensity curve.

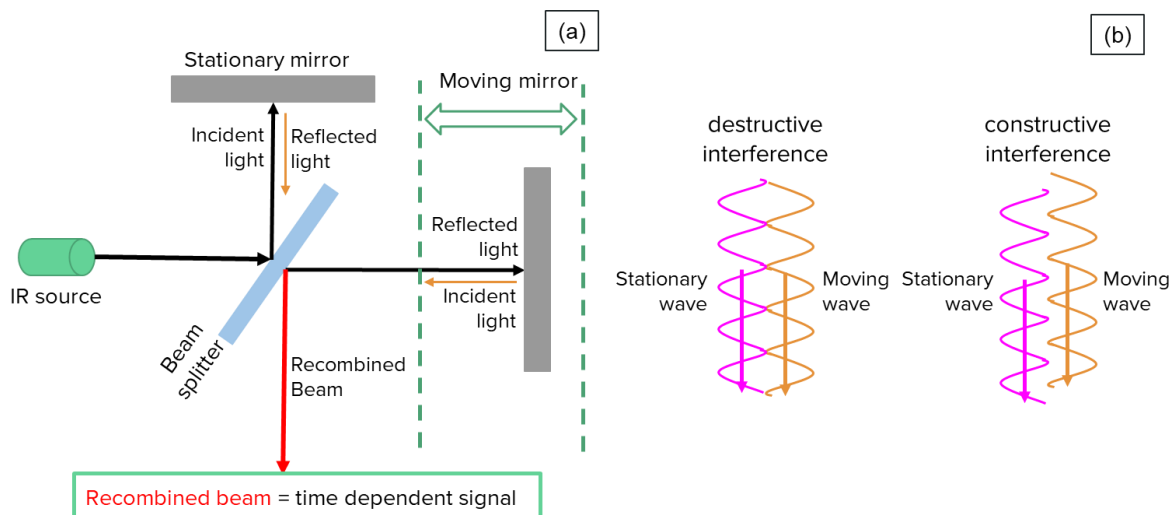


**Fig. 1.8** (a) The layout of the illuminating system for the FTIR device is composed of the IR source, a beam splitter, a stationary and a moving mirror to obtain a time dependent recombined beam. (b) The conceptual representation of the destructive and constructive interference between the wave coming from the stationary mirror and that from the moving one. The recombined beam is a time dependent signal because of the alternation in time of destructive and constructive interference of the light.

The adopted FTIR device in this research activity is the model 6300 from Jasco, see **Fig. 1.9(a)**, operating in the range 1.5 – 20.0  $\mu\text{m}$ . The measurement chamber is hermetically closed to allow a rough evacuation of the internal air by use of a rotary primary pump. This is useful to reduce the absorption peaks in the IR of the room air. In **Fig. 1.9(b)** an example of measured spectral light intensity is shown. Because of the limited response of photodetectors in the IR

range, the adopted calibrated reference must be highly reflective, indeed, this device is equipped with a flat smooth aluminium as calibrated reference.

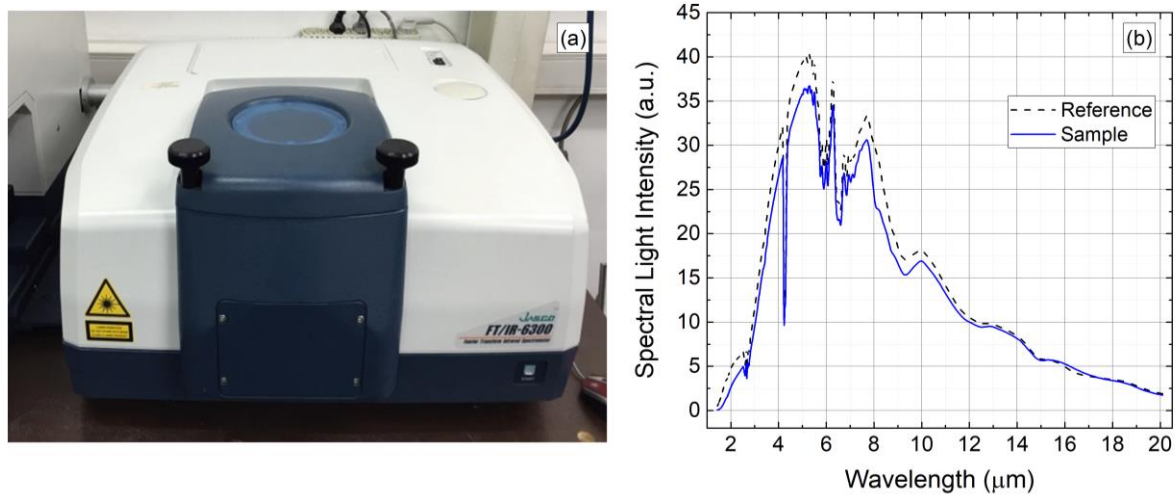


**Fig. 1.9** (a) The experimental setup used to measure the reflectivity of samples in the range 1.5 – 20 μm is shown, FTIR-6300 from Jasco. (b) An example of measurement outcome of the FTIR spectroscopy is reported. The spectral light intensity is referred to the light reflected by the sample and the aluminium reference.

The main limit of these two technologies, which optically measure the spectral reflectivity to calculate the spectral emissivity through eq. 1.15, is the boundary conditions of the investigated sample during the measurement. Generally, commercial optical devices operate at room pressure and temperature, condition acceptable when the operation of the absorber is of low temperature as 60 – 80 °C, like not-evacuated panels the domestic heating, being not far from that of the optical measurement. On the contrary, our case of evacuated collectors has operating temperatures always above 100 °C with the absorber into a high vacuum environment. Unfortunately, there is no optical device in commerce equipped with a heated sample holder and, simultaneously, with a pumping system to evacuate the measurement chamber to reproduce the peculiar conditions of the evacuated panel. Operating conditions too far from those of the optic measurement could lead to the unreliability of the resulting spectral emissivity  $\varepsilon_\lambda$ .

Some works in literature describe novel devices designed to perform measurements of  $\varepsilon_\lambda$  at high temperatures [29]–[31]. Echániz et al. showed some  $\varepsilon_\lambda$  resulting for a multilayered absorber (based on Si, N, Mo over stainless-steel Ag coated), carried out by a homemade IR-radiometer with the sample under moderate vacuum ( $10^{-3}$  mbar) and at various  $T_{\text{abs}}$ , from 250 °C to 600 °C. Calculation of the thermal emittance  $\varepsilon_{\text{abs}}(T_{\text{abs}})$  reported a discrepancy of the order of +8% when compared to those based on  $\varepsilon_\lambda$  measured at room temperature [31]. Similar results were obtained also by another group thanks to a different setup and testing another multilayered absorber (based on Ti, Al, C, N and O) but still reporting that room temperature measurement tends to underestimate  $\varepsilon_{\text{abs}}$  of 3.2% at  $T_{\text{abs}} = 200$  °C up to around 10% at 500 °C [32]. Very similar discrepancies are reported also for another coating based on W, Si and N over stainless steel for the same temperature range [33].

The devices used to perform such measurements are prototypical and their complexity makes them difficult to replicate. Nevertheless, the accurate measurement of the radiative properties of the absorber is key to estimate the annual converted solar energy for the

evacuated plate absorber. So that, before the production of novel absorbers, the proper experimental test facility was designed and fabricated to perform the accurate and reliable characterization of absorbers under realistic boundary conditions. Manufacturing details and measurement algorithm are deeply described in the following chapter 2.

## 2. Measurement of Radiative Properties Under Realistic Operational Conditions

The optical measurement of reflectivity is the most common procedure to characterize solar absorbers. Another approach, limited only to prototypical devices for research activity, is calorimetry. It consists in calculating directly  $\alpha$  and  $\varepsilon$  from the power balance equation of the absorber during heating and/or cooling tests under controlled boundary conditions, overcoming the measurement of the spectral properties to be integrated over the wavelengths. The general formulation of the calorimetric equation is reported as follows in eq. 2.1 under the hypothesis of uniform temperature distribution of the absorber and its surroundings, and flat plate geometry of the sample.

$$m_{abs}c_p \frac{dT_{abs}}{dt} = \dot{Q}_{heater} - K_{all}(T_{abs} - T_{amb}) + P_{in}\alpha A_{abs} - \varepsilon_{eff}\sigma A_{abs}(T_{abs}^4 - T_{amb}^4) \quad 2.1$$

Where  $m_{abs}$ ,  $c_p$ ,  $T_{abs}$  and  $A_{abs}$  are mass, heat capacity, temperature, and surface of the absorber exposed to the Sun, respectively.  $\dot{Q}_{heater}$  is the positive contribution to the absorber's temperature derivative  $dT_{abs}/dt$  due to eventual contact with an electric heater.  $K_{all}$  is a conduction coefficient and represents the sum of all the thermal conduction losses due to contact with the absorber, like the presence of gas in the chamber and contact with a supporting structure. The overall conduction loss is modelled as  $K_{all}$  times the temperature difference between the absorber and that of the surrounding environment  $T_{amb}$ . The contribution due to the absorbed light is built as the product between  $P_{in}$  and  $\alpha$ . The first is the light power density coming from a solar simulator and incident over the absorber, while  $\alpha$  is its solar absorptance. The last term is the radiative loss of the absorber and is formulated as a thermal emittance parameter  $\varepsilon_{eff}$  times the difference of the fourth power of  $T_{abs}$  and  $T_{amb}$ . This term comes out from the Stefan-Boltzmann's law of radiation applied to the theory of uniform radiosity in radiating cavities based. The thermal emittance  $\varepsilon_{eff}$  is called "effective" because the net radiative heat exchange of the absorber depends not only on the thermal emittance of the absorber  $\varepsilon$ , but also on shape, relative position, and thermal emittances of all the other surfaces of the cavity. The exact analytical expression of  $\varepsilon_{eff}$  is complex and not always possible [34]. Since the aim of the calorimetric test is to determine only the thermal emittance  $\varepsilon$  of the absorber, all the available calorimetric facilities in literature have the sample's area orders of magnitude smaller than the size of the cavity, so that the environment can be approximated as Black Body obtaining the relation  $\varepsilon_{eff} = \varepsilon$ . In this way, the calorimetric equation 2.1 contains exactly the two absorber radiative properties of interest ( $\alpha$  and  $\varepsilon$ ).

The idea of calorimetric measurement was already used in 1978 to test selective coatings over metallic substrates. The device consisted in a high vacuum enclosure (pressure below  $5 \times 10^{-6}$  mbar) equipped with a quartz window to let an external xenon lamp heat the sample. It was exposed to the cavity only by the coated side while its back and edges faced an isothermal support. This was possible because such a support was thermally controlled by PID system that adjusted the current passing through the electric heater. In these conditions, the calorimetric equation has null  $K_{all}$  and  $\dot{Q}_{heater}$  due to the high-vacuum and isothermal support, and the temperature derivative of the sample depends only on its light absorptance  $\alpha$  and thermal emittance  $\varepsilon$  [35].

More recently Kreamer et al. in 2015 proposed a novel calorimetric device to measure  $\alpha$  and thermal emittance of both sides of the selective solar absorbers. The sample is suspended

by metallic wires within the evacuated chamber and attached to a copper support via In/Ga bonding. The support is electrically heated and keeps the sample at the desired temperature. According to this architecture, the calorimetric equation has all the reported thermal contributions, and three individual experiments were needed to measure separately the two thermal emittances and  $K_{all}$  due to the parasitic heat losses through supporting wires and copper holder. By a fourth test,  $\alpha$  can be measured heating the sample by an external solar simulator through a fused silica viewport [36].

A similar architecture was used by Granados et al. to measure the thermal emittance of both sides of photovoltaic solar cells. The sample is suspended in the middle of the chamber by thermocouple leads under medium vacuum (below  $10^{-1}$  mbar) and heated by an external light passing through a transparent glass, with no additional support. Because of the poor vacuum insulation and thermocouple wires, their calorimetric tests needed to estimate the conduction contribution  $K_{all}$  together with  $\alpha$  and  $\varepsilon$  [37].

The calorimetric approach of measurement of  $\alpha$  and  $\varepsilon$  is powerful and overcomes all the limits of the optical analysis of reflectivity carried at room temperature. On the other hand, even if the boundary conditions during the calorimetric tests described in literature are close to those of evacuated panel (high vacuum and high temperature), the facilities have vacuum chambers designed to minimize their radiative role to take advantage of the approximation  $\varepsilon_{eff} = \varepsilon$ . During the operation of the evacuated flat panel, the absorber faces the internal surfaces of the cover glass and back of the stainless-steel vessel at distance of the order of 5 cm. This geometrical condition is extremely far from the ideal environment created for the calorimetric devices described in literature, implying that the effective thermal emittance  $\varepsilon_{eff}$  might significantly differ from  $\varepsilon$ . Analytical thermal models of solar flat panels approximate the interaction glass-absorber and absorber-vessel through the hypothesis of infinite parallel plates, where the theoretical  $\varepsilon_{eff}$  depends only on the thermal emittances of the two exposed surfaces  $\varepsilon_1$  and  $\varepsilon_2$ , see eq. 2.2. This approximation is reliable and valid properly for evacuated flat plate panels [38, p. 2].

$$\varepsilon_{eff-plates} = \frac{1}{\frac{1}{\varepsilon_1} + \frac{1}{\varepsilon_2} - 1} \quad 2.2$$

The goal of this activity is producing novel selective absorbers designed for the evacuated flat panel operating at mid-temperatures, but the lack of a test facility for the accurate measurement of the effective radiative properties during operation creates the need for the proper device to characterize the absorbers to be produced. What all the devices available in literature cannot provide is testing the absorber within a panel-like environment using the real solar irradiation, instead of a solar simulator, to accurately measure the solar absorptance. In addition, thanks to the panel-like chamber it is possible to directly measure the effective thermal emittance  $\varepsilon_{eff}$  instead of approximating it through eq. 2.2. Reproducing the real operating conditions of evacuated flat panel to assess the effective radiative properties of the absorber is the most accurate way to estimate the real performance, since the potential change of the absorber' spectral emissivity with temperature, for both absorption and emission mechanisms, and the real interaction with glass and vessel are in action during the calorimetric tests.

In this chapter a novel calorimetric test facility to better respond the described requirements is presented. It is sort of small-scale evacuated flat panel to carry out calorimetric

tests both outdoor and indoor, illuminating the sample with solar radiation or that of a simulator, respectively. Experimental results will confirm the importance of this kind of facility, being the best way to characterize solar absorbers for the evacuated flat panel operation.

### *2.1. Experimental setup of the novel calorimetric test facility*

The novel test facility is aimed at reproducing a panel-like environment for the absorber to be tested. The evacuated panel adopted as reference is the TVP Solar SA collector, being the only commercial device available today in the market [9]. Nevertheless, the experimental results obtained by the test facility can be extended to any other evacuated flat panel, since what might change from a commercial panel to another are the adopted constructive technical solutions, whereas the absorber is always supposed to work under the same boundary conditions of high vacuum.

The test facility consists of a squared stainless-steel vacuum chamber closed by a cover glass (tempered soda-lime glass with thickness of 4 mm). The section view, out of the CAD built with PTC Creo Parametric, is shown in **Fig. 2.1**. The vacuum seal is obtained by a custom-made Viton gasket hosted in a groove on the vessel flange and directly attached to the glass surface. Low pressure in the chamber is guaranteed by a pumping system composed of primary and turbo-molecular pump connected in series from Pfeiffer. The turbomolecular pump is directly exposed to the chamber environment through the nipple on the bottom, visible in **Fig. 2.1**, to actively pump out the gases from the chamber at pressure of the order of  $10^{-5}$  mbar to the intermediate level of  $10^{-2}$  mbar at its exhaust port, where the inlet of the primary pump is connected to move the pumped gases towards the ambient.

The chamber is large enough to host a sample sized 140 mm x 150 mm suspended by four stainless-steel springs hooked on 1 mm holes on the edges of the sample. Dimensions of the absorber and chamber are not random, but they reproduce the vertical and horizontal pitch of pin rack support to sustain the glass of the TVP Solar SA panel, as already described in the previous section 1.1. The scope of this device is to replicate an environment for the absorber to be tested that was radiatively like the single absorber unit among the holes to host the pin rack, having the glass and the vessel directly exposed. The test facility has no pipeline carrying the working fluid because the objective of this experimental setup is to isolate the radiative properties of the absorber from other thermal mechanisms.

The pressure is measured during each test with a vacuum gauge (Compact Full Range Gauge from Pfeiffer) through a nipple placed on a lateral wall of the chamber. Temperatures of absorber, glass and walls of the envelope are measured by K-type thermocouples whose wires leave the vacuum chamber through a custom-made feedthrough, made in silicone for vacuum applications, and then attached to an electronic module (National Instruments 9162). The tip of the absorber thermocouple is crimped to a ring terminal and attached to an M3 stainless-steel bolt fixed in a hole on the sample's centre, while the other two are stucked to the glass and the vessel with Kapton adhesive, proper for vacuum applications. It is worth mentioning that glass' and vessel' s temperatures are measured within the vacuum environment. This is motivated by the fact that external air convection, natural or forced, would have affected the reproducibility and noise of the measurements.

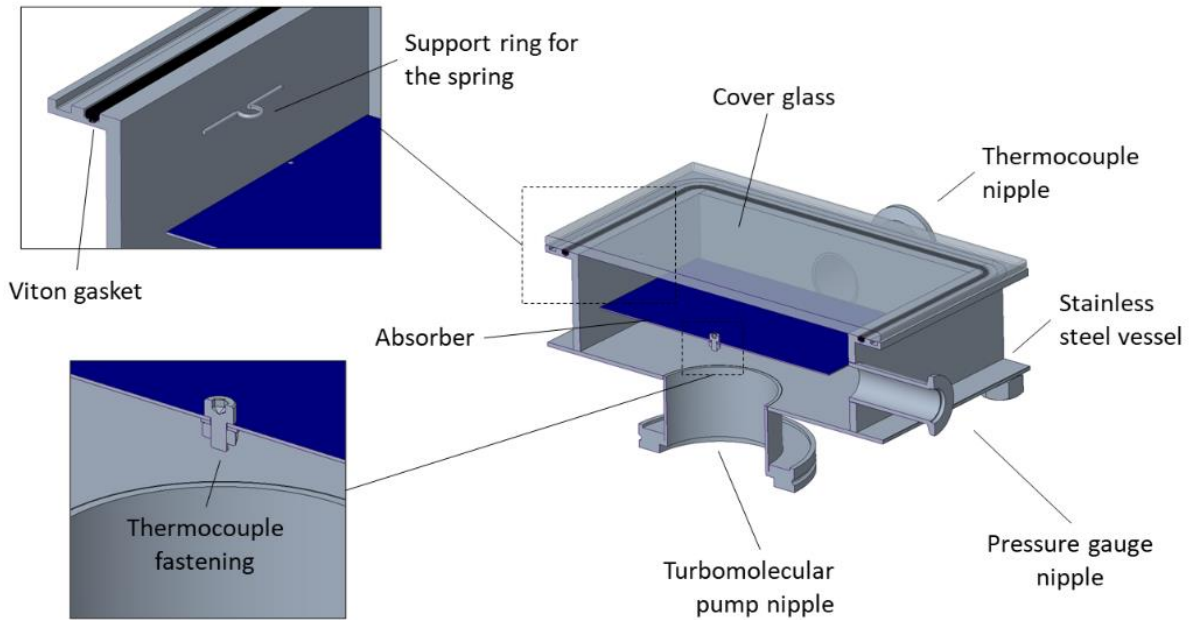


**Fig. 2.1** The section view of the designed vacuum chamber is reported together with two zoom-in pictures of some details.

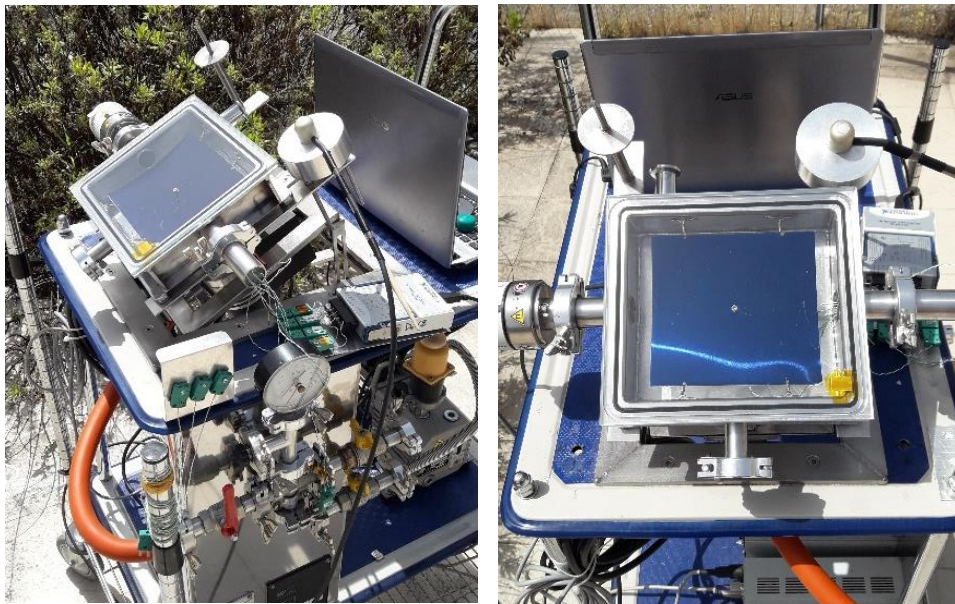


**Fig. 2.2** The presented device for calorimetric testing of absorbers is depicted in its outdoor configuration (lateral view on the left and frontal view on the right). The whole system is mounted on a flatbed trolley and all the measured quantities are recorded by the laptop on the back of the chamber.

The whole system (vacuum chamber, pumping system, measurement probes and electronics) is mounted on a flatbed trolley to ease its mobility. In **Fig. 2.2(a)**, the device is depicted in its configuration for outdoor testing. The vacuum chamber is equipped with a tilt support to set an angle with the vertical consisting of two slotted rods manually fixed by two screws. A meridian and a pyranometer are attached parallelly to the chamber to check the

perpendicularity and measure the intensity of the solar irradiation incident over the glass, respectively. The pyranometer used is thermopile-type from Apogee with response time of 0.5 s, measurement repeatability less than 1% and a calibration uncertainty of 5%. In addition, a secondary pyranometer (CMP11 from Kipp & Zonen), with a lower uncertainty of 1% and larger response time of 5 s, was used to accurately normalize the average value of the high speed pyranometer. By the double pyranometer measurement, we took advantage of the high-speed response of the first and accuracy of the second. All the measured quantities (thermocouples, pressure gauge and pyranometer reading) are recorded with 1 s time step.

## 2.2. Design of the LED-based Solar Simulator

To perform indoor tests, the system needs a solar simulator capable to illuminate the absorber with a controlled and uniform power density as high as  $1.0 \text{ kWm}^{-2}$ . Classes of solar simulators are defined according to international standards [39], taking into account three parameters: non-uniformity, spectral match and temporal instability.

According to one of the most used standard, IEC 60904-9 [40], solar simulators can be identified with classes of merit (A, B or C) based on the deviation of specific parameters from the ideal condition of solar irradiation and are reported in **Tab. 2.1**. Spatial non-uniformity and temporal instability share the same limits of 2%, 5% and 10% respectively for class A, B and C. For the spectral match, the maximum accepted deviation must be satisfied simultaneously in all spectrum intervals, shown in **Tab. 2.2**, respecting the proposed fractions of **Tab. 2.1**. It is worth noticing that the spectral ranges of **Tab. 2.2** start from 400 nm and stop at 1100 nm, even if the solar spectrum has notoriously another half of its intensity above that threshold. All the standards for solar simulators, just as the reported IEC 60904-9, are built to match the requirements of photovoltaic solar cells, whose light-to-current conversion efficiency is negligible above 1100 nm of wavelength due to the bandgap of Si. The strong intrinsic wavelength dependence of photovoltaic absorbers historically constrained the standards to limit the wavelength range of interest. As opposite, thermal absorbers had always had an intrinsically limited variation on the wavelength response, being extremely high absorptive in the whole solar range, so that solar simulators built for photovoltaic applications were suitable also for the thermal absorbers.

**Tab. 2.1** Spectral match, irradiance spatial non-uniformity and temporal instability from the standard of solar simulators IEC 60904-9 [40] are classified as A, B and C.

Classification	Spectral Match (for each interval)	Irradiance Spatial Non-Uniformity	Temporal Instability
Class A	0.75 – 1.25	2%	2%
Class B	0.60 – 1.40	5%	5%
Class C	0.40 – 2.00	10%	10%

**Tab. 2.2** According to the standard of solar simulators IEC 60904-9 [40], the classes of spectral match must be referred to defined fractions of the spectral emitted light power for each range of wavelength. The ranges are below 1100 nm because of the typical threshold of photovoltaic cells.

Wavelength range (nm)	AM1.5 Global Tilt (power fraction in %)
400 – 500	18.4
500 – 600	19.9
600 – 700	18.4
700 – 800	14.9
800 – 900	12.5
900 – 1100	15.9

In literature there are several works about solar simulators designed to emulate the whole solar spectrum, still observing the limits of spatial non-uniformity and temporal instability. Different lamp technologies can be adopted, such as metal halide lamps [41], high pressure xenon discharge bulb [42], [43], LEDs [44] or even a combination of LED and halogen or quartz lamps [45]. The easiest solutions adopt several LEDs with different spectral emissions to match the solar spectrum, but they require a source area much larger than the illuminated one. For instance, Tavakoli et al. employed 19 different wavelength high-power LEDs obtaining class A for spectral match, uniformity and temporal stability simultaneously, but limited to a surface of 2.3 cm x 2.3 cm at 8.7 cm distance from the lamp system [46]. Lopez-Fraguas et al. have recently presented a class A solar simulator based on 14 different peak wavelengths LEDs, but the uniform area was limited to 1 cm<sup>2</sup> [47]. Also Al-Ahmad et al. (2019) have developed a “large area” class A solar simulator (98% uniformity); however, the class A was limited to an area of 20 cm<sup>2</sup>, when extending to an area of 32 cm<sup>2</sup> the uniformity reduces to Class B (95% uniformity). None of those technical solutions could fit our requirements of absorbers as large as 14 cm x 15 cm without building a huge illumination device, heavy and difficult to manage.

One of the most interesting and recent work in literature that describes a solar simulator that would fit our requirements of calorimetric testing was presented by Moss et al. in 2018. Their application was testing a selective solar absorber placed in a flat vacuum envelope and they proposed, as solar simulator, a device consisting of four quartz halogen bulbs inserted in a reflecting envelope to increase uniformity. The system presents class B uniformity on a large area (50 cm x 50 cm), but it is bulky, heavy, and far from being easily mounted on the carter of our calorimetric facility, as they showed in their article, see in **Fig. 2.3** [49]. Moreover, the use of halogen quartz lamps produces a large fraction of IR radiation outside the solar spectrum that is absorbed by the cover glass, which is opaque above about 2.5 μm, and is responsible of an unwanted glass heating. Any increase of the glass temperature due to mechanisms not observable during the real outdoor operation would lead to failure our goal to reproduce realistic operating conditions of the panel-like chamber in its indoor configuration.

In this scenario of solar simulators, the proper device to be used for our calorimetric testing was to be designed from scratch. A novel cost-effective solution is proposed as alternative to the expensive commercial simulators, which are designed according to the strict

international standard for photovoltaic cells, and overcoming all the available complex prototypical devices described in literature, since they are far from being easily replicated and placed on the carter of our test facility.



**Fig. 2.3** The picture of a solar simulator for testing thermal absorbers as is shown in a recent paper [49]. The use of a reflecting envelope improves the uniformity of the incident light over the sample, but the encumbrance and the unwanted IR glass heating due to the halogen lamps makes this solution not feasible for our application.

First part of the designing process is the choice of the type of lamp to be used. High intensity white LED array can be very advantageous in terms of reduction of unwanted IR radiation, reduced system dimensions, high electric-to-light conversion efficiency, adjustable emitted power and low production cost [50]. The main limit of LED arrays is the reduced width of the wavelength range of emission, that is commonly close to the visible. Fortunately, thermal absorbers have a spectral response with a reduced wavelength dependence in the solar spectrum, so that even spectrally unmatched light sources can be effectively used.

The basic idea is of four LED arrays symmetrically disposed at the corners of a square, which is parallel to the illuminated surface. Each single emitter is an integrated LED array (CXA 3590 from CREE), resulting in a 30 mm diameter lamp, see **Fig. 2.4(b)**, with a Lambertian light emission distribution, **Fig. 2.4(a)**, and a light emission confined in the visible range, **Fig. 2.4(c)**. Lambertian emitters have an angular distribution of emitted light that follows the cosine law with viewing angle  $\theta$ , eq. 2.3 .

$$E(r, \theta) = E_0(r) \cos^m \theta \quad 2.3$$

where  $r$  is the distance from the source,  $E_0(r)$  is the corresponding irradiance on the axis and  $m$  is equal to 1 for Lambertian sources [51].

Uniformity can be defined by  $E_{max}$ ,  $E_{min}$  and  $E_{mean}$  which are the maximum, the minimum and the mean power density of the irradiance  $E = E(r, \varphi)$  calculated on the illuminated surface. To quantitatively define non-uniformity,  $\Delta E$  is introduced in eq. 2.4

$$\Delta E = \frac{E_{max} - E_{min}}{E_{mean}} \quad 2.4$$

Where,

$$E_{mean}(R) = \frac{\int_0^{2\pi} \int_0^R E(r, \varphi) dr d\varphi}{\pi R^2} \quad 2.5$$

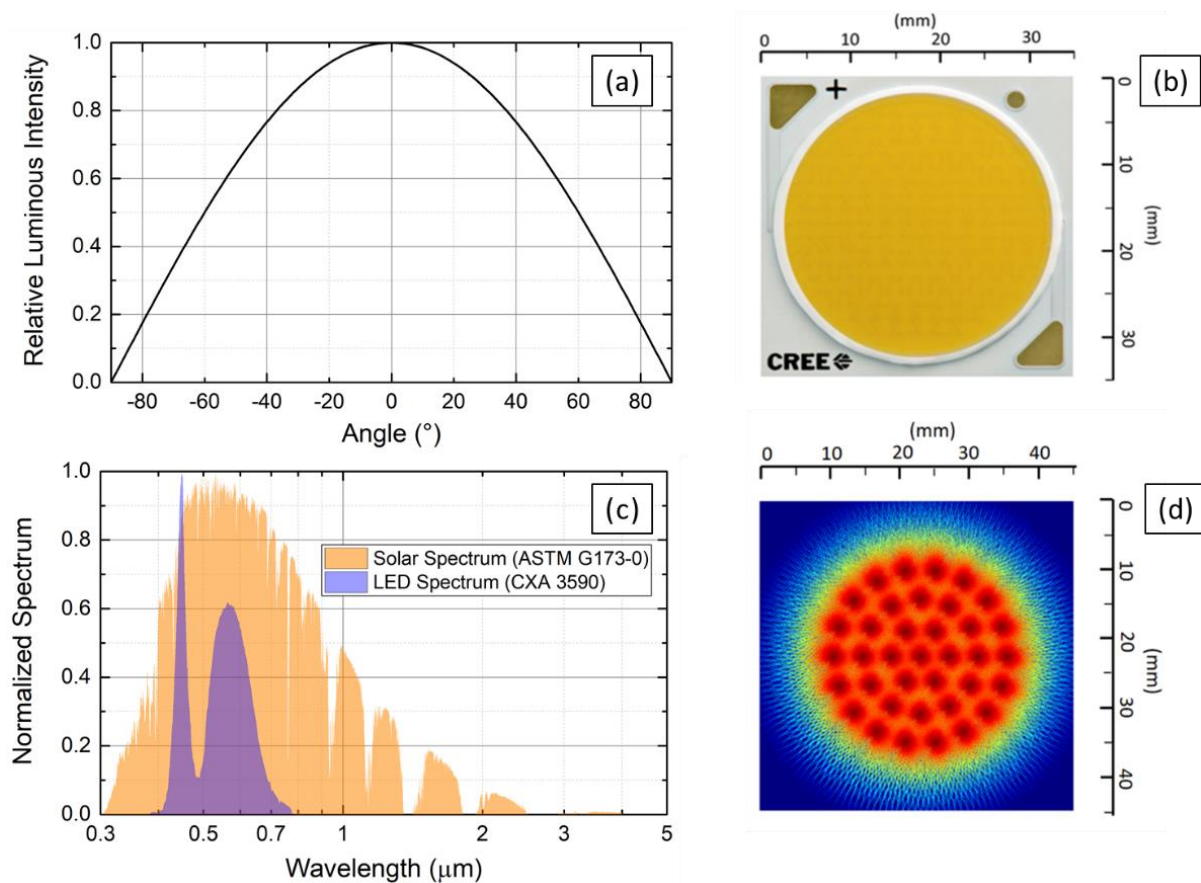


**Fig. 2.4** (a) Angular distribution of the relative luminosity intensity for a single array as reported by the manufacturer [52]. (b) Picture of multi-die integrated LED array forming a single lamp (top view). (c) The normalized spectrum of the adopted LED CXA 3590 from CREE is compared to the solar spectrum (standard ASTM G173-0) [52]. (d) The ray tracing simulation reproduce the single LED array lamp by use of 37 equally spaced point-sources of light emitting 30,000 rays each.

For the described configuration there are two geometrical distances to be chosen, the pitch (P) between two adjacent LED arrays' centres and the LED-to-surface (LS) distance. These are

the two parameters to be selected to maximize uniformity still guaranteeing high power intensity.

The optimization process was carried out through simulations of the incident light power map over the illuminated surface 200 mm x 200 mm wide. It is wider than the absorber to be tested (140 mm x 150 mm) to guarantee the full characterization of the LED device. Comsol Multiphysics was adopted to simulate the emitted light by each LED array by means of the ray tracing approach. Ray tracing consists of simulating the emitted light by a point-like emitter through a finite number of rays. They all start from the same point of origin but move forward with different directions, angularly distributed according to the Lambertian law of emission, eq. 2.3. The adopted LED lamp is numerically simulated by 37 point-sources equally spaced within the diameter of 30 mm, each emitting 30,000 rays or 1.5 rays/sq. deg (about 5 rays/msr) on average, see **Fig. 2.4(d)**.

The origin of the coordinate system is at the centre of the illuminated surface, which in turn is on the x-y plane ( $LS = 0$  mm), whereas the LEDs are placed on a parallel plane at a positive distance  $LS$  along the z axis. In **Fig. 2.5**, the simulated irradiance maps and iso-power density lines, referred to uniformity classes A, B and C, are reported for two configurations, the single centred and the four LED arrays configurations.

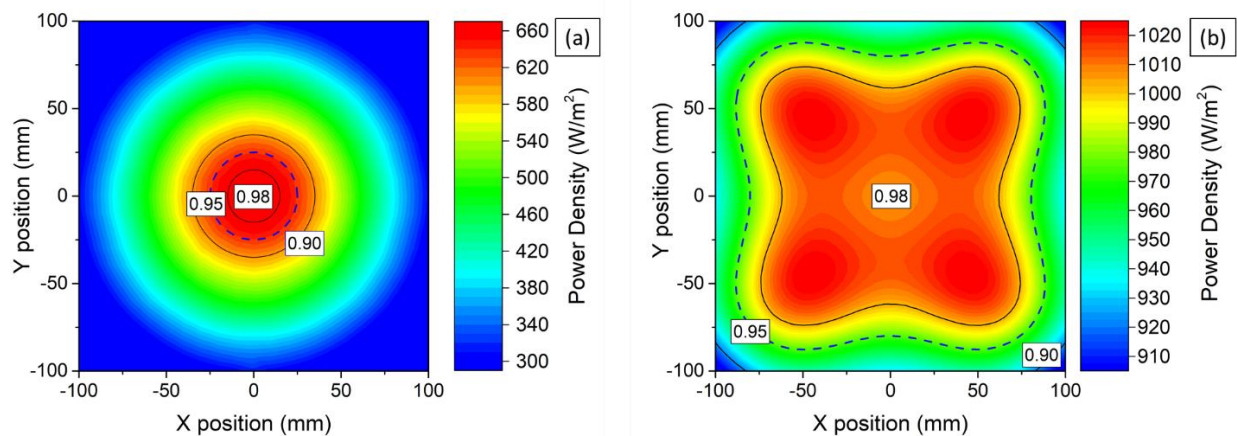


**Fig. 2.5** The simulated power density colormaps and iso-power density lines (black for 0.98 and 0.90, dashed blue for 0.95) on the illuminated 200 mm x 200 mm surface with each LED array emitting 43 W of light power. (a) Single LED array placed at (0, 0) mm,  $LS = 150$  mm. The power density is maximum at the array centre and has a steep decrease along the radius. (b) Four LED arrays with  $P = 160$  mm and  $LS = 150$  mm: the line of 90% uniformity is present only at the edges of the colour map.

**Fig. 2.5(a)** refers to a single LED array emitting 43 W of light power, distributed among all the rays, when centred at (0 mm, 0 mm) at a  $LS$  distance equal to 150 mm. It shows the intrinsic non-uniformity of the LED array emission reaching the class A uniformity only on few  $\text{cm}^2$ . In **Fig. 2.5(b)**, the use of four identical LED lamps (with  $LS = 150$  mm and  $P = 160$  mm) emitting the same 43 W each, increases both light intensity and uniformity over the investigated surface. It can be observed that iso-density profiles have a square-like shape (in agreement with the LED array arrangement) and that the class A uniformity in the central zone extends on an area of about  $120 \text{ cm}^2$ , the class B on an area of about  $250 \text{ cm}^2$ , and class C on almost all the  $400 \text{ cm}^2$  investigated. The minimum values of intensity are along the midlines

of the square, whereas the peaks are on the oblique lines. It is also worth noticing that the positions of the four power density peaks do not match those of the LED arrays (the peaks are slightly shifted towards the centre along the diagonals). This effect is due to the superposition of the emitted light by the four lamps in the central zone, on the contrary this cannot happen in the outer region where no superposition could occur.

A series of numerical simulations were carried out varying  $P$  and  $LS$  parameters to assess the illumination uniformity, defined by  $\Delta E$  expressed in eq. 2.5, on circular areas of radius  $R$ . The  $P$  value was limited to 160 mm because the whole illumination system is required to fit on the carter of the facility. **Fig. 2.6** shows the results obtained in the four LED arrays configuration in terms of the non-uniformity parameter  $\Delta E$  and its complement as function of the radial distance. The maximum uniformity is found for  $P = 160$  mm and  $LS = 150$  mm (the same configuration showed in **Fig. 2.5(b)**), with a  $\Delta E$  less than 2% and 5% on an illuminated area of 50 mm and 70 mm radius respectively. Varying  $LS$  in between 140 and 160 mm, still provides high uniformity with  $\Delta E$  respectively below 3% and 5%. A 20 mm smaller pitch distance ( $P = 140$  mm) is required to observe a variation, at least for larger radii. Such results indicate that a slight variation of  $P$  or  $LS$  from the previous optimal values of 160 mm and 150 mm, respectively, does not severely affect uniformity. This simplifies the experimental set-up assembly where millimetric assembly accuracy is enough to guarantee the required performances. It should be noted that the data reported in **Fig. 2.6** represent the minimum distance from the centre on which the uniformity is preserved, whereas in the colour map reported in **Fig. 2.5(b)** the iso-power density lines represent the maximum area on which the required uniform can be achieved.

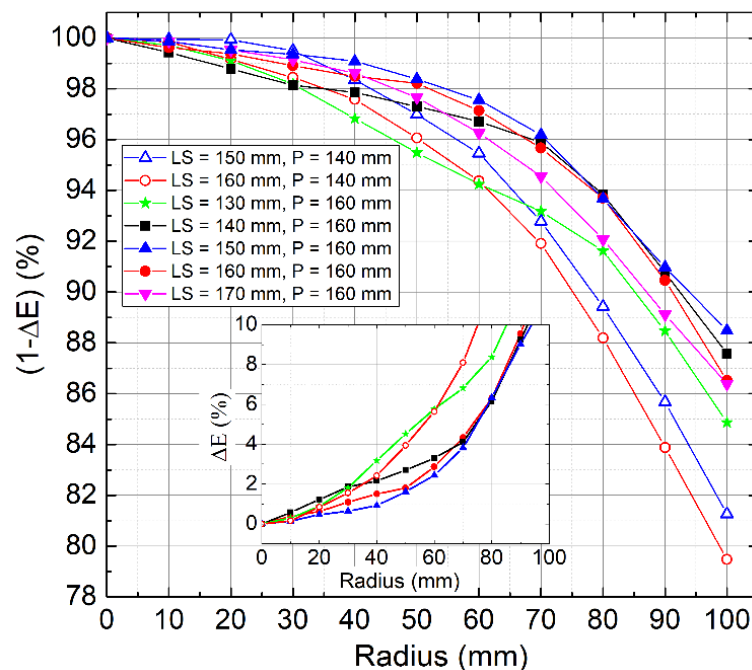


**Fig. 2.6** Variation of non-uniformity parameter (and its complement in the inset) for different  $P$  and  $LS$  values as a function of the radius of the illuminated surface in the configuration with the four LED arrays. The inset shows details of the high uniformity zone.

The mean power density  $E_{\text{mean}}$  is also computed as function of the radius of the illuminated area for different LS values ( $P = 160$  mm), see **Fig. 2.7(a)**. As expected, the bigger LS values, the lower the mean power density, and this reduction effect can be roughly estimated at 0.3% per millimetre ( $100 \text{ Wm}^{-2}$  for 30 mm). Proper knowledge of power density derivative along the radial direction can also be useful to quantify errors related to sample positioning in the x-y plane. For all the geometrical configurations previously analysed and for a sample mis-positioning of few millimetres, we found a variation that would reflect in a total mean power density error below 1%, see **Fig. 2.7(b)**.

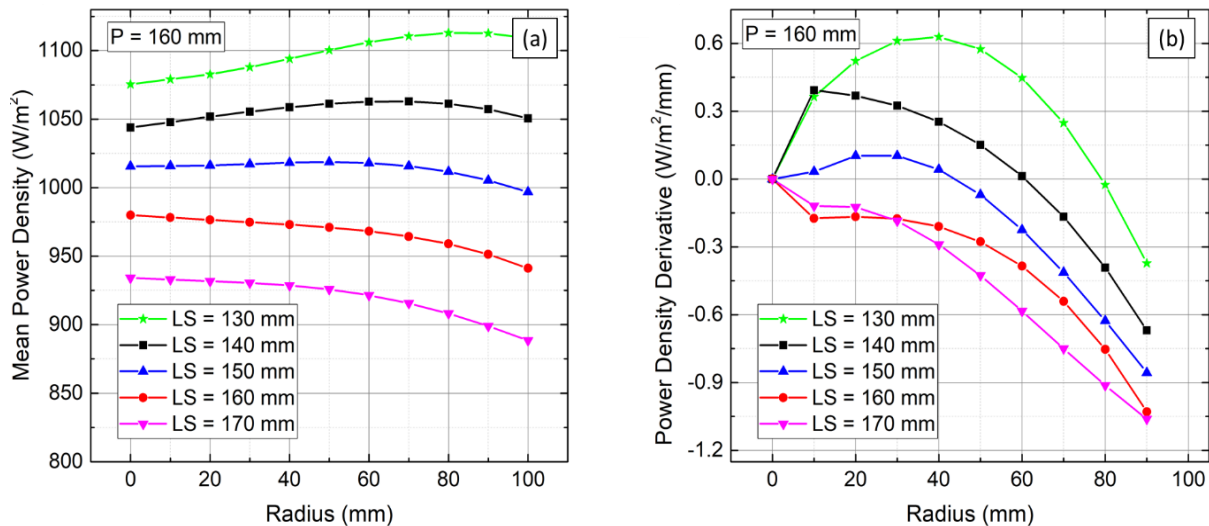


**Fig. 2.7** (a) The mean value of irradiance,  $E_{\text{mean}}$ , on the illuminated surface for different LS values ( $P = 160$  mm). The light power emitted by each LED array is 43 W. (b) For the same configurations, the mean power density derivative along radial direction as a function of the radius of the illuminated surface is reported.

Note that the amount of light power that reaches the illuminated surface is only a fraction of the total emitted by the four LED arrays (ranging from 20% to 26%, for LS of 130 mm and 170 mm respectively). Such light loss, mainly spilling from the sides, might make the workroom less comfortable and should be reduced. For this reason, the experimental apparatus has been equipped with black screens to optically isolate the illumination chamber. These screens have been experimentally characterized by means of reflectivity measurements performed with Integrating Sphere coupled to the Optical Spectrum Analyzer reporting about 96% of absorbance in the visible spectrum. The presence of such screens was simulated too with the ray tracing simulation and no impact could be observed in the whole spatial region of class B uniformity for the optimal configuration  $LS = 150$  mm and  $P = 160$  mm.

Once the potential performances of the proposed LED based system were calculated, the experimental setup was built. It consists of four LED arrays mounted on six rectangular stainless-steel bars assembled using bolts and nuts; slots in the bars allow to adjust the pitch distance  $P$ , see **Fig. 2.8(a)**. The LED lamp is mounted on a supporting structure containing all the control electronics as shown in the picture **Fig. 2.8(b)**. The guides in the support pillars allow to adjust the LS distance according to the actual vertical position of the absorber to be tested. The whole system (including the control electronics) fits in a volume of  $70 \text{ cm} \times 37 \text{ cm} \times$

37 cm, therefore representing a suitable workbench solution for general purpose laboratory activities.

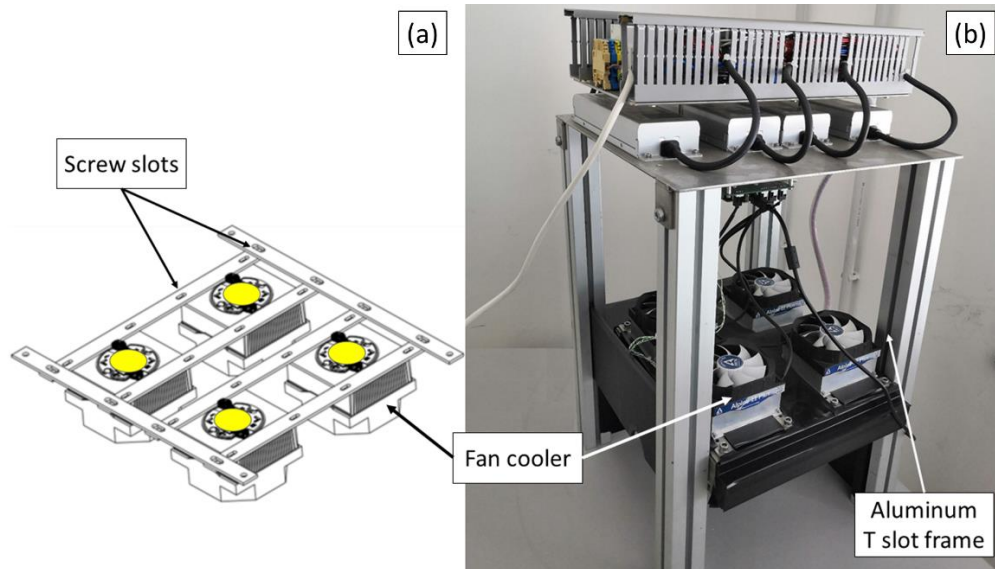


**Fig. 2.8** (a) The LED lamp is composed of four identical LED arrays, symmetrically arranged with a pitch distance of 160 mm, which can be modified by screw slots. (b) The supporting structure is designed to accommodate the electronic control and to make the LS distance tuneable via the T-Slot in the aluminium frame.

Each LED array is powered by its own LED driver ELG-200-C1750 (from Mean Well) and the light output can be controlled by an external 0-10 V DC voltage acting as dimmer. The whole LED system is controlled by a combination of a custom PCB board, a National Instruments (NI) USB-6008/6009 OEM device and a LabView software. The dimmers of the four LED drivers are controlled by analog outputs of the USB NI board. Because the NI board is equipped with just two analog outputs, one output controls two LED drivers. Also, these outputs range from 0 to +5 V, while the dimmer requires 0 V to +10 V for dimming and therefore voltage doubler circuits are provided on the custom PCB board. The four voltage doubler circuits can be fine regulated by means of trimmers. This feature is used to equalize light output by placing a pyranometer directly under the four individual LED arrays.

LED arrays are turned on and off using two digital outputs of the NI board, driving solid state relays of appropriate power rating. Again, one digital output controls two LED drivers simultaneously. LED array temperatures are monitored with a K-type thermocouple attached to the chip socket and readings performed using a precision thermocouple amplifier with cold junction compensation (from Analog Device), connected to an analog input channel of the NI Board. The luminous flux emitted by the LED arrays strongly depends on the LED temperature [52]. We therefore mounted each LED array chip on a modified CPU cooler of double power rating [55]. Such solution allows to keep the LED temperature stable during operation at values below 75 °C for any applied bias voltages.

The experimental characterization of the LED array assembly has been conducted by using the same secondary standard pyranometer (CMP11 from Kipp & Zonen) with 1% precision and a response time of about 5 s. Firstly, a time-stability test has been conducted, see **Fig. 2.9(a)**: the pyranometer is placed under the four LED arrays ( $P = 160$  mm) at  $LS = 150$  mm and (0 mm, 0 mm) x-y coordinates, i.e., in the centre of the illuminated area. The LED

arrays' control voltage is 6.5 V and the power density is read out together with LED array temperature. Just after the switching on, the LED array delivery about 3% more power than the set value (class B), however, after 10 minutes of illumination the power delivered is only 2% higher than the set value, and after 30 min of illumination, the measured power density becomes stable in time within 1% uncertainty of the pyranometer reading, making the device class A in terms of long temporal instability.

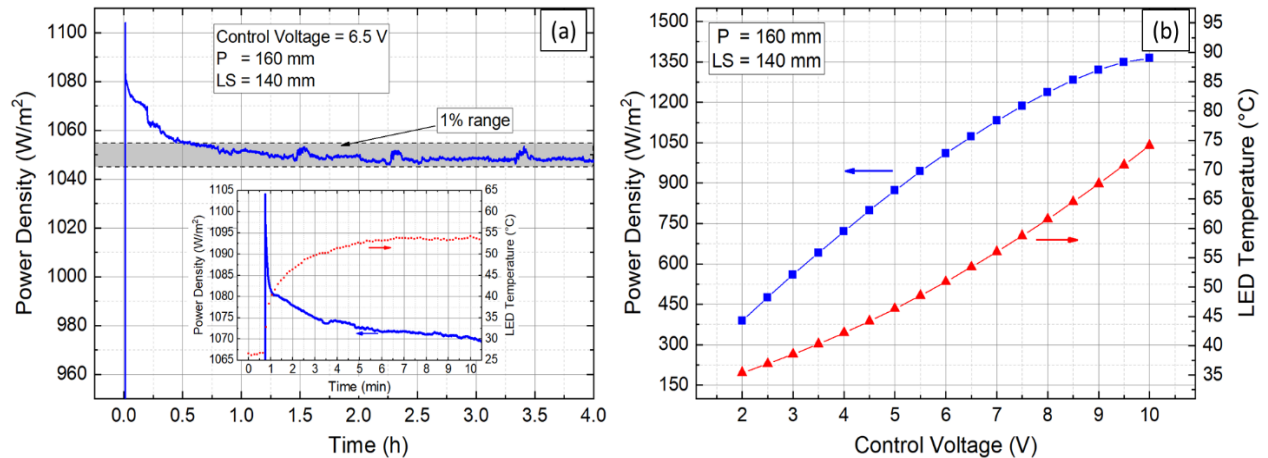


**Fig. 2.9** LED array light output stability measured at the centre of the illuminated surface. (a) Evolution of light power density with time: the gray box indicates 1% range of uncertainty around the steady state level. The inset shows the inverse correlation between emitted power and LED operating temperature. (b) Steady state power density and operating temperature as a function of control voltage (error bars are within the data points).

In particular, the inset of **Fig. 2.9(a)** reveals that the reduction of power output with time can be directly linked to the thermal stabilization of the LED source. The temporal measurement of the emitted light power density has been carried out also for additional control voltages ranging from 2.0 V to 10.0 V with step 0.5 V. Similarly to the case of 6.5 V, all the measures showed stable power output after 30 min from the switch on: their stabilized power density and temperature values depend on the control voltage as reported in **Fig. 2.9(b)**. Power density level can be varied from  $392 \text{ W m}^{-2}$  up to  $1360 \text{ W m}^{-2}$ , with almost perfect linearity, making the device suitable for both low and high intensity applications with class A long term temporal instability.

To validate the numerical simulations performed with the ray tracing approach, three light maps were experimentally measured for a fixed pitch of 160 mm and three LS distances. The black dots in **Fig. 2.10** represent the pyranometer measurement positions: 96 points radially disposed on the maximum  $200 \text{ mm} \times 200 \text{ mm}$  illuminated surface with a step of 10 mm (equal to the pyranometer probe diameter). Radial mapping is preferred, since power density peaks and valleys are expected to be along diagonals and symmetry lines, as showed in **Fig. 2.5**.

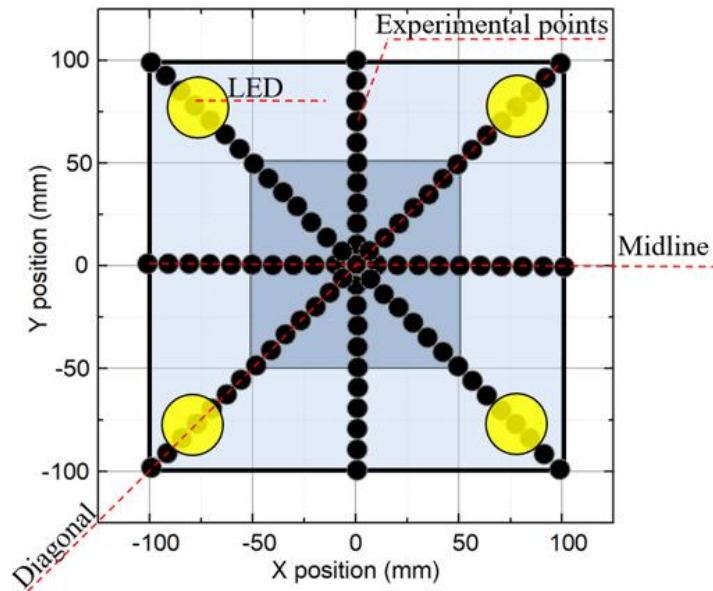


**Fig. 2.10** Spatial arrangement of the experimental validation. The yellow circles represent LED array positions at  $P = 160$  mm. The black dots represent the positions where light power density was measured with the secondary standard pyranometer.

The experimental results obtained for a control voltage of 6.5 V and a LS distance of 130, 140 and 150 mm are summarized in **Fig. 2.11(a)** and compared to the corresponding numerical simulation. Each experimental point is obtained by averaging the eight experimental data acquired at the same radial distance from the centre (the error bars represent 1% uncertainty from the pyranometer calibration). A very good accordance was found, proving that the numerical model is reliable and properly validated.

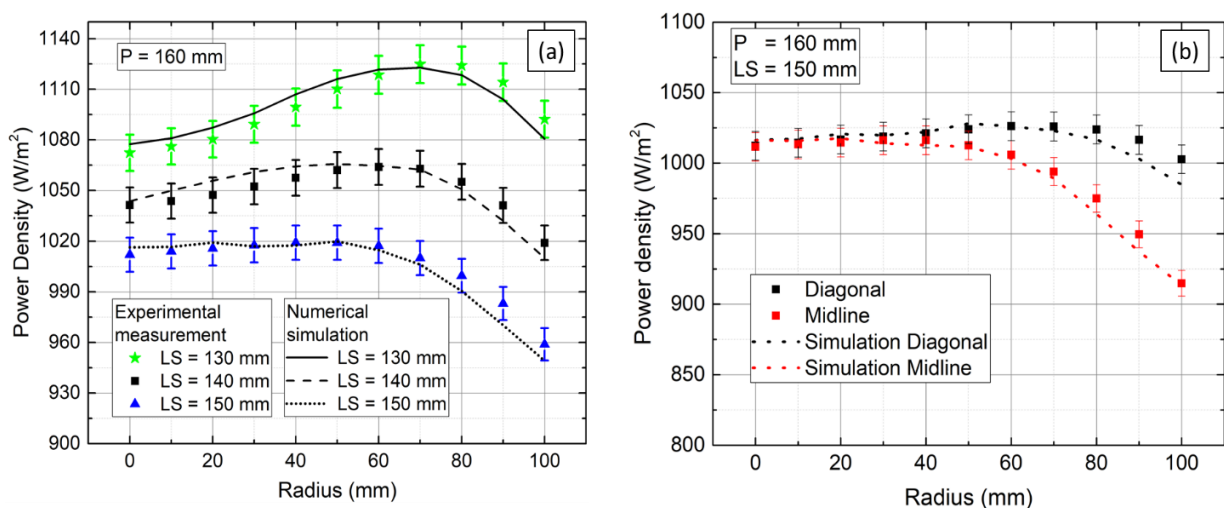


**Fig. 2.11** (a) Power density average on 8 points measured at each reported radius (dots) and simulation result in the same points (lines). (b) Comparison between simulated and experimental results along symmetry and diagonal lines. In (a) and (b) the measured point error bars refer to 1% pyranometer uncertainty.

The same accordance was observed when analysing the power density along the midlines and the diagonals as shown in **Fig. 2.11(b)** for the optimal configuration of  $P = 160$  mm and  $LS = 150$  mm. The accurate characterization of this system guarantees an extremely precise estimation of the power incident over the cover glass of the vacuum chamber of the order of 1%.

The proposed LED based solar simulator was then mounted on the flatbed trolley in its optimal configuration ( $LS = 150$  mm,  $P = 160$  mm) to perform indoor calorimetric tests, see **Fig. 2.12**. The contained dimensions of the overall system and the black screens make the presented test facility an easy-to-manage tool involving no constraints for laboratory spaces and users. The design and the characterization of the described LED device is subject of our recent publication [56].

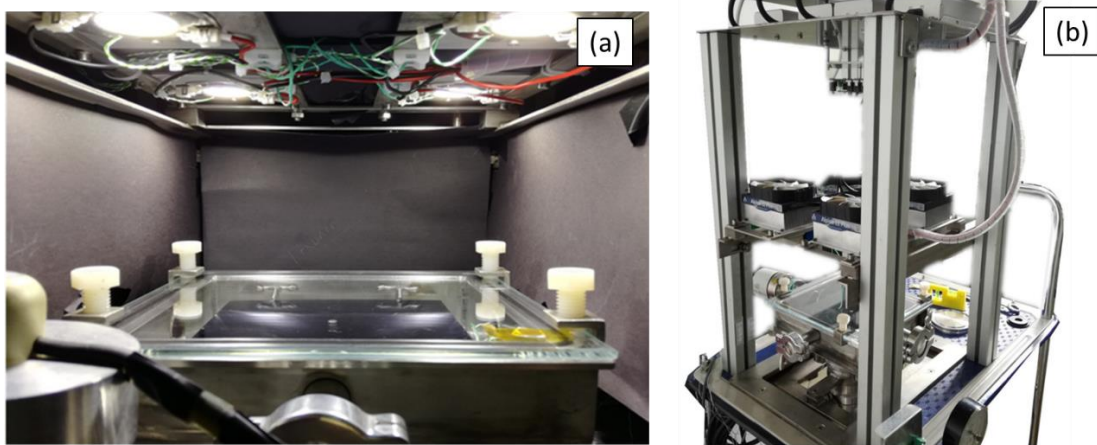


**Fig. 2.12** The indoor configuration of the proposed calorimetric test facility is shown. The adopted solar simulator was designed to fit on the carter and its optimized configuration was used. (a) Picture of the internal side of the protecting black screens during the test. (b) The picture of the system, without the black screens, shows how the whole system has very contained geometrical overall dimensions.

### 2.3. Calorimetric Equation

In this section the calorimetric eq. 2.1 is detailed for the absorber during the test within the presented test facility and proposed in a form suitable to extrapolate the radiative properties of the investigated absorber as function of the temperature derivative.

The vacuum inside the chamber is kept actively by the pumping system guaranteeing a pressure never above  $5 \times 10^{-5}$  mbar during all the conducted tests. Coupling this pressure threshold to a characteristic distance absorber-glass and absorber-vessel of 2 cm, the impact of the conductive losses due to the residual gas can be neglected and not considered in the formulation of the calorimetric equation, as demonstrated by the kinetic theory of ideal gas in the previous section 1.1.

The contact between the sample and the stainless-steel supporting springs is another potential cause of conductive thermal loss. In the worst-case scenario this contact is perfect, and the two spring's ends are exactly at the absorber's and chamber's temperatures,  $T_{abs}$  and  $T_{amb}$ , respectively, dissipating heat via conduction and radiative emission towards the

chamber. The following differential equation 2.6 governs the temperature distribution over the length of a straight wire under hypothesis of steady-state condition and round section [57].

$$\frac{d^2T}{dx^2} = \frac{4\varepsilon_{\text{wire}}\sigma}{k_{\text{wire}}D_{\text{wire}}}(T^4 - T_{\text{amb}}^4) \quad 2.6$$

$T$  is the temperature of the wire at the spatial coordinate  $x$ .  $k_{\text{wire}}$ ,  $D_{\text{wire}}$  and  $\varepsilon_{\text{wire}}$  are the wire's thermal conductivity, diameter and thermal emittance, respectively. Assuming  $x = 0$  at the contact with the sample, the corresponding heat loss through the wire can be written as eq. 2.7:

$$\dot{Q}_s = \frac{\pi}{4}D_{\text{wire}}^2k_{\text{wire}}\left.\frac{dT}{dx}\right|_{x=0} \quad 2.7$$

Thanks to the finite element method, the differential eq. 2.6 can be solved and **Fig. 2.13(a)** shows the resulting temperature distribution as  $T - T_{\text{amb}}$  when  $D_{\text{wire}}$  is 0.45 mm,  $\varepsilon_{\text{wire}}$  is 0.15,  $k_{\text{wire}}$  is  $17 \text{ Wm}^{-2}$ ,  $T_{\text{amb}}$  is 303 K, and sample's temperature is 400 K above the surrounding chamber ( $T_{\text{abs}} - T_{\text{amb}} = 400 \text{ K}$ ). The distribution is roughly linear, meaning that the conduction mechanisms is dominant than radiation towards the chamber. In **Fig. 2.13(b)** the thermal loss calculated by eq. 2.7 is reported as power per unit of  $140 \text{ mm} \times 150 \text{ mm}$  sample's area when four supporting springs are in thermal contact. The power density loss is below  $1 \text{ Wm}^{-2}$  while the calorimetric tests are conducted under incident light densities as high as  $1 \text{ kWm}^{-2}$ , so that the impact of the supporting springs is surely negligible and is not accounted in the calorimetric equation of the sample.

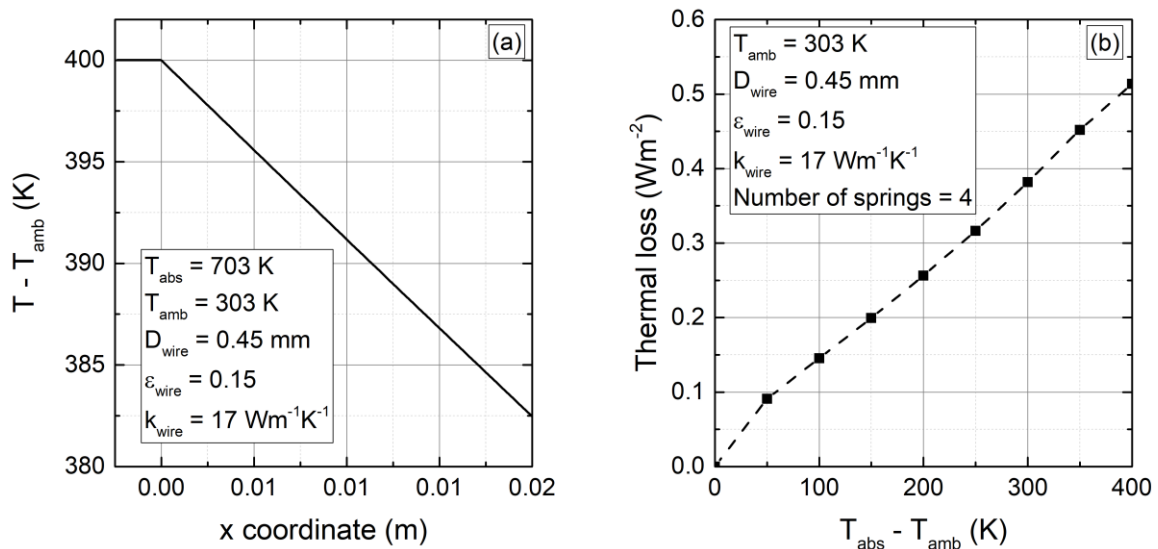


**Fig. 2.13** (a) Temperature distribution over the wire when  $T_{\text{abs}} - T_{\text{amb}} = 400 \text{ K}$  as result of the differential eq. 2.6 solved by finite element method. (b) Thermal loss calculated by eq. 2.7 is expressed in  $\text{Wm}^{-2}$  for four springs with perfect contact to the sample and chamber as function of  $T_{\text{abs}} - T_{\text{amb}}$ . The surface is referred to  $140 \times 150 \text{ mm}^2$  of sample's area.

The presence of the stainless-steel bolt attached to the absorber to fasten the thermocouple is an additional source of loss. It could affect the tests because of its thermal emittance and light absorptance which are likely to be different with respect to the absorber under test. Even if its radiative properties might be far from those of the investigated sample, its exposed surface is more than two orders of magnitude lower, so the role of the bolt is limited to its thermal capacitance which is to be added to the thermal capacitance of the sample. Numerical 3D simulations confirm this assumption and in the following section 2.6 is deeply discussed.

The general calorimetric equation 2.1 can be rewritten as eq. 2.8 according to our specific boundary conditions. The absorber temperature derivative  $dT_{abs}/dt$  is affected only by radiative mechanisms of light absorption and thermal emission, as conduction through the springs and residual gases can be neglected.

$$\frac{(m_{abs}c_{p_{abs}} + m_{th}c_{p_{th}})}{A_{abs}} \frac{dT_{abs}}{dt} = P_{light}\alpha_{light}\tau_{gla} - \varepsilon_{eff-abs}\sigma(T_{abs}^4 - T_{gla}^4) - \varepsilon_{eff-sub}\sigma(T_{abs}^4 - T_{ves}^4) \quad 2.8$$

$m_{abs}$ ,  $c_{p_{abs}}$ ,  $m_{th}$  and  $c_{p_{th}}$  are the mass and specific heat of the absorber and thermocouple fastening, respectively. Commercial flat absorbers are thin metallic foils, as aluminium or copper, coated on one side with a selective absorbing coating. The thickness of the foil is typically few tenths of millimetre, so the overall exposed surface can be approximated just by the area of the two sides of the absorber. Each of the two extends for  $A_{abs} = 140 \text{ mm} \times 150 \text{ mm}$ .  $P_{light}$  and  $\alpha_{light}$  is the light power density incident over the glass of the chamber and the sample' spectrally averaged absorptance, respectively. Depending on the adopted light source,  $P_{light}$  and  $\alpha_{light}$  is written in the text as  $P_{Sun}$  and  $\alpha_{Sun}$  in case of outdoor and  $P_{LED}$  and  $\alpha_{LED}$  for indoor testing.  $\tau_{gla}$  and  $T_{gla}$  are light transmittance and measured temperature of the glass, respectively. The light absorption mechanism is modelled by the product between  $P_{light}$ ,  $\alpha_{light}$  and  $\tau_{gla}$ . The glass transparency  $\tau_{gla}$  was evaluated as the ratio between the reading of the secondary pyranometer when exposed perpendicularly to the incident light underneath and above the glass. For both solar and LED light, the calculated  $\tau_{gla}$  had the same value of 0.915.

The thermal emission mechanism is modelled according to the Stefan-Boltzmann formulation that expresses the radiative exchange with the difference between the fourth power of surface temperatures times an effective emittance parameter. In the equation,  $\varepsilon_{eff-abs}$  and  $\varepsilon_{eff-sub}$  are the effective thermal emittances of the two sides of the sample, the first for the absorbing side facing the glass and the second for the substrate facing the bottom of the stainless-steel vessel at temperature  $T_{ves}$ .

Eq. 2.8 can be rewritten assuming that  $T_{gla}$  and  $T_{ves}$  are represented just by a single temperature  $T_{amb}$  as their arithmetic average. This allows to sum  $\varepsilon_{eff-abs}$  and  $\varepsilon_{eff-sub}$  together to obtain  $\varepsilon_{eff-TOT}$ , as shown in eq. 2.9.  $\varepsilon_{eff-TOT}$  expresses the total effective thermal emittance of the absorber when placed in the panel-like chamber and depends on spectral emissivity and geometry of each surface of the cavity.

$$\frac{(m_{abs}c_{p_{abs}} + m_{th}c_{p_{th}})}{A_{abs}} \frac{dT_{abs}}{dt} = P_{light}\alpha_{light}\tau_{gla} - \varepsilon_{eff-TOT}\sigma(T_{abs}^4 - T_{amb}^4) \quad 2.9$$

This assumption is feasible because during all the tests the maximum difference between  $T_{\text{gla}}$  and  $T_{\text{ves}}$  never exceed 10 K, impacting no more than 1% in terms of radiated power, and so on the calculated  $\varepsilon_{\text{eff-TOT}}$ . Eq. 2.9 is the power balance equation that regulates the sample's temperature  $T_{\text{abs}}$  over time  $t$  for the presented test facility. This equation is adopted to calculate  $\alpha_{\text{light}}$  and  $\varepsilon_{\text{eff-TOT}}$  of the absorber during experimental tests, since all the other quantities can be measured or are already known.

#### 2.4. Measurement Algorithm of the Calorimetric Test

$\alpha_{\text{light}}$  and  $\varepsilon_{\text{eff-TOT}}$  are the outcome of this calorimetric procedure and, to calculate them out of eq. 2.9, the measurement process is divided into two subsequential steps: Warm-Up and Cool-Down phase. The first consists of exposing the sample to the light through the cover glass, letting the temperature of the sample increase up to the stagnation temperature  $T_{\text{stag}}$ . Such a temperature is the maximum reachable, occurring when the radiative emission of the sample equals the absorbed light power. For all the experimental tests the sample was kept at stagnation at least for 10 minutes. The second phase, Cool-Down, consists in letting the sample cool through radiative emission while shielded from any incident light. An aluminium foil is used as shield to externally cover the glass. The data analysis of this procedure starts from the Cool-Down phase. During this phase eq. 2.9 has zero  $P_{\text{light}}$ , so  $\varepsilon_{\text{eff-TOT}}$  can be easily calculated as the only unknown of the equation. Then, the Warm-Up phase is analysed to calculate  $\alpha_{\text{light}}$ , being  $\varepsilon_{\text{eff-TOT}}$  already known from the analysis of the Cool-Down phase.

To qualify the calorimetric test facility, the commercial absorber Mirotherm® from Alanod is adopted. It was already introduced in the previous section 1.2 and consists of an aluminium substrate coated on one side by a selective film for solar thermal applications, while the back is the bare material. This specific absorber is installed within the TVPSolar SA panels for mid-temperature thermal applications, up to 200 °C of operation. In the following section we show results for repeated experiments in both outdoor and indoor configuration for the same sample.

In **Fig. 2.14**, all the measured quantities during a single outdoor test are reported as function of the relative time. The zero of relative time is set at the start of the Warm-Up phase, point A in **Fig. 2.14**. Before this time, the sample is within the vacuum chamber with the system already oriented perpendicularly to the Sun while the glass is covered by the opaque shield. In this condition the sample is at a temperature close to the chamber. When the shield is taken out, the sample is exposed to the solar irradiation and the Warm-Up phase begins, point A in **Fig. 2.14**. During this phase  $T_{\text{abs}}$ ,  $T_{\text{gla}}$  and  $T_{\text{ves}}$  increase simultaneously together with the internal pressure which has never exceeded the threshold of  $5 \times 10^{-5}$  mbar for every experiment. Outdoor tests were conducted around the solar noon of clear sky days to minimize variations of solar irradiation and the maximum recorded variation of  $P_{\text{Sun}}$  over the whole Warm-Up phase was 5% of its initial value in point A. The absorber temperature increases up to the stagnation temperature  $T_{\text{stag}}$ , i.e., when  $T_{\text{abs}}$  derivative is zero, point B<sup>stag</sup>. This condition of  $T_{\text{abs}} = T_{\text{stag}}$  is kept for 10 minutes, then the glass is covered with the shield again, point B, letting the sample cool down to temperature close to ambient, point C.

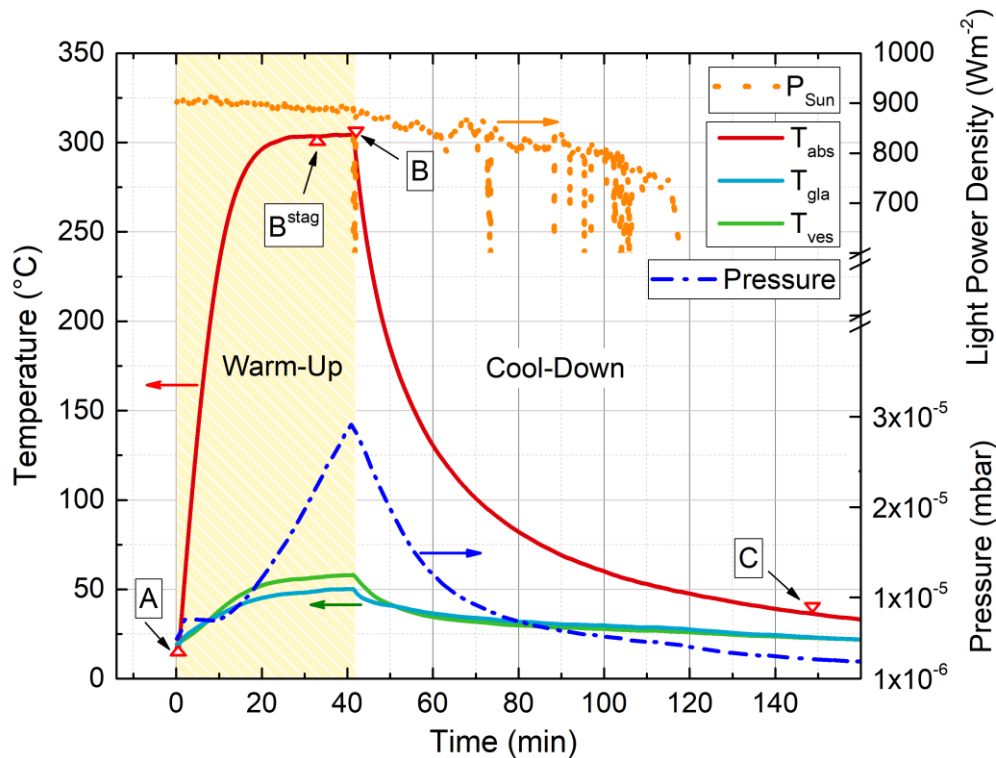


**Fig. 2.14** The measured quantities (absorber, glass and vessel temperature, internal pressure and solar irradiance) during an outdoor experiment are shown. The relative time 0 min starts when the sample is exposed to the solar irradiation (beginning of the Warm-Up phase, point A). Around 40 min, the stagnation temperature  $T_{stag}$  is reached (interval  $B^{stag} - B$ ), then the system is covered by a metallic opaque shield, so that the Warm-Up phase ends while the Cooling-Down phase starts (point B). The Cooling-Down phase continues until the sample's temperature is close to ambient (point C).

In **Fig. 2.15(a)**, the time derivative of  $T_{abs}$  is reported as function of the relative time and as function of  $T_{abs}$  itself in **Fig. 2.15(b)**. Theoretically, the maximum of the sample's temperature derivative is expected at the start of the Warm-Up phase, point A, since thermal losses are minimum, see eq. 2.9. The actual experimental measurement of the temperature derivative reveals the maximum in  $A^*$ , see **Fig. 2.15(a)**, at the end of a time interval after uncovering the glass. As consequence, the measured  $T_{abs}$  derivative reaches its maximum value at  $T_{abs}$  higher than the initial, see **Fig. 2.15(b)**. Through all the conducted experiments, the process A –  $A^*$  takes a time interval of around 1 minute corresponding to roughly 20 °C of temperature shift. This effect is due to the thermocouple fastening that increased the thermal capacity of the probe, also confirmed by numerical 3D simulations discussed in the following section 2.6. Subsequently to A –  $A^*$ , the time derivative of  $T_{abs}$  progressively reduces to zero, point  $B^{stag}$ , as thermal losses increase with the fourth power of the  $T_{abs}$ . During the interval  $B^{stag} - B$  the derivative of  $T_{abs}$  keeps zero and in **Fig. 2.15(a)** it is possible to distinguish  $B^{stag}$  from B, whereas in **Fig. 2.15b** they are overlapped. The point B occurs when the glass is covered again with the opaque shield and the Cool-Down phase starts with negative values of  $T_{abs}$  derivative. Analogously to A –  $A^*$ , but with opposite sign, there is the delay of the measured  $T_{abs}$  derivative also during the Cool-Down phase, interval B –  $B^*$  in figure. It extends for a slightly shorter time interval and smaller temperature shift than A –  $A^*$ . This is due to a lower modulus of  $T_{abs}$  derivative obtained by the increased heat capacity of the sample at

higher temperatures. The last interval of the experiment is B\* – C during which the derivative increases its value up to zero, point C.

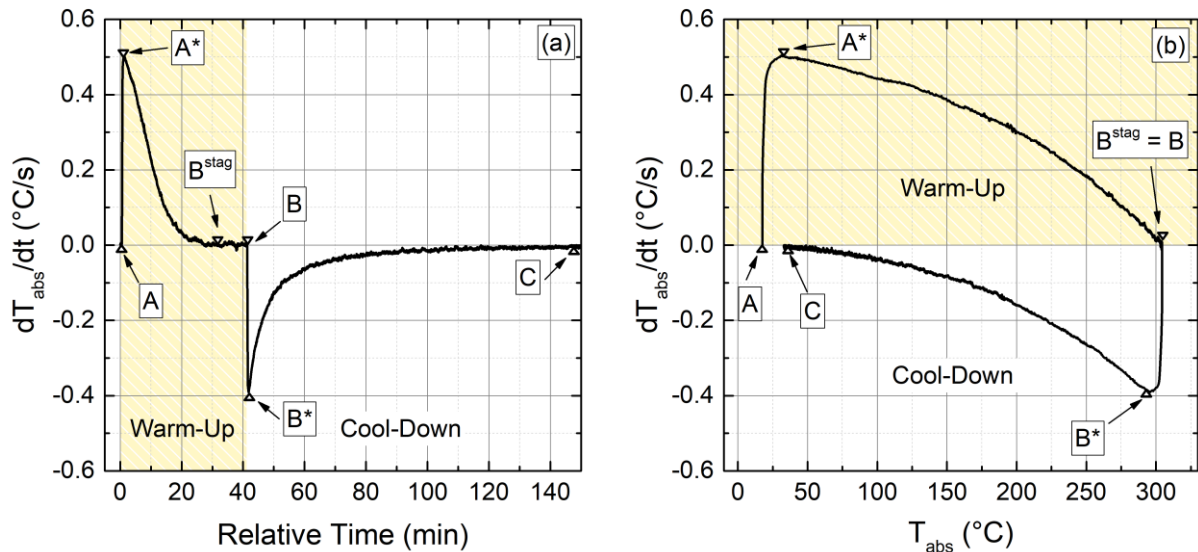


**Fig. 2.15** The time derivative of  $T_{\text{abs}}$  for an outdoor experiment is reported as function of relative time (a) and  $T_{\text{abs}}$  itself (b). The yellow background defines the Warm-Up phase, while the white refers to the Cool-Down.

The indoor measurement algorithm is analogous to that described so far for the outdoor procedure. The chamber is set horizontal, and the LED system is mounted facing the glass. Because of the transient of the emitted light when the LEDs are switched on [56], they had been turned on 30 minutes before the Warm-Up phase while the glass was covered by the opaque shield as well. The Warm-Up phase, just as outdoor tests, was started by the removal of the shield and then stopped by the switch off of the LED system, making the Cool-Down start.

### 2.5. Experimental results: Optical and Calorimetric Approaches

In this section experimental results from calorimetric tests of the Mirotherm<sup>®</sup> commercial absorber are reported and compared to those expected from the traditional optical analysis. Optical reflectivity measurement of spectral emissivity  $\varepsilon_{\lambda}$  was conducted at room temperature for the coated and uncoated side of the absorber.  $\varepsilon_{\lambda}$  allows the calculation of the expected light absorptance and thermal emittance through eq. 1.9 and 1.10, while the radiative interaction glass-absorber and absorber-vessel can be modelled by the theory of infinite parallel radiating plates with eq. 2.2. For sake of clarity and simplicity of the nomenclature, the subscript OPT will be added to all the quantities resulting from the optical analysis of spectral reflectivity and for those without are to be considered as result of calorimetric tests.

In **Fig. 2.16(a)**, spectral emissivity derived from the optical analysis carried at room temperature is shown,  $\varepsilon_{\lambda\text{-abs-OPT}}$  for the coated and  $\varepsilon_{\lambda\text{-sub-OPT}}$  uncoated side of the absorber. From 0.35 to 1.75  $\mu\text{m}$  the analysis was carried using the integrating sphere from Ocean Optics

equipped with a halogen lamp and connected to an Optical Spectrum Analyser through an optic fibre cable. Then, from 1.75 to 20.0  $\mu\text{m}$  the FTIR from Jasco equipped with an integrating sphere was used. The coated side shows a good selectivity with high emissivity values in the solar range (blue dashed line in Fig. 2.16(a)) which rapidly decrease at longer wavelengths. On the other hand, the aluminium substrate returned  $\varepsilon_{\lambda\text{-sub-OPT}}$  (black solid line) lower than  $\varepsilon_{\lambda\text{-abs-OPT}}$ , particularly in the solar range, since there is no selective coating applied on the back. In the same figure, normalized solar spectrum incident on terrestrial surface, standard ASTM G173-0 (orange pattern) is reported together with normalized spectrum of the adopted LED lamps from CREE (violet pattern).

The spectrally averaged light absorptance of the coated side is calculated by eq. 1.9 returning  $\alpha_{\text{Sun-OPT}}$  and  $\alpha_{\text{LED-OPT}}$  of 0.933 and 0.947, respectively. Spectrally averaged thermal emittance  $\varepsilon_{\text{abs-OPT}}$  and  $\varepsilon_{\text{sub-OPT}}$ , relatively to spectral emittance  $\varepsilon_{\lambda\text{-abs-OPT}}$  and  $\varepsilon_{\lambda\text{-sub-OPT}}$ , are calculated through eq. 1.10 at several  $T_{\text{abs}}$  and shown in Fig. 2.16(b).  $\varepsilon_{\text{abs-OPT}}$  is always higher than  $\varepsilon_{\text{sub-OPT}}$  in the whole investigated temperature range 50 - 300  $^{\circ}\text{C}$ , larger by 10% at  $T_{\text{abs}} = 50$   $^{\circ}\text{C}$  up to 40% at 300  $^{\circ}\text{C}$ . This behaviour is a direct consequence of the increase of  $\varepsilon_{\lambda\text{-abs}}$  at lower wavelengths where the radiative emission occurs at higher temperatures.

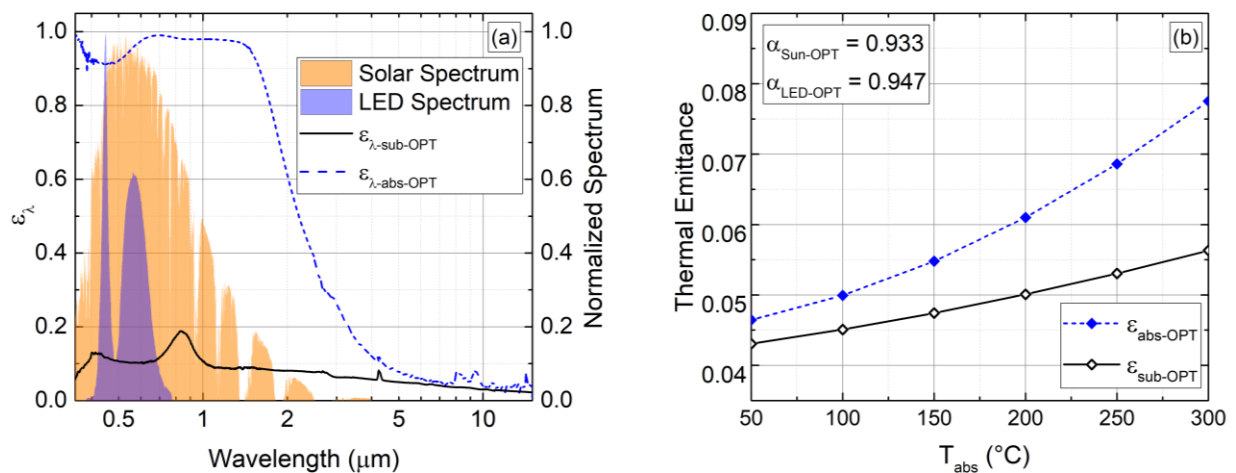


**Fig. 2.16** Results of the optic analysis are reported for both sides of the commercial absorber Mirotherm<sup>®</sup> from Alanod. (a) Spectral emissivity curve of coated,  $\varepsilon_{\lambda\text{-abs-OPT}}$ , and uncoated,  $\varepsilon_{\lambda\text{-sub-OPT}}$ , side was measured by reflectometry and FTIR measurements at room temperature and are shown as function of wavelength. Also normalized solar spectrum, ASTM G173-0 standard, and spectrum of the adopted LED system are reported. (b) Thermal emittance of coated,  $\varepsilon_{\text{abs-OPT}}$ , and uncoated,  $\varepsilon_{\text{sub-OPT}}$ , side is calculated through eq. 1.10 and reported as function of  $T_{\text{abs}}$ .

Together with the optical characterization, also the calorimetric measurement campaign was carried out.  $\alpha_{\text{light}}$  and  $\varepsilon_{\text{eff-TOT}}$  resulting from 12 calorimetric tests, 6 performed outdoor and the other 6 indoor are reported. In case of outdoor testing, all the experiments, from #1 to #6, consist in exposing the test facility to solar irradiance without any external fan to cool the chamber walls. Indoor tests were conducted under the following controlled conditions, tests #1 and #2 refer to  $P_{\text{LED}}$  close to 1  $\text{kWm}^{-2}$  while the chamber is externally cooled by an electric

fan. Test #3 has similar  $P_{LED}$  but with no fan system for external cooling. Tests #4, #5 and #6 were performed without external cooling too, but at reduced  $P_{LED}$ .

In **Fig. 2.17(a)**,  $\epsilon_{eff-TOT}$  resulting from one of the analyses of the Cooling-Down phase (grey line) is reported as function of  $T_{abs}$  and the points B, B\* and C are indicated. At the start of the Cool-Down phase, point B, the calculated  $\epsilon_{eff-TOT}$  is zero. At lower  $T_{abs}$ , as the cooling progresses, there is an increase of calculated  $\epsilon_{eff-TOT}$  up to more realistic values, point B\*. This anomaly is due to the thermocouple fastening and is driven by the shape of  $dT_{abs}/dt$  in B – B\*, as seen in **Fig. 2.15**, affecting the calculated  $\epsilon_{eff-TOT}$  in the first moments of the Cool-Down phase for roughly 10 °C starting from  $T_{stag}$ . In the following interval B\* – C, the calculated  $\epsilon_{eff-TOT}$  reduces together with  $T_{abs}$ , as even expected from the optical analysis of the coated and uncoated side, see **Fig. 2.16(b)**. As the sample approaches point C, the calculated  $\epsilon_{eff-TOT}$  becomes noisier. This outcome is explainable by the reduced values of  $T_{abs}$  derivative when the sample has a temperature close to the ambient. The intrinsic noise of the thermocouple signal returns higher noise/signal ratios of the derivative when it approaches zero. To overcome this and obtain a one-to-one relation between  $\epsilon_{eff-TOT}$  and  $T_{abs}$ , a fitting of the data was performed in the range B\* – C by use of the second order polynomial function  $\epsilon_{eff-TOT-FIT}$ , see **Fig. 2.17(a)**.

In **Fig. 2.17(b)** are shown the fitted emittances  $\epsilon_{eff-TOT-FIT}$  resulting from tests #1 to #3 of the outdoor and #1 to #3 of the indoor measurement campaigns (coloured lines). They have good agreement each other and no trend can be extrapolated from comparing indoor versus outdoor results, neither from #1 and #2 versus #3 carried indoor, as they differ from usage of fan cooling. This implies that, even if the test facility has different external boundary conditions, the resulting  $\epsilon_{eff-TOT-FIT}$  is not sensibly affected. More experimental details about this boundary conditions will be reported following in **Tab. 2.3** and **Tab. 2.4**. The six  $\epsilon_{eff-TOT-FIT}$  results that appear in **Fig. 2.17(b)** group together in a variation of  $\pm 0.0025$  at  $T_{abs}$  above 150 °C, while  $\pm 0.0035$  below, corresponding roughly to  $\pm 2.5\%$  and  $\pm 4\%$  of the average, respectively. The increased variation at lower temperature leads to the higher noise of  $\epsilon_{eff-TOT}$  which presumably affects the result of the fit.

In **Fig. 2.17(b)** is reported also the total thermal emittance of the absorber as the sum of the emittances optically estimated  $\epsilon_{abs-OPT}$  and  $\epsilon_{sub-OPT}$  together with the corresponding effective total thermal emittance  $\epsilon_{eff-TOT-OPT}$  in hypothesis of infinite plates.  $\epsilon_{eff-TOT-OPT}$  is the sum of the two thermal emittances optically estimated, but each corrected through eq. 2.2, assumed that the coated side of the absorber exchanges radiation only with the glass, whose thermal emittance is set 0.85, and the uncoated side only with the stainless-steel of the vessel, with emittance 0.13. At temperatures below 150 °C there is accordance between the fitted  $\epsilon_{eff-TOT-FIT}$  of the six experiments and the sum of the two optical emittances  $\epsilon_{abs-OPT} + \epsilon_{sub-OPT}$ , but above with the increase of  $T_{abs}$ , the calorimetric results tend to be lower. At  $T_{abs} = 200$  °C, the sum  $\epsilon_{abs-OPT} + \epsilon_{sub-OPT}$  is on the edge of variation of the calorimetric values, and at  $T_{abs} = 300$  °C it overestimates the total emittance of 0.01, i.e., 9% of the calorimetric result. On the other hand, the optical total effective emittance  $\epsilon_{eff-TOT-OPT}$  underestimates the calorimetric outcome in the whole investigated temperature range. This discrepancy reduces with temperature, ranging from 11% at  $T_{abs} = 50$  °C to 8% at  $T_{abs} = 300$  °C.

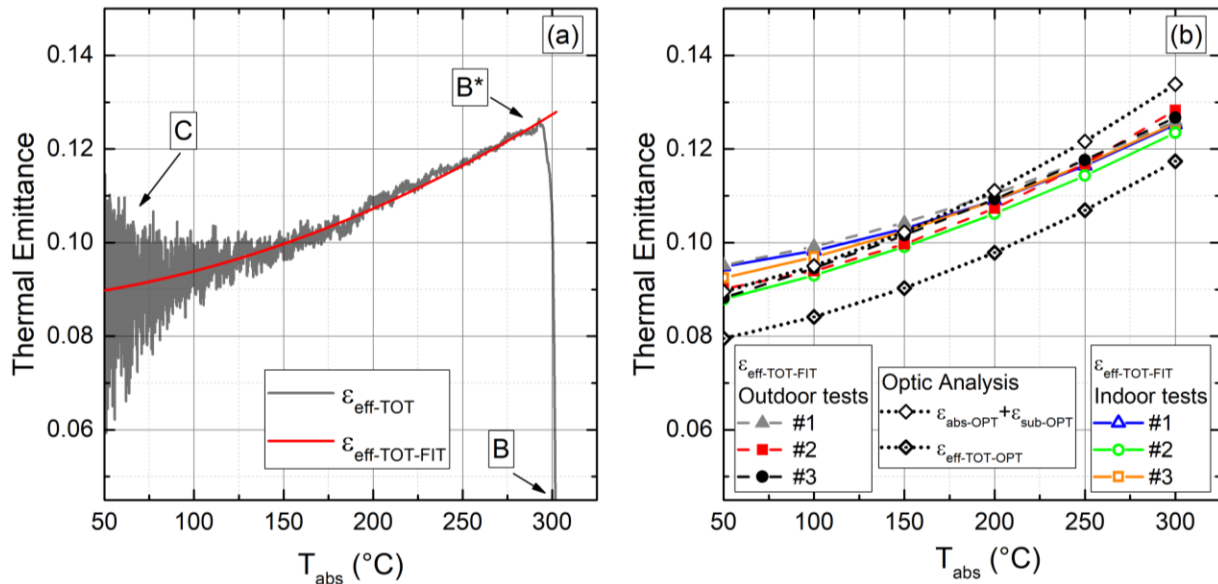


**Fig. 2.17** An example of calorimetrically measured effective thermal emittance  $\epsilon_{\text{eff-TOT}}$  is reported together with the polynomial fitting curve  $\epsilon_{\text{eff-TOT-FIT}}$  as function of  $T_{\text{abs}}$ . (b) Polynomial fitting curves are reported as function of  $T_{\text{abs}}$  for three indoor and three outdoor experiments together with the total thermal emittance derived by optic reflectivity measurements as sum of  $\epsilon_{\text{abs}}$  and  $\epsilon_{\text{sub}}$ , and as the effective emittance  $\epsilon_{\text{eff-TOT-OPT}}$  calculated by eq. 2.2.

These results underline the main scope of the presented calorimetric test facility. Neither the sum of the spectrally averaged emittances of the two sides carried out by optical analysis, nor the further correction by eq. 2.2 of infinite plates can be used to obtain an accurate estimation of the actual effective total thermal emittance of the absorber when working under operating conditions of evacuated flat panel. The reasons of such discrepancy might be the change of the spectral emissivity of the sample at high temperature and/or a not well-modelled radiative interaction with the surroundings.

The first effect was already experimentally observed in the past, as discussed previously in section 1.3. For instance, Echániz et al. carried out the optical analysis of a selective absorber, a multilayer coating based on Si, Mo and N over a substrate Ag coated, at actual temperatures as high as 600 °C using an innovative homemade IR-radiometer, rather than the traditional measurement performed at room condition. They observed a strong reduction, from 0.75 to 0.58, of spectral emissivity of the coated side at 2  $\mu\text{m}$  of wavelength when the absorber's temperature increases from 250 to 350 °C. A slight but uniform increase at longer wavelengths of the rest of the spectral emissivity returned an augmented spectrally averaged emittance of the order of 8% in the same range of temperature, but with an attenuated rate of increase because of the shift of emissivity at lower wavelengths. The authors attributed such a phenomenon to a change of the radiative properties of the selective coating and a similar effect might happen also during our calorimetric tests, being a potential explanation to the obtained experimental results.

The interaction with the surroundings might be an additional cause of the observed discrepancies, and 3D numerical simulations are needed to quantify its impact on the effective thermal emittance. To ease the reading, we anticipate here that numerical simulations reveal no impact of the geometry on the radiative exchange with the glass and vessel, confirming the

quality of the design of the facility, but more details about the numerical apparatus and the outcome of the simulations are discussed in the section 2.6.

The presented test facility and its measurement algorithm are more reliable than the traditional optic analysis performed at room temperature and its traditional mathematical correction. This is possible because during the calorimetric tests, the realistic operational conditions of the absorber are reproduced, and the measurement is focused directly on the radiative properties of interest.

Subsequently to the Cool-Down phase of each test, the Warm-Up phase is analysed to calculate  $\alpha_{\text{light}}$  as the only unknown of the calorimetric eq. 2.9, adopting as emittance parameter the fitted curve  $\varepsilon_{\text{eq,TOT-FIT}}$  of the same test. Using this approach, every test is stand-alone and not correlated to other parallel experiments. Similarly to  $\varepsilon_{\text{eff-TOT}}$ , also the calculated  $\alpha_{\text{light}}$  from the Warm-Up phase shows the anomaly due to the delayed response of  $T_{\text{abs}}$  derivative at the beginning of the phase. In the first moments of the phase,  $\alpha_{\text{light}}$  turns to be zero but increases to more realistic values when the  $T_{\text{abs}}$  derivative steps over the point  $A^*$ . The interval  $A - A^*$  impacts the measurement for no more than 20 °C and  $\alpha_{\text{light}}$  is calculated only in the following interval  $A^* - B^{\text{stag}}$ . For each indoor and outdoor test, the measured  $\alpha_{\text{light}}$  in  $A^* - B^{\text{stag}}$  can be assumed constant within a variation of  $\pm 1.5\%$  around the mean value.  $\alpha_{\text{Sun}}$  and  $\alpha_{\text{LED}}$  resulting from the outdoor and indoor experimental campaigns are reported in the following **Tab. 2.3** and **Tab. 2.4**, respectively.

**Tab. 2.3** summarizes the six experimental outdoor tests with  $P_{\text{Sun}}$  expressed in  $\text{Wm}^{-2}$  at  $A^*$  and  $B^{\text{stag}}$ , i.e., at the beginning and end of the interval to calculate  $\alpha_{\text{Sun}}$ . The temperatures measured in  $B^{\text{stag}}$  of absorber, glass, and vessel, in the order  $T_{\text{stag}}$ ,  $T_{\text{gla}}$  and  $T_{\text{ves}}$  are expressed in °C. The last column shows the mean value of the calculated  $\alpha_{\text{Sun}}$  in the interval  $A^* - B^{\text{stag}}$  together with  $\alpha_{\text{Sun-OPT}}$  from the optical analysis which is reported in the bottom row. The measured  $P_{\text{Sun}}$  values are as high as  $0.9 \text{ kWm}^{-2}$  because all the six tests were conducted on clear sky days in Naples,  $40^\circ 51' \text{ N} - 14^\circ 18' \text{ E}$ , in October and around noon. The chamber was exposed to the solar radiation and ambient air with no fan system to force the external convection. There is accordance between the six calorimetric  $\alpha_{\text{Sun}}$  and optical  $\alpha_{\text{Sun-OPT}}$  with a maximum discrepancy of 0.024 corresponding to 2.5% of  $\alpha_{\text{Sun-OPT}}$ .

**Tab. 2.3** The summary of six outdoor calorimetric experiments is reported. The table shows  $P_{\text{Sun}}$  measured at start and end of the Warm-Up phase on points  $A^*$  and  $B^{\text{stag}}$ , the temperatures at stagnation of absorber, glass, and vessel,  $T_{\text{stag}}$ ,  $T_{\text{gla}}$  and  $T_{\text{ves}}$ , respectively.  $\alpha_{\text{Sun-OPT}}$  and  $\alpha_{\text{Sun}}$  for each test are reported.  $\alpha_{\text{Sun}}$  is the averaged value calculated in  $A^* - B^{\text{stag}}$ .

Outdoor test	$P_{\text{Sun}}$ in $A^*$ ( $\text{Wm}^{-2}$ )	$P_{\text{Sun}}$ in $B^{\text{stag}}$ ( $\text{Wm}^{-2}$ )	$T_{\text{stag}}$ (°C)	$T_{\text{gla}}$ in $B^{\text{stag}}$ (°C)	$T_{\text{ves}}$ in $B^{\text{stag}}$ (°C)	$\alpha_{\text{Sun}}$
#1 (no ext. fan cooling)	910	921	308	56	59	0.930
#2 (no ext. fan cooling)	910	885	302	54	59	0.915
#3 (no ext. fan cooling)	906	897	305	50	58	0.910
#4 (no ext. fan cooling)	923	942	306	56	60	0.915
#5 (no ext. fan cooling)	915	926	311	50	59	0.932
#6 (no ext. fan cooling)	923	943	313	51	60	0.909

$$\alpha_{\text{Sun-OPT}} = 0.933$$

**Tab. 2.4** is analogous to **Tab. 2.3** but refers to the six tests carried indoor with the LED system. For this reason,  $P_{\text{LED}}$  is identified by one single value, constant all over the Warm-Up

phase, whereas the solar irradiance was intrinsically transient. Each  $P_{LED}$  is coupled to a Control Voltage that is the electric potential driving the control electronics of the LED system, ranging from 2 to 10 V [56]. Indoor tests #1 and #2 have glass and vessel temperatures sensibly lower than #3 because of the presence of the fan to externally cool the chamber. Although the difference is roughly 20 °C, the resulting  $\alpha_{LED}$  has no significant change, meaning that the calorimetric eq. 2.9 is reliable to describe the thermal behaviour of the absorber. Indoor tests #4, #5 and #6 were performed at lower  $P_{LED}$  obtaining lower  $T_{stag}$ , shifting from roughly 320 °C at 1 kWm<sup>-2</sup> to 226 °C at 0.4 kWm<sup>-2</sup>. Neither in this case significant variations on  $\alpha_{LED}$  can be detected. Calorimetric  $\alpha_{LED}$  obtained under different boundary conditions are in good accordance with the optical  $\alpha_{LED-OPT}$  having a maximum deviation of 2%, slightly lower than the discrepancy between  $\alpha_{Sun}$  and  $\alpha_{Sun-OPT}$ . This might be addressed to the higher time stability of the incident light provided by the LED system than the exposure to transient solar irradiance.

The good agreement between calorimetric and optic light absorptance validates two aspects simultaneously. One is how we modelled thermal losses, the other is how we modelled the light absorption mechanism.

**Tab. 2.4** The summary of six indoor calorimetric experiments is reported. The table shows the Control Voltage of the LED system and the corresponding  $P_{LED}$ , the temperatures at stagnation of absorber, glass, and vessel,  $T_{stag}$ ,  $T_{gla}$  and  $T_{ves}$ , respectively.  $\alpha_{LED-OPT}$  and  $\alpha_{LED}$  for each test are reported.  $\alpha_{LED}$  is the averaged value calculated in  $A^* - B^{stag}$ .

Indoor test	Control Voltage (V)	$P_{LED}$ (Wm <sup>-2</sup> )	$T_{stag}$ (°C)	$T_{gla}$ in $B^{stag}$ (°C)	$T_{ves}$ in $B^{stag}$ (°C)	$\alpha_{LED}$
#1 (with ext. fan cooling)	6.50	1060	330	49	48	0.944
#2 (with ext. fan cooling)	5.80	981	319	46	38	0.928
#3 (no ext. fan cooling)	5.57	951	320	70	55	0.929
#4 (no ext. fan cooling)	4.00	715	289	66	58	0.949
#5 (no ext. fan cooling)	3.00	552	263	60	53	0.946
#6 (no ext. fan cooling)	2.00	392	226	49	44	0.940

$$\alpha_{LED-OPT} = 0.947$$

## 2.6. Numerical 3D Thermal Simulations

The numerical 3D simulation of the whole facility, absorber and surrounding chamber, is a useful instrument to quantitatively realize the impact of each parameter and to validate the comprehension of all the thermal phenomena observed during the calorimetric tests. The model adopted to perform numerical 3D simulations was built using Comsol Multiphysics and is depicted in **Fig. 2.18**. The model was aimed at simulating both transient and steady-state temperature domain of the system in its indoor configuration, aiming at reproducing the calorimetric experimental data of the absorber using as input its optical absorptance  $\alpha_{LED-OPT}$ , and temperature dependent emittances  $\epsilon_{abs-OPT}(T_{abs})$  and  $\epsilon_{sub-OPT}(T_{abs})$  from the optical analysis.

Unfortunately, the computational complexity of radiation is exponential with the number of cells, so particular attention was paid in creating a numerical model as minimal as possible.

Instead of the original 3D CAD of the system, a simplified version was used to better matches the requirements of the simulation. The chamber walls were modelled as straight walls without holes to connect the turbopump, thermocouple feedthrough or pressure gauge. Such walls are in direct contact with the glass without the presence of any vacuum gasket. The absorber is a flat aluminium foil, and its stainless-steel thermocouple is modelled just as two cubic blocks placed respectively on the two sides of the absorber, emulating the actual thermocouple M3 fastening, the nut and the screw. The absorber is heated by a superficial power density term expressed as the product  $P_{LED} \times \alpha_{LED-OPT} \times \tau_{gla}$  which is assumed constant over time. The front and the back of the absorber can exchange thermal power with the thermocouple through the surface contact, and radiatively with the internal walls of the envelope, the glass and the stainless-steel vessel. The chamber walls are externally cooled by convection of air, natural or forced depending on the type of test we want to simulate. The internal residual gas and the four supporting springs are not simulated since their contribution is negligible as discussed previously in section 1.1 and 2.3. To speed up the computational time, the model is simulated only for its quarter, taking advantage of the intrinsic symmetry of the system. It is worth noticing that the size of the cells of the absorber have progressive reduction going from the edge to the centre. This choice leads to the expected temperature gradient on the absorber, which is bigger close to the thermocouple, see **Fig. 2.18**.

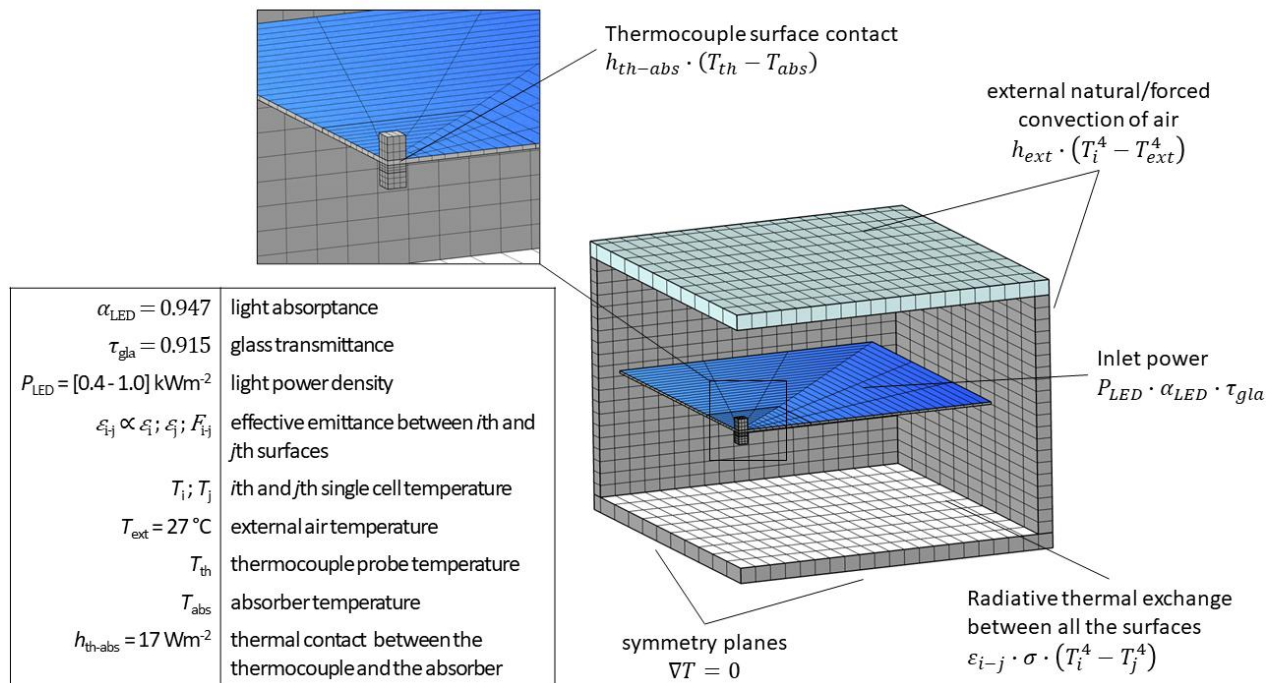


**Fig. 2.18** A quarter of the calorimetric test facility is modelled to perform thermal transient and steady-state simulations with Comsol Multiphysics. The choice of a simplified geometry and regular mesh was to minimize the computational complexity. The simulated boundary conditions are reported, and the table contains the description of each parameter.

**Fig. 2.19(a)** is the temperature map of the simulated absorber and thermocouple fastening after 20 s of maximum LED irradiation when the initial temperature of the absorber is 27 °C. It is possible to distinguish two slightly different temperatures  $T_{th}$  and  $T_{abs}$ , the first is the simulated mean temperature of the thermocouple bolt, the second is the simulated

temperature of the absorber far from the bolt and not affected by its presence. In **Fig. 2.19(b)**, the simulated time derivative of  $T_{th}$  and  $T_{abs}$  are compared to that experimentally measured in the same boundary conditions (initial temperature = 27 °C and  $P_{LED} = 1360 \text{ Wm}^{-2}$ ).  $T_{abs}$  derivative is maximum at relative time 0 s, as even expected by the calorimetric eq. 2.9 since the lower  $T_{abs}$ , the lower the emitted radiation ( $\propto T_{abs}^4$ ), the higher the temperature derivative for a fixed absorbed power. On the contrary, the simulated  $T_{th}$  evolves gradually from the zero of derivative to its maximum which is reached after 20 s of the heating process. This is easily explained by the thermal interaction between the bolt and the absorber, as the bolt need a temperature gradient to increase its temperature. The fact that the simulated  $T_{th}$  and  $T_{abs}$  derivatives meet at 20 s of the heating process means that the established gradient between the bolt and the absorber is constant in time with no impact on the simulated derivatives. These results are validated by the experimental temperature derivative during the calorimetric test under the same boundary conditions, see **Fig. 2.19(b)**, since the simulated  $T_{th}$  derivative is in perfect agreement with the experimental measurement. The presence of the bolt affects inevitably the temperature measurement, making very difficult the experimental observation of the immediate thermocouple response as seen with the simulation.

This simulative-experimental comparison of **Fig. 2.19** is referred to a very extreme condition of  $P_{LED} = 1360 \text{ Wm}^{-2}$ , that is the maximum reachable with the adopted solar simulator. The choice of such a power intensity led to the chance of maximizing the temperature derivative, both experimental and simulated, to enhance the impact of the fastening.

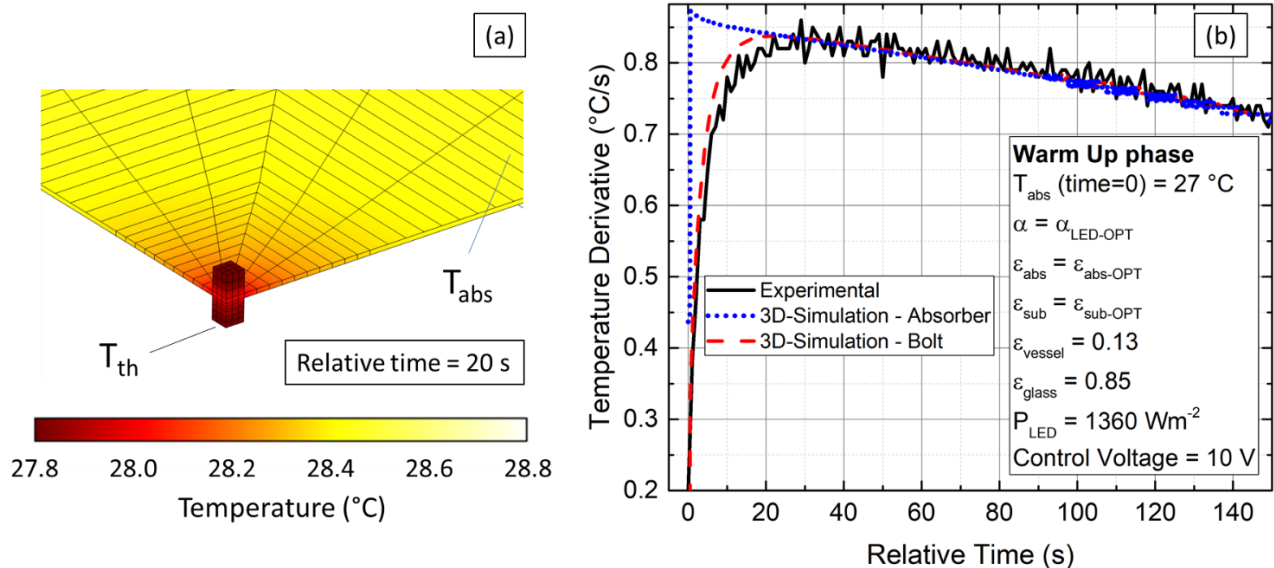


**Fig. 2.19** The result of time dependent simulations confirms the role of the bolt observed from the experimentally measured absorber's temperature derivative. (a) The temperature domain as result of the transient simulation is shown at the relative time = 20 s. The gradient between the bolt and the absorber is of the order of 1 °C. (b) The simulated temperature derivative of the edge of the absorber, see  $T_{abs}$ , and that of the bolt,  $T_{th}$ , are compared to the experimental measurement. There is good accordance between the simulated derivative of  $T_{th}$  with the measured derivative, while the simulated absorber has its maximum temperature derivative exactly at the relative time = 0 s.

During each calorimetric test at the beginning of the Warm-Up phase, the temperature derivative of the absorber is dominated by the role of the absorbed light ( $P_{\text{light}} \times \alpha_{\text{light}} \times \tau_{\text{gla}}$ ), because the emitted radiative power is very low at temperature close to ambient. This means that the simulated  $T_{\text{th}}$  and the measured absorber temperature in the first moments of the test cannot be affected by an eventual inaccurate estimation of the thermal emittances. With the increase of  $T_{\text{abs}}$  during the Warm-Up phase, the role of thermal emittances increases its importance over the light absorptance, as also demonstrated by the weighting factor  $w$  described in section 1.2. Thanks to the 3D numerical simulation, the actual radiative interaction of the absorber with the surrounding can be extrapolated, getting a deeper comprehension of the phenomena occurring during the experimental tests.

In **Fig. 2.20**, the absorber stagnation temperatures measured experimentally during the same six indoor tests reported before are compared to those expected by the 3D simulation and by the calorimetric eq. 2.9 using as input the optically estimated emittances  $\varepsilon_{\text{abs-OPT}}$  and  $\varepsilon_{\text{sub-OPT}}$ . Thanks to the calorimetric eq. 2.9, the stagnation temperature can be calculated assuming as effective thermal emittance the sum of the optical emittances  $\varepsilon_{\text{abs-OPT}} + \varepsilon_{\text{sub-OPT}}$  or the correction of each with the model of infinite plates. Rewriting this equation for the specific case of stagnation, i.e., no temperature derivative of the absorber, we obtain the following eq. 2.10

$$T_{\text{stag}} = \sqrt[4]{\frac{P_{\text{light}} \tau_{\text{gla}} \alpha_{\text{light}}}{\sigma \varepsilon_{\text{eff-TOT}}} + T_{\text{amb}}^4} \quad 2.10$$

This equation cannot be written completely explicit for  $T_{\text{stag}}$  since  $\varepsilon_{\text{eff-TOT}}$  is dependent on the absorber temperature too, so an iterative algorithm was developed to calculate  $T_{\text{stag}}$ . What emerges from **Fig. 2.20** is that  $T_{\text{stag}}$  values calculated by the 3D simulation are in good agreement with those obtained by eq. 2.10 in case of  $\varepsilon_{\text{eff-TOT}} = \varepsilon_{\text{abs-OPT}} + \varepsilon_{\text{sub-OPT}}$  for all the investigated  $P_{\text{LED}}$  range 0.4 – 1.0 kWm<sup>-2</sup>. On the contrary, the case of the theoretical correction of infinite parallel plates  $\varepsilon_{\text{eff-TOT}} = \varepsilon_{\text{eff-TOT-OPT}}$  reveals higher  $T_{\text{stag}}$  than the 3D-simulation of 10 °C at  $P_{\text{LED}}$  of 0.4 kWm<sup>-2</sup>, up to 18 °C at 1.0 kWm<sup>-2</sup>. This means that, for the 3D-simulation, the radiative interaction of the absorber with the glass and vessel is of second order, and the radiative thermal exchange is only function of the absorber properties.

To ease the reading, in **Fig. 2.20** is also repropounded **Fig. 2.17(b)** that contains the effective thermal emittances measured during the Cool-Down phase of three outdoor and three indoor tests, compared to the expected values by the optical reflectivity measurement. In **Fig. 2.20**, the experimental  $T_{\text{stag}}$  values overlap those of the 3D-simulation at  $P_{\text{LED}} = 0.4$  kWm<sup>-2</sup>, confirming the fact that the experimental calorimetric emittance  $\varepsilon_{\text{eff-TOT}}$  agrees with the sum of the optical emittances  $\varepsilon_{\text{abs-OPT}} + \varepsilon_{\text{sub-OPT}}$  up to 200 °C. As  $P_{\text{LED}}$  increases, the experimental  $T_{\text{stag}}$  becomes bigger and reached a deviation of 10 °C at  $P_{\text{LED}} = 1.0$  kWm<sup>-2</sup> where the experimental stagnation temperature is 330 °C. For every stagnation condition, the correction of infinite parallel plate overestimates the experimental temperatures of roughly 10 °C.

These results are perfectly in line with the calorimetric emittance  $\varepsilon_{\text{eff-TOT}}$  measured during the Cool-Down phase, as it was lower than the sum of the optical emittances  $\varepsilon_{\text{abs-OPT}} + \varepsilon_{\text{sub-OPT}}$  and simultaneously higher than those obtained by the correction of the infinite parallel plates. In conclusion, these simulative results confirm the initial proposed interpretation of the behaviour of the thermal emittance with respect to the optical estimation at temperatures

above 200 °C, see **Fig. 2.17(b)**, as the change of the radiative properties of the coating is the only possible mechanism in action to justify those results.

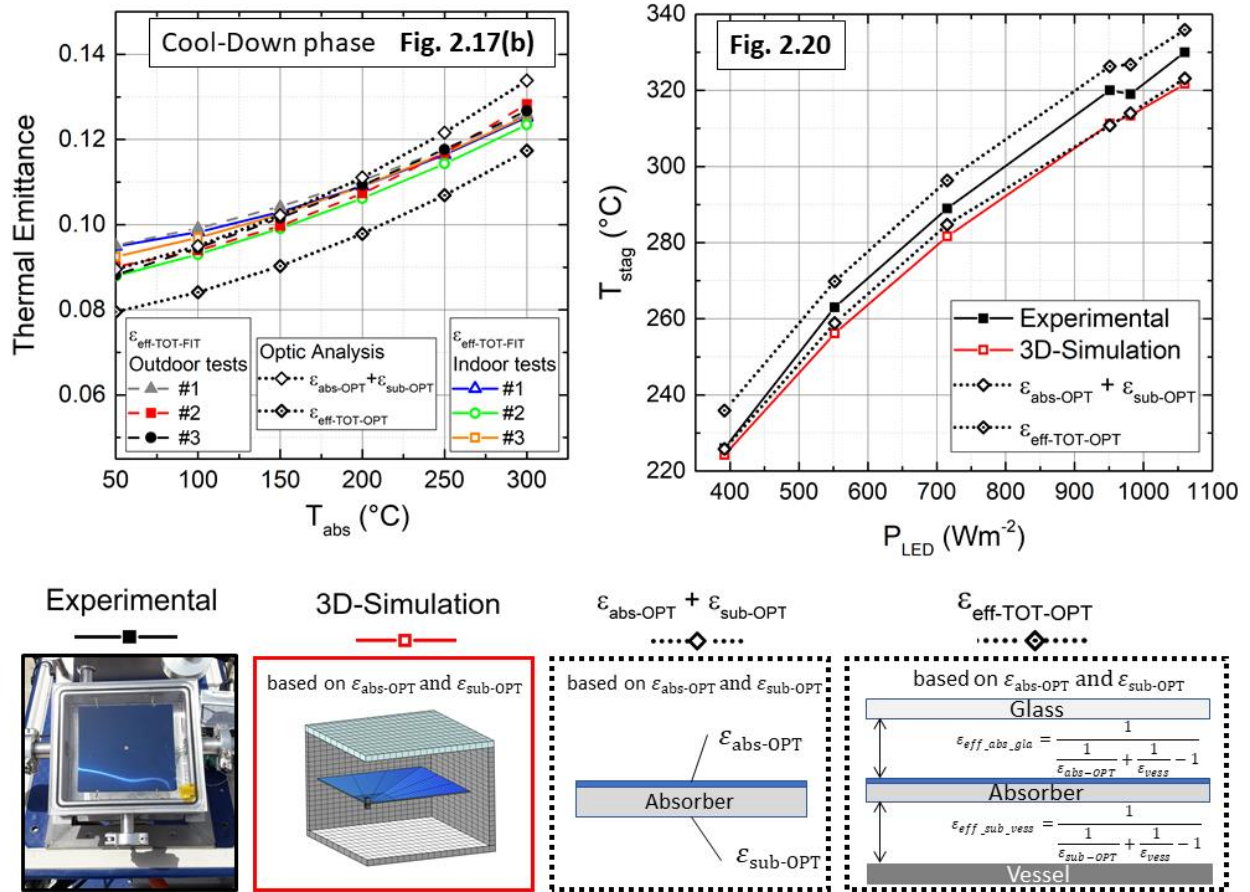


**Fig. 2.20** Absorber stagnation temperatures  $T_{\text{stag}}$  of the six indoor calorimetric tests are shown as function of the light power density  $P_{\text{LED}}$  and are compared to the stagnation temperatures expected by the 3D numerical simulation and by iteratively solving the eq. 2.10 adopting as emittance the sum of the optical emittances  $\epsilon_{\text{abs-OPT}} + \epsilon_{\text{sub-OPT}}$  and the effective emittance obtained by the model of infinite parallel plates  $\epsilon_{\text{eff-TOT-OPT}}$ . In this figure also **Fig. 2.17(b)** is repropose to ease the interpretation of the stagnation data.

### 3. Production of Novel Selective Solar Absorbers

Once the reliable characterization procedure had been developed to test absorbers under realistic operating conditions, the activity of production of novel absorbers took place. The previous paragraph 1.2 introduced the basic technologies to produce selective absorbers and anticipated that multilayer and cermet coatings with an extra antireflective layer are the most used solution at industrial scale for their simplicity, reliability, and performance. Even their combination is an effective solution consisting of a layered structure where each layer is cermet, and, among the layers, the volumetric density of the metallic particles into the dielectric matrix changes guaranteeing the alternation high-low metal fraction, similar to the metal/dielectric alternation of multilayers [58].

Our application of mid-temperature heat, above the threshold of 100 °C as operating temperature, requires an absorber with a new balance between solar absorptance and thermal emittance, as discussed in section 1.2. The weighting factor, relative importance of thermal emittance against absorptance, reaches values above 1 only for the specific case of the unconcentrated evacuate flat plate panel, and, for this reason, a new category of absorbers is emerging. This subject is completely new among the numerous works available in literature about absorbers for low- and high-temperature applications. Those two categories share values of weighting factor sensibly lower than 1 and particular attention was paid in maximizing solar absorptance, as reported by review articles about plate absorbers for low-[59] and concentrated tube receivers for high-temperature [23], [26]. As opposite, the role of absorber's thermal emittance is key for the conversion efficiency of the evacuated flat plate panel, and the proper design for the absorber is needed.

The aim of this work is not only producing prototypical flat absorber samples properly designed to be calorimetrically tested under realistic operating conditions, but also to make the proposed solution respect the requirements of the industrial production. The chosen architecture is the multi-layered Cr-based coating with SiO<sub>2</sub> on top as antireflecting layer deposited over a copper foil acting as substrate. The choice of copper over aluminium, which are the two traditional alternatives as substrate of plate absorbers, is due to its lower thermal emittance, 0.020 for copper and 0.045 for aluminium [60]. The chosen selective multilayer coating is Chromium based with the alternation of nanometric metal-dielectric phases obtained by deposition of the metal and its oxide. This solution was preferred to cermet layers since the deposition of the metallic phase into the dielectric matrix would have introduced additional deposition parameters, whereas simplicity and reproducibility is pursued.

#### 3.1. *Optics Fundamentals for the Multilayer Selective Coating*

The concept of operation of nanometric layers with metal/dielectric alternation has solid analytic foundations. The most general mathematical formulation to describe electromagnetic waves and their interaction with the matter is the Maxwell's set of differential equations of the electric and magnetic field. Under the hypotheses of electromagnetic wavelength sensibly bigger than the material' size in its direction of propagation and of uniform plane sinusoidal wave, the Maxwell's equations can be simplified as follows to describe the transmitted, reflected and absorbed light when interacting with the matter. Eq. 3.1 is the Snell's law of refraction and relates the angle of incidence of the light  $\theta_i$  to the transmission angle  $\theta_t$  when a

discontinuity of refractive index from  $n_1$  to  $n_2$  occurs. The reflection due to the same discontinuity can be modelled according to the Fresnel's laws, eq. 3.2, where the parallel and orthogonal component of the electromagnetic wave to the interface plane,  $R_s$  and  $R_p$  respectively, are function of the refractive indices  $n_1$  and  $n_2$ , the incident  $\theta_i$  and transmitted  $\theta_t$  angles. At each interface, the transmitted intensity is always complementary to the reflected amount, because of the basic energy balance equation. The absorption mechanism is modelled via the exponential decay of each ray intensity  $I$  through the medium from its initial value  $I_0$ , see eq. 3.3, where  $k$  is the extinction coefficient of the medium,  $\lambda$  is the electromagnetic wavelength and  $x$  is the spatial coordinate representing the depth reached by the wave.

$$n_1 \sin \theta_i = n_2 \sin \theta_t \quad 3.1$$

$$R_s = \left| \frac{n_1 \cos \theta_i - n_2 \cos \theta_t}{n_1 \cos \theta_i + n_2 \cos \theta_t} \right|^2; R_p = \left| \frac{n_1 \cos \theta_t - n_2 \cos \theta_i}{n_1 \cos \theta_t + n_2 \cos \theta_i} \right|^2 \quad 3.2$$

$$I = I_0 e^{-\left(\frac{4\pi k}{\lambda}\right)x} \quad 3.3$$

The conceptual scheme of the light interaction with a medium is reported in **Fig. 3.1**. Assumed three different materials A, B, and C interacting with an electromagnetic wave incident over the interface A-B, see **Fig. 3.1(a)**, the intensities and angles of the reflected and transmitted waves are governed by eq. 3.1 and 3.2. The first reflection keeps the wave inside the material A, while the transmitted goes across the material B and meets the second interface B-C. Being this another interface, the ray is partially transmitted and reflected again. The transmitted component continues forward the material C while the reflected continues within the material B. This component meets again the interface A-B, but now with inverted sequence of refractive indices. Theoretically, the endless repeat of such a process returns the total reflected and transmitted fractions of the incident electromagnetic wave as the sum of all the reflected components from the interface A-B and those transmitted from the interface B-C. The absorption mechanism is showed in **Fig. 3.1(b)** with the exponential reduction of the amplitude of the wave when going through the thickness of material B (assumed to have much higher extinction coefficient  $k$  than material A). The combination of the two described mechanisms, reflection-transmission and exponential absorption, are the basic strategies of the multilayer coating to absorb the incident light by increasing its path within the layers, taking advantage of absorbing materials with high extinction coefficient  $k$  to maximize the absorption and minimal discontinuity of refractive index  $n$  to reduce the total reflection.

Another mechanism that accounts for the light absorption is the destructive interference between the reflected and transmitted waves. It occurs independently from the exponential decay of the light intensity through the layers and can be obtained by using the proper combination of thicknesses. Typically, the dielectric layers follow the "quarter wavelength rule", as the destructive interference at a certain wavelength occurs when the thickness are a quarter of the incoming light. This, together with the characteristic solar wavelengths, explain why the whole structure of selective absorbing coatings are of the order of few hundreds of nanometres.

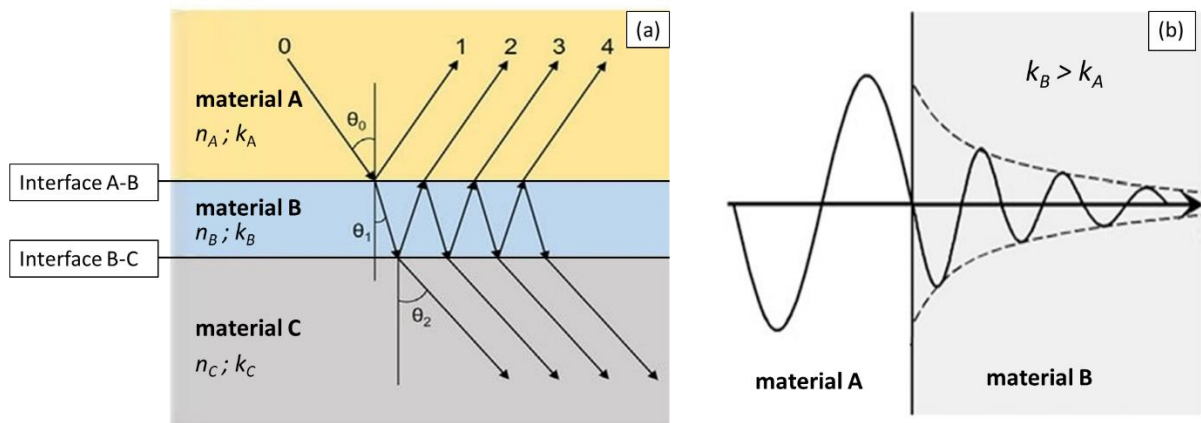


**Fig. 3.1** Conceptual scheme of light-matter interaction of a multi-layered coating. (a) The multiple reflections of the single ray incident over the interfaces A-B and B-C is the mechanism that regulates the net reflected and transmitted light. (b) The absorption mechanism of the single ray is exponential with the thickness of the layer.

The mechanisms of intrinsic absorption of the layers, multiple reflections and destructive interference are the chance that the multilayer coating applied over the reflective substrate has for absorbing the incident solar radiation. At the longer wavelengths of the radiative emission, the interaction of the coating with the electromagnetic wave is different since the wavelength reaches value of the order of micrometres and all the absorptive mechanisms strictly depend on it. Indeed, the extinction coefficient reduces its impact exponentially with the wavelength  $\lambda$ , see eq. 3.3, and the destructive interferences happen at the nanoscale through the rule of the quarter. The inefficiency of the coating to absorb longer wavelength means that it is neither efficient to emit at the same wavelength because of the Kirchhoff's law, reaching the desired selectivity of the coating in terms of high absorption in the solar range and high transparency in the IR wavelengths to take advantage of the low emissive substrate.

The multilayer sequence made of metal/dielectric alternation is one of the most used among selective coatings for thermal applications. Metals have commonly higher values of refractive index  $n$  and extinction coefficient  $k$  than dielectrics. The role of metals is to enhance the absorptance through its  $k$  while dielectrics minimize the gap of the refractive indices between the metal and the air/vacuum environment. There are examples of alternating metal/dielectric absorbers described in literature and some of them [61]–[66] are reported in the following **Tab. 3.1**. The dielectric materials used are Chromium Oxide  $\text{Cr}_2\text{O}_3$ , Silicon Dioxide  $\text{SiO}_2$  and Aluminium Oxide  $\text{Al}_2\text{O}_3$ ; for the metal layer Chromium Cr, Titanium Ti, Platinum Pt and Tungsten W; while Copper, Aluminium, stainless-steel, Tungsten and Titanium as reflective substrate. It is interesting to note that dielectric layers are matched almost with any other metal layer and vice versa. The thicknesses of the dielectrics are of the order of tens of nanometre, whereas the central metal layer keeps around 10 nm. The most recent of the reported works, (Tian et. al (2021) [66]) has an extra dielectric of  $\text{SiO}_2$  on top of  $\text{Al}_2\text{O}_3$  acting as antireflecting layer. This nomenclature derives from the fact that  $\text{SiO}_2$  has a very low refractive index,  $n = 1.45$ , and it can be effectively used to minimize the gap between the air/vacuum and the  $\text{Al}_2\text{O}_3$  with  $n = 1$  and  $n = 1.70$ , respectively.

**Tab. 3.1** Multi-layered metal/dielectric selective coatings for solar thermal absorbers are reported from the literature. Each column refers to a published article, with authors and year of publication in the first row, materials and thicknesses in the central rows and the substrate material in the last.

Barshilia et al. (2008) [61]	Zhou et al. (2012) [62]	Lai and Li (2013) [63]	Dereshgi et al. (2017) [64]	Lai (2020) [65]	Tian et al. (2021) [66]
Cr <sub>2</sub> O <sub>3</sub> (28 nm)	SiO <sub>2</sub> (90 nm)	SiO <sub>2</sub> (90 nm)	Al <sub>2</sub> O <sub>3</sub> (80 nm)	Al <sub>2</sub> O <sub>3</sub> (71 nm)	SiO <sub>2</sub> (90 nm) Al <sub>2</sub> O <sub>3</sub> (71 nm)
Cr (13 nm)	Cr (10 nm)	Ti (7 nm)	Ti (10 nm)	Pt (7 nm)	W (10 nm)
Cr <sub>x</sub> O <sub>y</sub> (64 nm)	SiO <sub>2</sub> (80 nm)	SiO <sub>2</sub> (110 nm)	Al <sub>2</sub> O <sub>3</sub> (80 nm)	Al <sub>2</sub> O <sub>3</sub> (76 nm)	Al <sub>2</sub> O <sub>3</sub> (71 nm)
Cu substrate (> 150 nm)	Al substrate (> 150 nm)	Stainless Steel (> 150 nm)	W substrate (> 150 nm)	Ti substrate (> 150 nm)	W substrate (> 150 nm)

In these works, as common for this research field, the authors prepared their absorbers depositing the layers over perfectly flat and smooth substrates, such as glass, silicon wafer or polished-mirror-like stainless-steel. This particular attention to the smoothness of the substrate comes from the negative impact that it has on spectral emissivity [67]. In literature there is lack of a complete and reliable correlation between roughness and local emissivity of the surface material, and, for this reason, every work about absorbers tends to overcome this problem testing only perfectly smooth samples. Once they got the smooth support, they covered it with a film of the desired reflective metal, thick enough (> 150 nm) to have no transparency at all wavelengths, emulating the optical response of the smooth bare material. The size of those samples was small (< 50 mm) and suitable only for optical analysis of reflectivity. All the reported literature works obtained great performances with optical solar absorptance above 0.90 and contained thermal emittances, below 0.08 at 300 °C. The removal of the roughness, the lack of any information about the back of the substrate (which thermal emittance has a not negligible weight), and tests carried out only via reflectivity measurements make all those results not useful for our application.

Our work wants to fill all these gaps producing novel absorbers using as substrate the commercial bare copper foil, as it is without modifications, and then to qualify their performance through the novel calorimetric test facility, previously presented, reproducing the real operating condition of the absorber.

### 3.2. Proposed Architecture of the Multilayer Absorber

The chosen architecture for the proposed selective solar absorber consists of the alternation of Cr and Cr<sub>2</sub>O<sub>3</sub> over a copper commercial foil with an extra layer of SiO<sub>2</sub> acting as antireflective coating on top of the chromium-based multilayer. The scheme of the absorber is depicted in **Fig. 3.2**, where there are all the materials and layers involved.

Above the copper substrate there is a layer of Cu<sub>2</sub>O that is not result of any deposition, but natural oxidation of the metal exposed to air. Depending on the nature of the substrate,

temperature and time of exposure, its oxide layer could be more or less thick, and partially or fully oxidated. In case of copper, two are the possible oxides,  $\text{Cu}_2\text{O}$  cuprite and  $\text{CuO}$  tenorite. The full oxidation of the second can be achieved only at temperatures as high as  $300\text{ }^\circ\text{C}$ , whereas below  $200\text{ }^\circ\text{C}$  the first is more stable forming a layer of around  $10\text{ nm}$  [68], [69]. The introduction of the oxide layer over the metallic substrate is an aspect not usually considered when designing laboratory absorber samples, as they are prepared without the natural oxidation layer. As opposite, after the industrial lamination of copper (typically stored as ribbons) there could be a long-time interval before the deposition of the absorbing coating, causing the exposure to air and humidity. To reproduce realistic deposition conditions, the proposed coatings were deposited on the commercial copper foil as it arrived from the manufacturer without any pre-process to remove the oxide or to smooth the surface.

Another difference with the other works from literature is that the proposed multilayer, see **Fig. 3.2**, has the first deposited layer metallic instead of dielectric. The reason of this choice comes from the need for strong adhesion of the coating with the substrate, feature not mandatory during laboratory depositions over flat small samples, but of primary importance at industrial scale. The traditional industrial architecture for physical vapour deposition is roll-to-roll. The metallic substrate is a foil wrapped in ribbons and inserted within the deposition setup, unrolled, stretched, and moved to the various deposition sections of the system, then finally re-wrapped to be taken out. The substrate undergoes repeated bends and friction with the rolls, so it requires a strong adhesion of the coating otherwise the mechanical stresses would damage or even remove it during the deposition process itself. Typically, the bonding of the first dielectric layer with the substrate can be enhanced by an additional layer in between, as even reported by Almedco in the datasheet of their absorbers [24]. The candidate bonding materials are metals such as Niobium, Tungsten, Titanium or Chromium [70], [71] for their affinity with oxygen to create strong interatomic bonds. In our case the material chosen as bonding layer is Chromium.

Above the first Cr layer, the traditional three-layer sequence, dielectric-metal-dielectric, is obtained by  $\text{Cr}_2\text{O}_3 - \text{Cr} - \text{Cr}_2\text{O}_3$ , then finally coated by  $\text{SiO}_2$  as antireflecting layer.

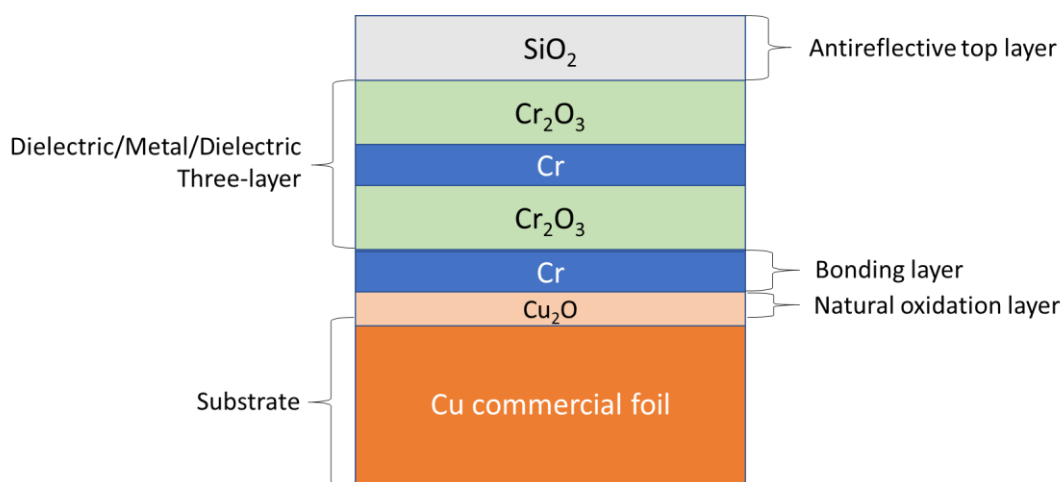


**Fig. 3.2** Structure of the proposed selective absorber. The substrate is a commercial copper foil with thickness  $0.20\text{ mm}$ , while the layers are nanometric (figure not in scale).

To better realize the role of each layer of the proposed structure, some values of refractive index and extinction coefficients from literature are reported in the following **Tab. 3.2**. There are the values of  $n$  and  $k$  of each material at two wavelengths,  $\lambda = 0.50 \mu\text{m}$  and  $\lambda = 2.0 \mu\text{m}$ , the first representative of the absorption mechanism in the solar range, the second of the IR interval for emission. The sequence Air/Vacuum – SiO<sub>2</sub> – Cr<sub>2</sub>O<sub>3</sub> – Cr – Cr<sub>2</sub>O<sub>3</sub> (following the path of the incident solar radiation) follows the gradient of refractive indices, as done so far in literature. The central Cr layer is demanded to absorb the light for its high values of  $k$ , two orders of magnitude higher than the other dielectrics of the stack, while the surrounding dielectrics are demanded to reduce the refractive index  $n$  discontinuity with the Air/Vacuum and the copper substrate. For instance, at  $\lambda = 0.50 \mu\text{m}$ , Cr has  $n = 2.55$  while Air/Vacuum 1.0 and Cu 1.16, so that the presence of the two Cr<sub>2</sub>O<sub>3</sub> layers and SiO<sub>2</sub> is needed minimize this discontinuity thanks to intermediate values of  $n$ , as 1.48 and 2.20 for SiO<sub>2</sub> and Cr<sub>2</sub>O<sub>3</sub> respectively. The inevitable presence of extra layers on bottom, Cr for bonding and Cu<sub>2</sub>O for natural oxidation of copper, spoils the optimal configuration “antireflective-dielectric-metal-dielectric-substrate”, affecting inevitably the performance. This is the explanation of why in literature absorbers are designed without the oxidation layer of the substrate and the metallic bonding film since in laboratory these constraints can be easily removed, contrarily to the industrial production.

**Tab. 3.2** Refractive indices and extinction coefficients from literature at two wavelengths ( $\lambda = 0.50 \mu\text{m}$  and  $\lambda = 2.0 \mu\text{m}$ ) of each material composing the layers of the proposed absorber.

Proposed Architecture	Material properties from literature	Refractive Index		Extinction coefficient	
		$\lambda = 0.50 \mu\text{m}$	$\lambda = 2.0 \mu\text{m}$	$\lambda = 0.50 \mu\text{m}$	$\lambda = 2.0 \mu\text{m}$
Air/Vacuum	Ciddor (1996) [72]	$n = 1.00$	$n = 1.00$	$k = 0.00$	$k = 0.00$
SiO <sub>2</sub>	Gao et al. (2012) [73]	$n = 1.48$	$n = 1.46$	$k = 0.00$	$k = 0.00$
Cr <sub>2</sub> O <sub>3</sub>	Al-Kuhaili et al. (2007) [74]	$n = 2.20$	$n = 1.90$	$k = 0.05$	$k = 0.02$
Cr	Rakic et al. (1998) [75]	$n = 2.55$	$n = 3.95$	$k = 4.11$	$k = 6.10$
Cr <sub>2</sub> O <sub>3</sub>	Al-Kuhaili et al. (2007) [74]	$n = 2.20$	$n = 1.90$	$k = 0.05$	$k = 0.02$
Cr	Rakic et al. (1998) [75]	$n = 2.55$	$n = 3.95$	$k = 4.11$	$k = 6.10$
Cu <sub>2</sub> O	Tahir et al. (2012) [76]	$n = 3.11$	$n = 2.38$	$k = 0.35$	$k = 0.03$
Cu	Ordal et al. (1985) [77]	$n = 1.16$	$n = 0.89$	$k = 2.64$	$k = 13.4$

In the next section 3.3, we report details about the deposition of all the layers of the proposed absorber; then in section 3.5, the experimental analysis of each layer of the coating is performed through the presented calorimetric test facility. Results will show the effectiveness of this proposed architecture in terms of performance, thermal stability, and easiness of production even at industrial scale.

### 3.3. Basics of Magnetron Sputtering

Physical Vapour Deposition (PVD) is the most common technique used to deposit thin films at industrial scale for selective solar absorbers over metallic substrates. Opposite to Chemical Deposition (CD) processes, where the layers are deposited through chemical reactions with the substrate, PVD consists of releasing vapours of the material to be deposited toward the substrate that is consequently coated by the condensed material.

The most relevant Physical Vapour Deposition techniques are Cathodic Arc, Electron-Beam, Thermal Evaporation, Pulsed Laser, and Magnetron Sputtering. In this work the adopted deposition technique is Magnetron Sputtering, as one of the most used for large scale production. In this paragraph its operating principle is described, and details of the laboratory scale deposition are reported. In the last chapter 4, the production at industrial scale is discussed by means of experimental tests with a roll-to-roll sputtering machine.

In **Fig. 3.3**, the conceptual scheme of operation of Magnetron Sputtering Deposition is shown. The deposition machine consists of a vacuum chamber kept under high vacuum by a pumping system. Within the chamber there is the substrate to be coated placed over a sample holder and the material to be deposited in shape of a bulk plate or disc, named "target", placed in front of the substrate. The back of the target, i.e., the side not exposed to the substrate, is cooled by water flux, attached to a magnet pack providing a magnetic field oriented mainly parallel, and connected to a power supply that keeps a negative potential. All the other components, such as the vacuum chamber and the sample, are electrically grounded. While the pump is active and the chamber has already reached its limit vacuum (base pressure of the order of  $10^{-7}$  mbar), Argon is injected with a controlled flux (commonly expressed in standard cubic meters - sccm) bringing the internal pressure up to  $10^{-3} - 10^{-2}$  mbar, depending on the required deposition conditions. The negative potential of the target, as high as hundreds of volts, ionizes the Ar atoms in  $\text{Ar}^+$  with the consequential release of electrons. The  $\text{Ar}^+$  ions are attracted by the negative potential of the target, acquiring a kinetic energy proportional to the applied voltage, and hit the exposed surface of the target. When the  $\text{Ar}^+$  ions have enough energy to break the interatomic bonds of the target material, its particles are released in the opposite direction of the Argon motion, in other words, towards the substrate obtaining the desired deposition of the target material. The kinetic energy of the  $\text{Ar}^+$  released to the target is also cause of undesired heating and must be dissipated. Usually the cooling system is water-based and operates on the back of the target support, being the other side exposed to vacuum.

During the sputtering process, close to the exposed surface of the target there is the presence of free electrons released by two different mechanisms. One is the ionization of Ar atoms, the other is the high energetic collision of the  $\text{Ar}^+$  ions to the target which causes the release of secondary electrons. Because of the negative potential of the target, every electron is repelled and pushed away towards the grounded surfaces of the chamber. Along their displacement such electrons interact with every Ar particle along their path enhancing the ionization process, and, to exploit this interaction, the permanence time of electrons is extended by means of a magnetic field forcing the electrons move along spirals instead of straight lines, Lorentz force  $F_{\text{Lorentz}}$  of eq. 3.4. This force gives to the electrons an additional component in the direction perpendicular to the velocity  $v$  and the magnetic field  $B$ , otherwise, without the presence of any magnetic field, the displacement would be straight due to the charge of the electron  $q_e$  interacting with the electrostatic field  $E_{\text{static}}$ .

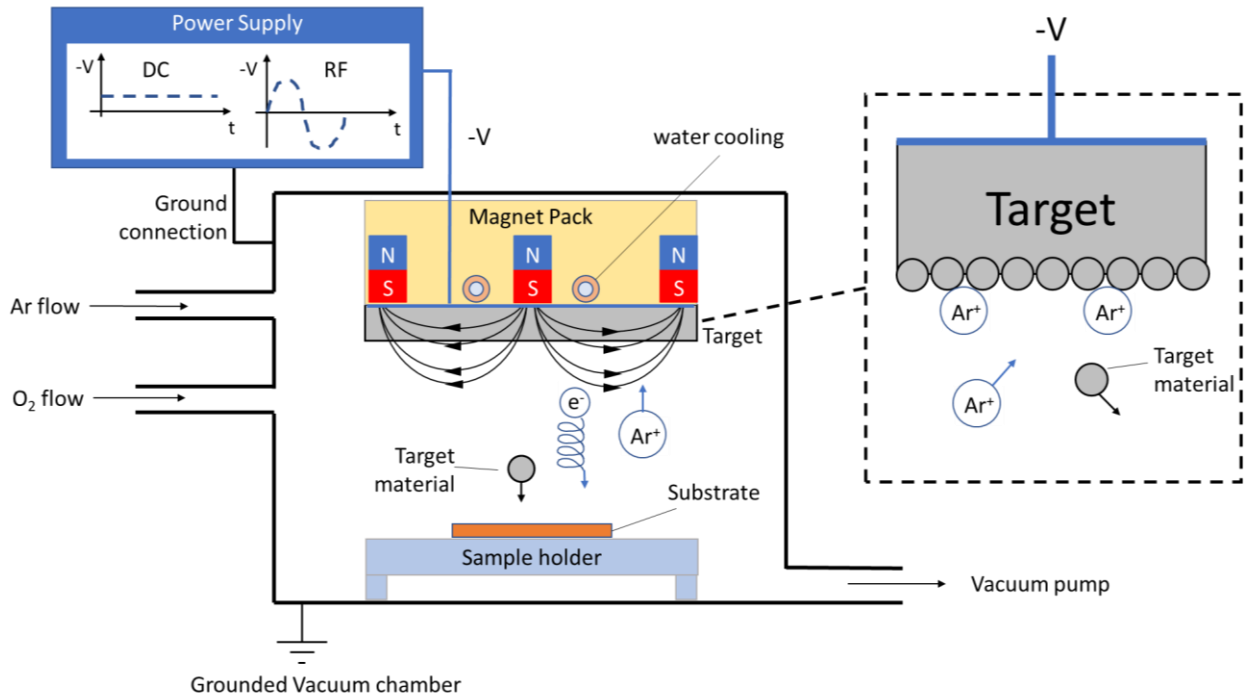


**Fig. 3.3** Conceptual scheme of operation of a Sputtering deposition machine. The sample is kept in place by a sample holder (electrically grounded), low-pressure is guaranteed by an active pumping system while Ar is injected together with O<sub>2</sub> or any other reactive gas. The target to be sputtered is charged with a negative potential thanks to a power supply, the Ar atoms tend to ionize and hit the target with a kinetic energy proportional to the applied voltage. The erosion release particles of the target material towards the sample to be coated.

It is worth noticing that, because of the right-hand rule for vector cross product of  $v$  and  $B$ , the increase of the permanence time comes from the component of the magnetic field parallel to the target surface.

$$\vec{F}_{Lorentz} = q_e(\vec{E}_{static} + \vec{v} \times \vec{B}) \quad 3.4$$

Depending on the type of target material to be deposited, and consequently on the kind of needed power supply, the sputtering process can be divided into two categories: Direct Current (DC) and Radio Frequency (RF) Sputtering. When the target is a metal, the negative potential of the power supply is completely transmitted to the exposed target surface due to the high electric conductivity, and the current of Ar<sup>+</sup> ions is continuous as long as the power supply provides constantly a negative potential of the order of 200-500 V. The use of a DC power supply to deposit metals gives the name to the process as Direct Current Sputtering. In case of a dielectric target material, the negative potential applied to the back of the target is weakly transmitted to the side to be sputtered, as dielectrics tend to polarize accumulating positive charges on the surface exposed to vacuum. This reduces the net potential and impacts on the ionization process of Argon. In addition, the already ionized Argon particles when hitting the target surface add their positive charge to the dielectric polarization, contributing to the decrease of the net superficial negative charge. These two mechanisms together affect

the continuity of the  $\text{Ar}^+$  current and brings the whole dynamic to cease. To completely overcome this issue, very high voltages would be needed, higher than 1 kV, letting the formation of plasma arcs all around the target and provoking damages of the experimental setup and hazardous for the safety of the operators. Instead of a continuous extreme high voltage for the dielectric target, the use of a transient voltage is effective to get rid of the charge compensation. The alternation of the applied voltage with a sinusoidal progression between a negative and positive potential with radio frequency can guarantee the desired continuity of deposition (RF Sputtering Deposition). When the applied potential is negative the  $\text{Ar}^+$  ions move towards the target, when positive the  $\text{Ar}^+$  accumulated on the exposed surface are repelled and move away. RF Sputtering (traditionally with a frequency of 13.56 MHz) has some disadvantages with respect to DC, since RF power generators are more expensive, the deposition rate is almost an order of magnitude lower than DC and the whole deposition machine must guarantee the perfect insulation of the parasitic radio-waves emitted towards the laboratory room.

In some cases, for example when the dielectric is the oxide of a metal, the alternative to RF is DC sputtering of the metallic target while injecting  $\text{O}_2$  into the chamber to chemically react with the sputtered metal. The partial pressure of Oxygen in the Argon atmosphere impacts on the  $\text{Ar}^+$  dynamic, changing the original deposition conditions of the metal and requiring higher voltages to sustain the  $\text{Ar}^+$  current. This technique is named DC Reactive Magnetron Sputtering [78], and particular attention must be paid to the deposition conditions to guarantee a good reproducibility and stability of the process. Its equivalent in RF [79] does not suffer of those stability issues, thanks to the alternation of the potential in radiofrequency, being very common among laboratory and industrial sputtering machines. This is easily comprehensible by the fact that thanks to the use of one type of power supply it is possible to sputter any kind of target, dielectrics and metals eventually with reactive gases, at the expenses of energy efficiency, cost effectiveness and simplicity of the deposition machine. For the specific case of production of solar absorbers, the use of the RF technology is mandatory because of some materials of interest, such as  $\text{SiO}_2$  that would need the Si target for the reactive DC process, that is not metallic. So that, deposition machines for industrial production of solar absorbers are likely to be equipped with RF power suppliers.

In the following paragraph 3.4, the experimental setup of the laboratory sputtering machine is described together with the deposition conditions of the materials of the proposed coating. The metallic Cr layers were obtained by DC sputtering of the Cr target, the  $\text{Cr}_2\text{O}_3$  layers from the same Cr target but in DC reactive sputtering with injection of  $\text{O}_2$  in chamber, the  $\text{SiO}_2$  by RF deposition from the target of  $\text{SiO}_2$ . In the final chapter 4 is shown that the same materials can be deposited steadily by a roll-to-roll machine. In addition, it will be demonstrated that there are conditions allowing the deposition of the  $\text{SiO}_2$  layer by DC reactive sputtering of the Si target with injection of  $\text{O}_2$ , obtaining that the whole multilayer coating can be deposited in DC mode and by use of just a Cr and Si targets, guaranteeing extreme simplicity of the design of the machine, cost effectiveness, and increased energy efficiency of the sputtering process.

### *3.4. Laboratory Sputtering Machine to Deposit the Proposed Coating Materials*

The laboratory sputtering machine used to deposit the proposed coating over commercial copper substrates is a batch device, meaning that both target and substrate positions are fixed

during the deposition. This architecture is very common among various research fields and allows to design space-saving machines, useful feature for any laboratory activity which operates with small-sized samples (below 50 mm). This is opposite to the roll-to-roll architecture of the industrial scale, where the substrate to be deposited moves continuously while the target is fixed, and the substrate is wrapped in ribbon with length of the order of kilometres and width of hundreds of centimetres.

In this section, we show the feasibility to deposit the materials with the batch-laboratory system, then in chapter 4, deposition tests are reported for the same materials also for an industrial real roll-to-roll machine. The goal is to demonstrate that the proposed coating solution is compatible with the requirements of the industrial scale.

The adopted laboratory machine is depicted in **Fig. 3.4**. Figure **(a)** is the external of the vacuum chamber. The central quartz window allows to see the plasma induced by the ionization of the gases during the process. **Fig. 3.4(b)** shows the internal of the chamber. There are four deposition sectors, each with a round target of 10 cm diameter facing a sample holder at roughly 10 cm, so it is possible to sputter four different targets over four different samples. The sample holders lean on a round plate that rotates moved by an electric motor and allows the positioning of the same holder below every of the four targets. **Fig. 3.4(c)** is the picture of the induced plasma close to the exposed target surface during a deposition. The concentric round shape derives from the design of the magnetic pack, which is made of permanent magnets fixed on the back of the target.

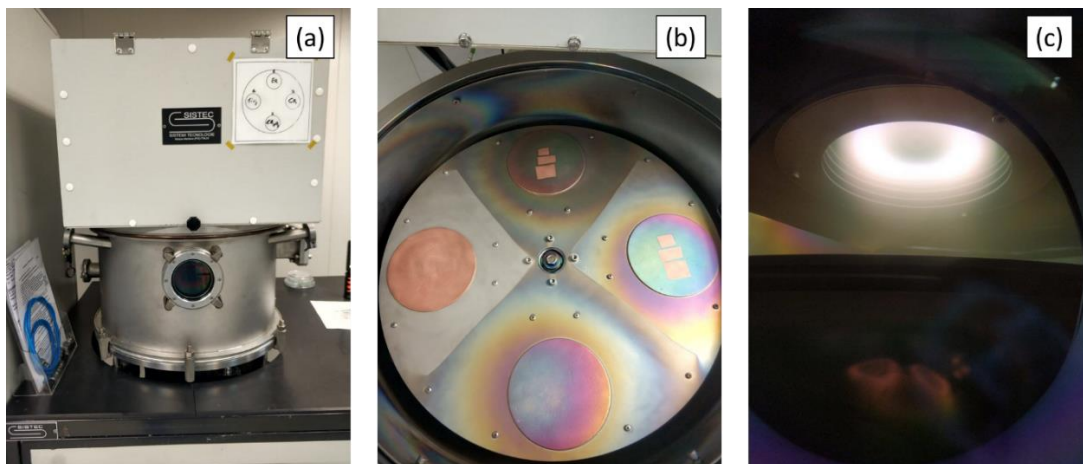


**Fig. 3.4** Pictures of the laboratory batch sputtering deposition machine. (a) The external of the vacuum chamber. (b) The plate supporting the four sample holders can rotate thanks to an electric motor. (c) Through a quartz window, the plasma induced by the ionization process is visible. Its shape is function of the magnetic field provided by permanent magnets on the back of the target.

The chamber is constantly evacuated by a pumping system composed of a rotary and a turbomolecular pumps connected in series. The second is exposed to the chamber, while the first collects the exhaust of the turbo and moves the pumped gas towards the ambient. The injection of gases into the chamber for the sputtering process brings the pressure from high vacuum levels, of the order of  $10^{-7}$ - $10^{-6}$  mbar, to medium vacuum up to  $10^{-3}$ - $10^{-2}$  mbar. In the

meanwhile, the turbopump is supposed to pump out these additional fluxes too with the risk of damage due to the relatively high pressure after hours of operation. To overcome this issue, the turbopump is connected to the chamber through a gate valve that reduces of half the pumped flux and, as consequence, the load on the turbopump when Ar and/or O<sub>2</sub> were injected for the sputtering depositions.

The deposition rate of each material at fixed deposition conditions was calculated through thickness measurement over the deposited material according to the following procedure. A smooth laboratory glass, cleaned with acetone, isopropyl alcohol, and then de-ionized water, was marked with a stripe of marker ink on the side to be coated. It was put on the sample holder facing the investigated target. After the deposition, the marked and unmarked points of the glass are equally coated. The glass is taken out from the machine and cleaned again with acetone and isopropyl alcohol. These solvents dissolve the ink of the marker and remove the coating from the points previously marked. The step height between the coated and uncoated glass is exactly the thickness of the deposited material, and it can be measured by means of profilometer measurements. The deposition rate of the process can be calculated easily as the ratio between the measured thickness and the deposition time. Carrying out this procedure for different positions over the holder, the spatial uniformity of deposition was estimated. Assumed acceptable a variation of 10% of the thickness, the maximum size of the square substrate to be deposited was 100 mm.

In the following **Tab. 3.3**, details of the sputtering process are reported for the deposited Cr, Cr<sub>2</sub>O<sub>3</sub> and SiO<sub>2</sub> by use of the laboratory batch setup. For every deposited material, the base pressure in the chamber before the injection of any process gas was  $4.0 \times 10^{-7}$  mbar. To reach such a value, the vacuum system needed at least 12 hours of continuous pumping of the chamber, so the pumps were activated the afternoon before the day of the deposition, taking advantage of the whole night for a full evacuation. The injection of Argon was set at 3.3 standard cubic meter (sccm) for the DC sputtering of Cr and Cr<sub>2</sub>O<sub>3</sub>, and 4.0 sccm for the RF sputtering, while the Oxygen flux was only for the DC reactive process to deposit Cr<sub>2</sub>O<sub>3</sub> from the Cr target. The two DC processes were controlled arbitrarily fixing the current sustained by the power supply, 0.30 A and 0.50 A for Cr and Cr<sub>2</sub>O<sub>3</sub> respectively, requiring a power of 89 W and 195 W. The Ar flux was chosen accordingly with the required voltage to sustain the processes. It was progressively increased starting from 0 sccm until the required voltage for a stable condition was below the threshold of 500 V. Indeed, as the partial pressure of Ar increases, the needed voltage to sustain a current reduces thanks to the augmented number of ionizable Ar atoms. The measured deposition rates of Cr and Cr<sub>2</sub>O<sub>3</sub> of 26 nm/min and 8.4 nm/min, respectively. Quite similar are the conditions of deposition of SiO<sub>2</sub> in RF sputtering, with Ar flow and pressure close to those in DC mode. The power supply was set to release a fixed power of 200 W returning a measured deposition rate was 6.6 nm/min, and no information about the voltage and current could be read from the RF controller. What emerges is that DC sputtering, in our case to deposit Cr, is more efficient than the other two processes in terms of needed power to guarantee a certain deposition rate. Indeed, Cr<sub>2</sub>O<sub>3</sub> in DC reactive sputtering has a deposition rate three times smaller when the demanded power is twice the Cr deposition. Even worse is the case of SiO<sub>2</sub> deposited in RF, since the obtained deposition rate is four times smaller for the same released power of 200 W.

**Tab. 3.3** Deposition details of the laboratory-batch sputtering process of each material of the proposed selective absorbing coating.

Material	Sputtering Mode	Ar flow (sccm)	O <sub>2</sub> flow (sccm)	Pressure (mbar)	Power (W)	Voltage (V)	Current (A)	Deposition Rate (nm/min)
Cr	DC	3.3	0.0	$2.2 \times 10^{-3}$	89	296	0.30	26
Cr <sub>2</sub> O <sub>3</sub>	DC Reactive	3.3	1.6	$3.1 \times 10^{-3}$	195	391	0.50	8.4
SiO <sub>2</sub>	RF 13.56 MHz	4.0	0.0	$2.5 \times 10^{-3}$	200	N.A.	N.A.	6.6

Base pressure =  $4.0 \times 10^{-7}$  mbar

The reported deposition conditions of Cr<sub>2</sub>O<sub>3</sub> derive from a pre-sputtering process which is needed to create the optimal deposition conditions for a stoichiometric oxide, since the right proportion of sputtered metallic Cr and injected O<sub>2</sub> must be found. In Fig. 3.5 the experimental characteristic oxidation curve of the Cr is reported. It consists of the required voltage to guarantee a constant current when the Ar flow is fixed for various O<sub>2</sub> flows. For a set current of 0.50 A and Argon flow of 3.3 sccm, the amount of Oxygen flow is progressively increased from zero up to 20 sccm, which is the limit of the adopted sputtering machine, then back to zero again. Each point of the figure is a stable deposition condition, kept for at least 2 minutes. The initial point A of the process has no O<sub>2</sub> flow and 330 V to sustain 0.50 A of current with the deposition of Cr in metal-mode. The injection up to 2.0 sccm of O<sub>2</sub> does not significantly change the needed voltage and the pressure keeps constant. This behaviour can be explained by the fact that the deposited Chromium chemically interact with all the injected Oxygen, forming the oxide, minimizing the Oxygen partial pressure in chamber. This amount of O<sub>2</sub> is so small that the Cr completely neutralizes its presence, explaining the minimal impact on voltage and pressure.

Increasing the O<sub>2</sub> flux to 3.0 sccm, the pressure is still the same while the needed voltage increases up to 360 V, point B. This is the result of the increased oxidation of Cr and of the interaction of O<sub>2</sub> with the cascade of free electrons. Increasing the O<sub>2</sub> flux above the point B, the pressure increases linearly with the O<sub>2</sub> flow, meaning that all the exposed Cr surfaces are fully oxidized and no pumping effect of O<sub>2</sub> can be observed. Any additional injection of Oxygen would directly increase the internal pressure of the chamber. In the point C, 4.5 sccm of O<sub>2</sub>, the voltage reaches a local maximum, since any further increase of injected Oxygen cannot affect the voltage up to 20 sccm of point D. In the interval C – D, there is the full oxidation of all the exposed Cr surfaces, even the target surface is fully oxidized, so that only Chromium Oxide is being deposited instead of the metallic Cr.

Reducing the amount of injected O<sub>2</sub>, the pressure and the voltage repeat backwards the same points observed before, down to 4.5 sccm where point E corresponds to the previous point C. Now, a further decrease of the O<sub>2</sub> flow would not return the same conditions of the first part of the process. Indeed, the voltage slightly increases as the O<sub>2</sub> flux reduces up to point F (1.6 sccm and 395 V), while the pressure follows its linear drop. This can be explained by the fact that at this point, because of the full oxidation of all the exposed Cr surfaces and with the target releasing Chromium Oxide, the reduction of the total pressure is responsible for the slight increase of the voltage. The further reduction of the O<sub>2</sub> flow, below 1.6 sccm, provokes a fast drop of the voltage being the injected Oxygen not enough to oxidate all the

sputtered Cr of the target. Stopping the O<sub>2</sub> flux, 0 sccm, the voltage returns to a value close to the initial.

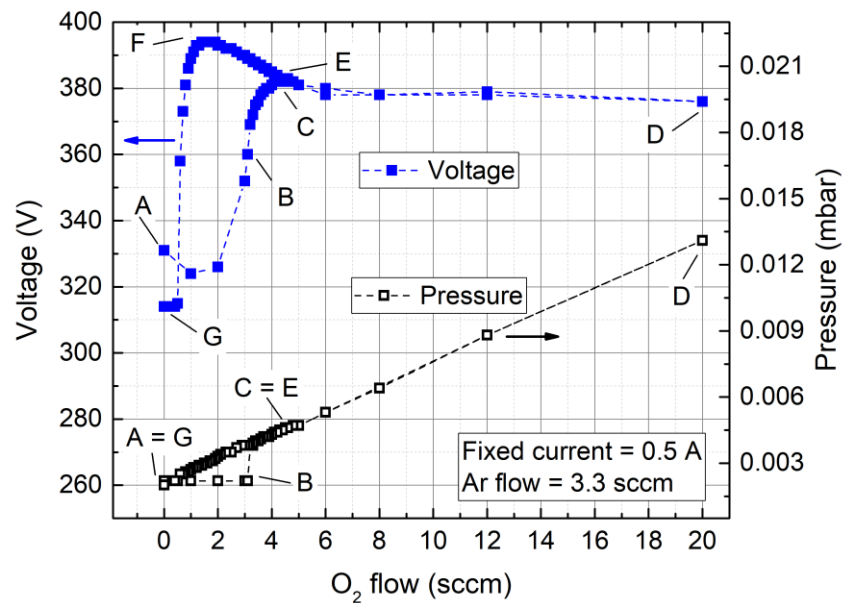


**Fig. 3.5** Oxidation hysteresis of Chromium during the DC reactive sputtering when the process current is fixed at 0.5 A and Ar flow is 3.3 sccm. The needed voltage, left axis, and the pressure, right axis, are reported as function of the injected O<sub>2</sub> flow.

The characteristic oxidation curve of a sputtered metal is well-known in literature. The width of the hysteresis, in terms of reactive flow, can be analytically modelled thanks to a 0-D approach [80]. What is of our interest is the stoichiometry of the deposited Chromium Oxide, and, fortunately, Contoux et al. in 1997 experimentally assessed that the best condition to deposit stoichiometric Cr<sub>2</sub>O<sub>3</sub> with DC reactive sputtering is the point of maximum voltage observed when reducing the injected O<sub>2</sub> after the full oxidation [81]. For this reason, our deposition condition of the reactive Cr<sub>2</sub>O<sub>3</sub> corresponds to point F of **Fig. 3.5**, previously reported in **Tab. 3.3**.

The preparation procedure to deposit Cr<sub>2</sub>O<sub>3</sub> consisted of injecting the O<sub>2</sub> flow at its maximum value of 20 sccm for at least 2 minutes while the target is being continuously sputtered. Then, the Oxygen flux was reduced progressively down to 1.6 sccm in 10 minutes. During this preparation phase, the sample holder underneath the target was left empty, with no substrate, and was coated by the mixture of Cr<sub>x</sub>O<sub>y</sub> and by Cr<sub>2</sub>O<sub>3</sub> only when the O<sub>2</sub> flux was set at the optimum value of 1.6 sccm. Thanks to the controlled rotation of the plate hosting the holders, the preparation phase was performed always over the same empty holder, then the actual deposition of Cr<sub>2</sub>O<sub>3</sub> was carried on the substrates put on the other three holders. For sake of reproducibility, also the other two materials Cr and SiO<sub>2</sub> had the pre-sputtering of 10 minutes over the same void holder, before the actual layer deposition

### 3.5. Deposition and Testing of the Proposed Absorbers

The adopted substrates to be coated by the proposed multilayer coating were commercial copper foils from KME [82] (thickness of 0.2 mm, width of 1 m and length of several meters wrapped in a ribbon). Three 100 mm × 100 mm square pieces were cut from the foils as arrived. Such a size was the limit due to the maximum acceptable deposition uniformity that was arbitrarily set to 10%. The three substrates were placed over the sample holders and fixed in place by stainless-steel frames, see **Fig. 3.6(a)**. Those frames were designed just for this peculiar application, since in laboratory it is not common to manage samples as large as ours. They were needed to mechanically keep the substrates in place, perfectly flat, and adherent to the holders during the process, otherwise the edge of the back would have been fouled by undesired deposited material. As explained before, each target was pre-sputtered over the empty holder before the actual deposition of the layer. When this preparation phase ended, the plate was rotated until the desired substrate was underneath the target in use and stayed in place to let the layer grow over the substrate. The thickness of the layer was controlled by the deposition time since the deposition rate had been previously calculated.

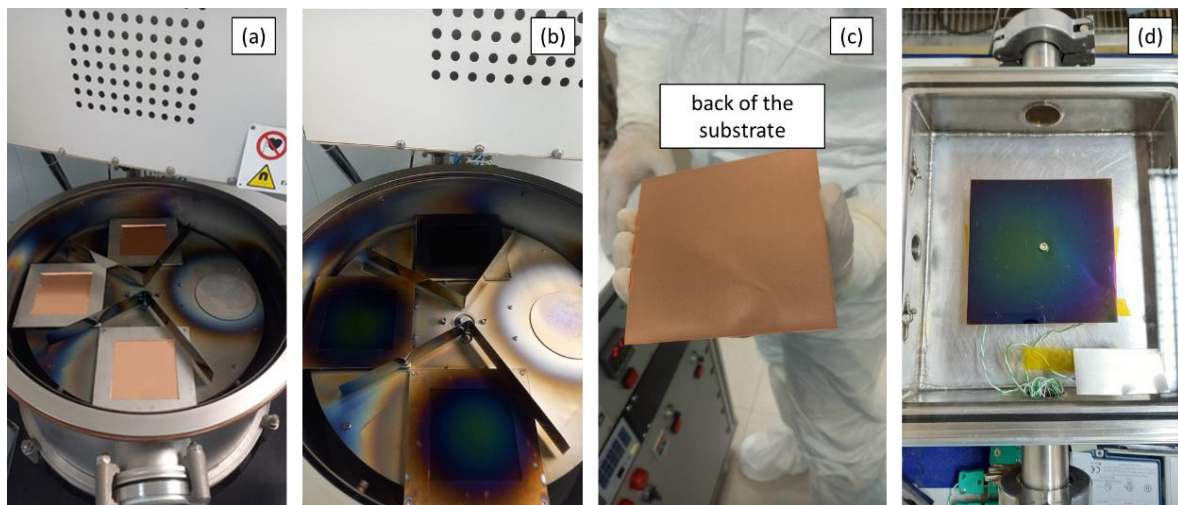


**Fig. 3.6** Pictures of production and calorimetric testing of the three proposed absorbers. (a) Positioning of the three copper substrates into the deposition machine before the process. (b) The result of the deposition process. (c) The back of the substrate after the deposition is uncoated thanks to the stainless-steel frames placed around the sample holder. (d) Positioning of one of the proposed samples into the calorimetric test facility. Because of the reduced dimensions of the absorber, 100 mm × 100 mm, it is supported by four stainless-steel pins attached to the bottom of the vessel keeping the same vertical coordinate of full-sized absorber.

In this work we produced three absorbers designed to work at three different temperature ranges: absorber #1 for temperatures below 100 °C, absorber #2 up to 200 °C, and absorber #3 for temperatures above 200 °C. They were based on the same multilayer structure but with different combinations of thicknesses, reported in **Tab. 3.4**. It is possible to note that all the thicknesses reduce from the absorber #1 to #3. The role of the absorbing coating is to enhance the solar absorption of the reflective substrate, contextually it increases the thermal emittance

of the coated side, so that the best trade-off must be found for each operating temperature. The three proposed absorbers have thicknesses comparable to the multi-layered absorbers seen in literature, previous **Tab. 3.1**. Here we want to demonstrate that a slight reduction of each thickness can strongly reduce the thermal emittance at the expense of a contained decrease of solar absorption, reaching a better compromise for the mid-temperatures. The result of the deposited materials is depicted in **Fig. 3.6(b)**. The supporting frames were coated together with the copper foils, while the back of each was perfectly protected, see **Fig. 3.6(c)**.

**Tab. 3.4** Thicknesses of each deposited material is shown for the three different proposed absorbers. From type #1 to #3 each layer had a reduction of the thickness to better match the requirement for a controlled thermal emittance at each operating temperature.

Deposited Material layers	Deposited Thicknesses (nm)		
	Absorber #1	Absorber #2	Absorber #3
SiO <sub>2</sub>	76	72	65
Cr <sub>2</sub> O <sub>3</sub>	68	52	45
Cr	10	9	8
Cr <sub>2</sub> O <sub>3</sub>	54	27	14
Cr	41	17	10

The three absorber samples were calorimetrically tested indoor. The reduced size of those samples needed a different mechanical support to keep in place the absorbers during the test, because the distance from the lateral walls of the chamber was too large for the stainless-steel springs, see **Fig. 3.6(d)**. The adopted solution was to fix four stainless-steel pins on the bottom of the vessel and leaning the absorber on the sharpened tips to minimize the surfaces of contact. The reduced size of the sample, 100 mm x 100 mm, and the different supporting structure could affect the reliability of the calorimetric testing. The calorimetric equation 2.9 was built on some assumptions and validated for the full-sized absorber 140 mm x 150 mm. Thermal conduction of the structure and the presence of the bolt in the centre of the absorber could be no longer negligible, requiring additional terms of thermal loss into the calorimetric equation. For sake of simplicity, the calorimetric equation was not adjusted and was used exactly like it had been done to test the Mirotherm<sup>®</sup> absorber. The calorimetrically measured effective total thermal emittance would be increased by those additional sources of loss making the results of the three novel proposed absorbers surely conservative in terms of converted solar energy.

Together with the calorimetric testing, also the optical analysis was carried out by means of reflectivity measurements at room temperature, obtaining as outcome the spectral emissivity curve  $\epsilon_\lambda$ . A full-sized 140 mm x 150 mm bare uncoated copper was experimentally investigated too, both optically and calorimetrically, to better realize the improvement in performance reached by the presence of the coatings. Results of optical and calorimetric measurements are reported in **Fig. 3.7**.

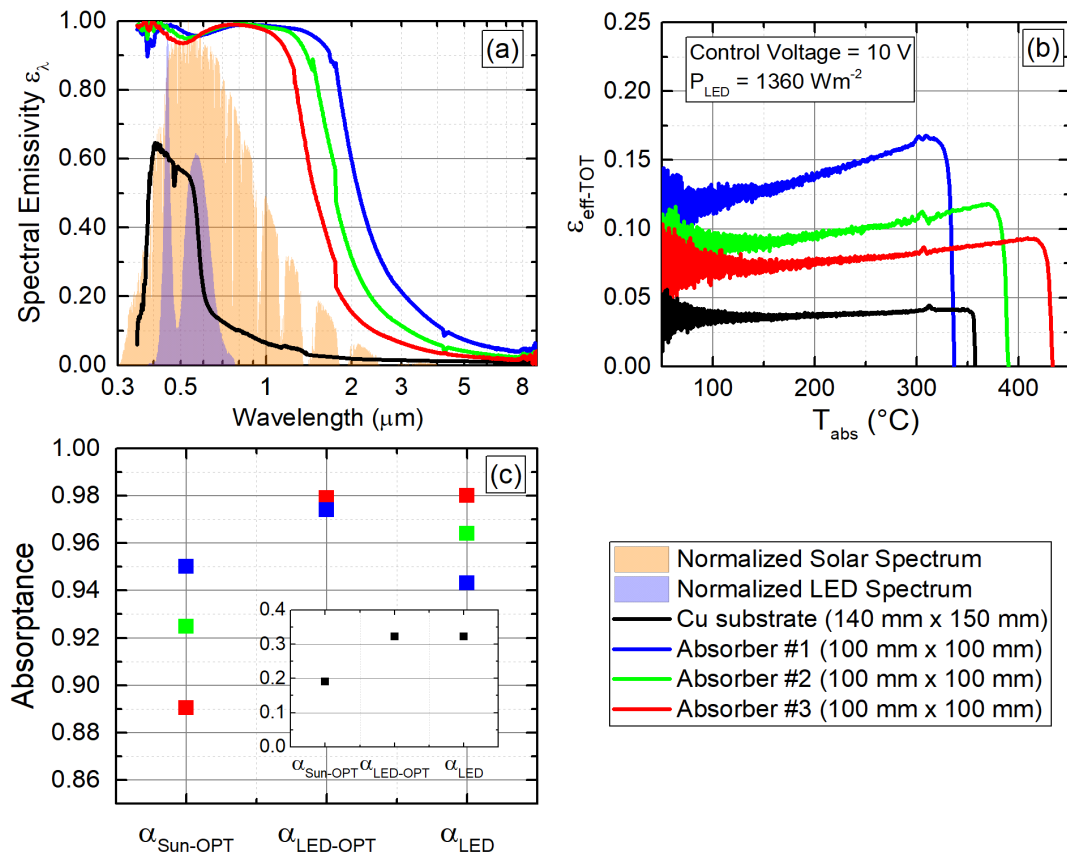


**Fig. 3.7** Experimental results for the proposed three absorbers and the bare copper foil. (a) Optical analysis of reflectivity reveals a slight intrinsic selectivity of the base copper and a good selectivity of the three absorbers. Absorber #3 has the shortest wavelength range of high emissivity, while absorber #1 the largest. This behaviour reflects the choice of the deposited thicknesses of **Tab. 3.4**. (b) The calorimetric tests were performed indoor and the thermal emittances of the three absorbers and the bare copper foil are reported. The absorber #3 has the lowest emittance out of the three proposed absorbers. (c) Solar absorbance  $\alpha_{\text{Sun-OPT}}$  and LED light absorbance  $\alpha_{\text{LED-OPT}}$  are estimated through the optical analysis, while  $\alpha_{\text{LED}}$  by means of the indoor testing.

**Fig. 3.7(a)** summarizes the optical response of the three absorbers and of the bare copper substrate in terms of spectral emissivity  $\varepsilon_\lambda$  versus the wavelength. In the same figure are reported also the normalized spectrums of the Sun and of the LED adopted for the calorimetric indoor testing. The bare copper has a slight intrinsic selectivity with enhanced absorbance in the visible range. The shift from absorbing to reflective behaviour occurs roughly at 0.6  $\mu\text{m}$ , explaining the characteristic reddish colour of copper. Absorbers #1, #2 and #3 show high selectivity, consistent with the solar thermal application. The different thicknesses of the layers impact the selectivity as expected. Absorber #1, which has the thickest layers, has the widest wavelength interval for the solar radiation absorption, and as consequence, the transition to low emissivity values occurs at longer wavelengths. As the thicknesses decrease from absorber #1 to #2 and #3, the solar absorption interval becomes shorter and the transition to low- $\varepsilon_\lambda$  is anticipated to shorter wavelengths. The change of the thicknesses of the proposed multilayer is effective to move the transition from high to low spectral emissivity among the

wavelengths, giving the chance to find the best compromise between solar radiation absorptance and thermal emittance.

In **Fig. 3.7(b)** are shown the total effective thermal emittances of the three absorbers and of the uncoated copper as function of the absorber temperature  $T_{\text{abs}}$ , measured during indoor calorimetric tests. The control voltage was set at its maximum of 10 V with the LED lamps emitting the total integral power density of  $1360 \text{ Wm}^{-2}$ . The LED irradiation was chosen to its maximum in order to extrapolate the thermal emittances for the largest possible temperature range. The maximum temperature of each test, i.e., the stagnation temperature, can be read from the measured emittance curve in correspondence of the anomaly due to the thermocouple fastening. Thanks to the partial light absorption of copper in the LED spectrum and to the extremely low thermal emittance, the stagnation temperature of the bare substrate reached  $358 \text{ }^\circ\text{C}$ . Its total emittance  $\varepsilon_{\text{eff-TOT}}$  is very low and quite constant over the whole temperature range with a value roughly of 0.04. The absorbers #1, #2 and #3 revealed higher emittances than the bare copper, following the same trend observed with the optical analysis. Apart from the increase of the absolute values, what emerges is also an augmented rate of increase of the emittance with temperature, returning three emittance curves sensibly different. The stagnation temperatures of  $337 \text{ }^\circ\text{C}$ ,  $390 \text{ }^\circ\text{C}$  and  $433 \text{ }^\circ\text{C}$ , respectively for absorber #1, #2 and #3, underline the importance of the emittance over the LED light absorptance since the latter slightly changed among the three absorbers.

In **Fig. 3.7(c)** the light absorptances are reported for the LED spectrum,  $\alpha_{\text{LED-OPT}}$  measured optically and  $\alpha_{\text{LED}}$  calorimetrically, together with the optical measurement of the solar absorptance  $\alpha_{\text{Sun-OPT}}$ . The optical LED absorptance  $\alpha_{\text{LED-OPT}}$  has very similar values for all the three, ranging from 0.974 to 0.979, because of the narrow wavelength window of the emitted LED light. The calorimetric response of the LED light absorptance  $\alpha_{\text{LED}}$  has values of 0.980, 0.964 and 0.942 for absorber #3, #2 and #1, respectively. These deviations from the optical estimation of LED light absorptance could be justified by the presence of the thermocouple bolt. It has a lower absorptance than the coating, and its presence becomes more important when the temperature derivative of the absorber is lower, i.e., the Warm-Up phase is slower. As seen from **Fig. 3.7(b)**, absorber #1 has the highest emittance, so the lowest temperature derivative out of the three absorbers, being surely the most affected by the role of the thermocouple bolt (indeed has the lowest  $\alpha_{\text{LED}}$ ). Even if there is a discrepancy between the optical and calorimetric response under the LED light, it is minimal and below 4%.

The concrete performance of the absorber must be considered for its solar absorptance, and its optical measurement returned 0.950 for absorber #1, the highest of the three, while absorbers #2 and #3 have 0.924 and 0.890, respectively. In **Fig. 3.7(c)**, there is also reported as inset the absorptances of the bare copper substrate. Its optical solar absorptance  $\alpha_{\text{Sun-OPT}}$  is 0.190, while  $\alpha_{\text{LED-OPT}}$  and  $\alpha_{\text{LED}}$  perfectly match with the value of 0.323, since the copper foil was tested with as a full-sized sample  $140 \text{ mm} \times 150 \text{ mm}$ , accordingly to the original procedure of the calorimetric facility.

These experimental results confirmed the original idea of tuning the solar absorptance and thermal emittance by changing the deposited thicknesses of the layers of the same structure.

Before discussing about the efficiency of the proposed absorbers, here we want to report the results of another experimental characterization of the absorbers. The measurement of the radiative properties was surely the first step to realize the performance, but another important aspect to assess was the stability of such a performance over years of operation. The operating temperatures above  $100 \text{ }^\circ\text{C}$  could speed up the degradation of the coating during the service

life of the panel, negatively affecting the overall performance. To verify the thermal stability of the deposited layers over the copper substrate, a stress test was carried out by use of the calorimetric test facility in its indoor configuration. Such a test consisted in keeping the absorber at a temperature sensibly higher than the operating one for a time interval of the order of hours.

The degradation of thin films can happen through chemical reaction of the deposited materials or through physical interdiffusion of the materials composing the coating [83]. For our application of evacuated thermal panels, the absorber is not exposed to the external air, dust, or humidity, but is kept under high vacuum for all its service life. Under this condition, the coating degradation occurs mainly through the physical interdiffusion of the layers. The high temperatures enhance the diffusion mechanism driven by the concentration gradient of the materials, so that an interdiffusion region appears in between two adjacent layers taking the place of the original discontinuous interface. When the deposited layers are very thin, order of a few tens of nanometres like the proposed coatings, this phenomenon is critical and could eventually deteriorate the absorber to unacceptable levels after some years of operation.

The interdiffusion process can be mathematically formulated by the Arrhenius exponential model, see eq 3.5, and it is the basis of the most used accelerated ageing procedures to qualify solar absorbers [84]. The interdiffusion rate  $K_{diff}$  of two adjacent layers depends linearly on a pre-exponential factor  $D_{Arrh}$  and exponentially to the ratio between the activation energy  $E_T$  and the absolute temperature  $T$  expressed in Kelvin, with  $R$  the universal constant of the ideal gas.

$$K_{diff} = D_{Arrh} e^{\left(-\frac{E_T}{RT}\right)} \quad 3.5$$

The activation energy  $E_T$  is a constant that depends on the sequence of materials of the coating [85], and, to enhance the thermal resistance over the years of operation,  $E_T$  must be as high as possible. On the other hand,  $D_{Arrh}$  is a macroscopic parameter used to quantify the interdiffusion, such as the decrease of the absorber efficiency [86].

The exponential dependency of  $K_{diff}$  on the temperature  $T$  gives the chance to perform accelerated stress tests by increasing the temperature of the test. The operating temperature of the absorber for mid-temperature application keeps typically below 200 °C, i.e., 473 K, and its service life should be of at least of 20 years. Keeping the absorber under extreme high temperatures can make the degradation process fast enough to observe it in laboratory. The stress test was conducted with absorber #3, keeping the sample at its stagnation for two hours under the highest LED light emission. This test is representative for all the three absorbers, since diffusion mechanisms happen at the interfaces (as they share the same layer structure), and absorber #3 has the highest stagnation.

In **Fig. 3.8**, the result of the stress test is reported in terms of temperature of the absorber #3, glass, and vessel of the test facility, respectively  $T_{abs}$ ,  $T_{gla}$  and  $T_{ves}$ , as function of the time, together with the internal pressure. The pumping system guaranteed high vacuum during the whole test ( $< 5 \times 10^{-5}$  mbar), the glass' and the vessel's temperature is stable at 72 °C and 64 °C. The temperature of the absorber  $T_{abs}$  keeps the stagnation of 433 °C over 120 minutes, meaning that the light absorptance and thermal emittance stay unchanged during the stress test. According to eq. 3.5, this test performed at 706 K has an impact on the degradation almost of two orders of magnitude faster than the operation at 473 K, so, the fact that there is no

sensible change of the radiative properties after two hours at 433 °C is the evidence of the stability of the deposited coating.

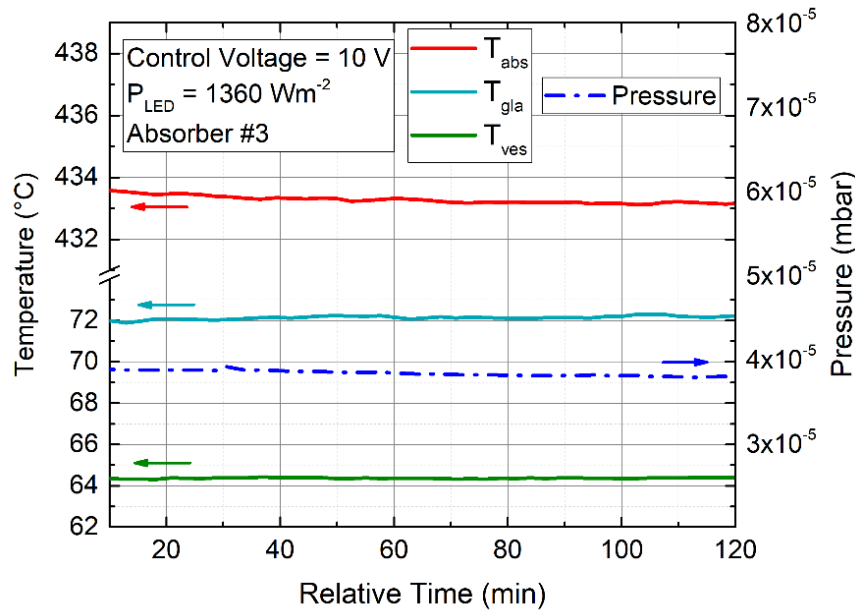


**Fig. 3.8** The stress test of the absorber #3 is reported. The stagnation temperature of 433 °C was kept constant with fixed emitted LED power. This test guarantees the resistance of the absorber to extreme high temperatures, and a constant stagnation temperature means unchanged light absorptance and thermal emittance.

Repeating the same test for a longer time interval and for lower values of the emitted LED light, it is possible to find the value of the activation energy  $E_T$  of the proposed selective coating, extrapolating a value not below 220 kJ/mol. It can be demonstrated that this activation energy is large enough to guarantee a service life not less than 25 years of operation at nominal temperature of 200 °C, as we recently published [87].

### 3.6. Estimation of the Annual Converted Energy

Once the deposited selective coatings have been deposited, characterized about their radiative performance, and even qualified their resistance over years of operations, now it is possible to quantitatively estimate the benefits derivable from the adoption of the proposed absorbers in place of the currently adopted commercial solution within the evacuated unconcentrated flat panel. The commercial absorber of reference is Mirotherm<sup>®</sup>, which is an aluminium foil coated with a selective coating deposited by means of Physical Vapour Deposition techniques, already in use by TVP Solar SA [9] for their evacuated flat panels. The radiative properties of Mirotherm<sup>®</sup> and of the three proposed absorbers had been experimentally measured by means of calorimetric testing and optical analysis of reflectivity, obtaining reliable values of solar radiation absorptance and total effective thermal emittance. Those radiative properties alone cannot return the overall performance of the absorber, so

there is the need for the proper parameter to make quantitative estimations of the converted energy during operation.

In the previous section 1.2, we introduced the absorber efficiency, see eq. 1.12. This parameter is well known in literature and is used to guide the designing process of solar selective coatings. It depends on the solar absorptance and thermal emittance of the coated side of the absorber, whereas the back of the substrate is completely neglected. Starting from the efficiency of eq. 1.12, we can formulate a novel expression for the absorber efficiency taking into the right consideration also the back of the absorber with the use of the total effective thermal emittance  $\varepsilon_{eff-TOT}$ . This new parameter is the Effective Absorber Efficiency  $\eta_{abs-eff}$ , eq. 3.6, and depends on the radiative thermal mechanisms involving the mere absorber.

$$\eta_{abs-eff} = \alpha_{Sun} - \frac{\varepsilon_{eff-TOT} \sigma (T_{abs}^4 - T_{amb}^4)}{P_{Sun}} \quad 3.6$$

$T_{abs}$  and  $T_{amb}$  are the absorber and envelope temperatures, respectively.  $P_{Sun}$  is the solar irradiance. In **Fig. 3.9(a)**, the calculated  $\eta_{abs-eff}$  is proposed for  $P_{Sun} = 1000 \text{ Wm}^{-2}$  and  $T_{amb} = 25 \text{ }^\circ\text{C}$  (as explained previously, the impact on the net emitted radiation of the envelope's temperature is negligible, so we fixed it arbitrarily), in a wide range of  $T_{abs}$  for the three proposed absorbers and for Mirotherm<sup>®</sup>, our reference benchmark. The solar absorptance  $\alpha_{Sun}$  derives from the optical analysis and the thermal emittance  $\varepsilon_{eff-TOT}$  from the fitted curve during the calorimetric test. To ease the reading, they are summarized in **Fig. 3.9(b)**.

At the temperature of  $50 \text{ }^\circ\text{C}$ , absorber #3 has the lowest efficiency of 0.80, absorber #1 the highest with 0.85, while Mirotherm<sup>®</sup> and absorber #2 have the same value of 0.83. This trend is the same of the values of the solar absorptances since the role of thermal emittance is limited due to the low temperature. The rise of the absorber temperature reduces all the efficiency curves for the increased values of thermal emittances and weight on efficiency. Around the temperature of  $100 \text{ }^\circ\text{C}$ , the curves of absorbers #2 and #3 match that of Mirotherm<sup>®</sup> with the value of 0.78, while absorber #3 stays below with 0.76. The further increase of temperature returns the opposite trend of efficiencies, absorber #1 has the lowest and absorber #3 the highest values, following the opposite trend of thermal emittances, see **Fig. 3.9(b)**. At  $T_{abs} = 200 \text{ }^\circ\text{C}$ , absorber #1 has efficiency 0.53, against Mirotherm<sup>®</sup> with 0.59 and absorber #2 and #3 with 0.61 and 0.63, respectively. These differences enlarge as the temperature increases, up to  $317 \text{ }^\circ\text{C}$  with the zero of efficiency for Mirotherm<sup>®</sup>, 0.24 for absorber #2 and 0.35 for absorber #3, while absorber #1 cannot reach such a temperature due to its high emittance.

The calculated Effective Absorber Efficiency  $\eta_{abs-eff}$  confirms the original purpose of producing three different absorbers designed to work at different operating temperature ranges, returning each the best performance in a different range. The comparison with Mirotherm<sup>®</sup> reveals a potential improvement of just a few percent from temperatures of  $50 \text{ }^\circ\text{C}$  to  $150 \text{ }^\circ\text{C}$ , whereas at  $200 \text{ }^\circ\text{C}$  and  $250 \text{ }^\circ\text{C}$ , absorber #3 could respectively reach +0.04 and +0.11 of efficiency, i.e., +7% and +27% of Mirotherm<sup>®</sup> efficiency at the corresponding temperatures.

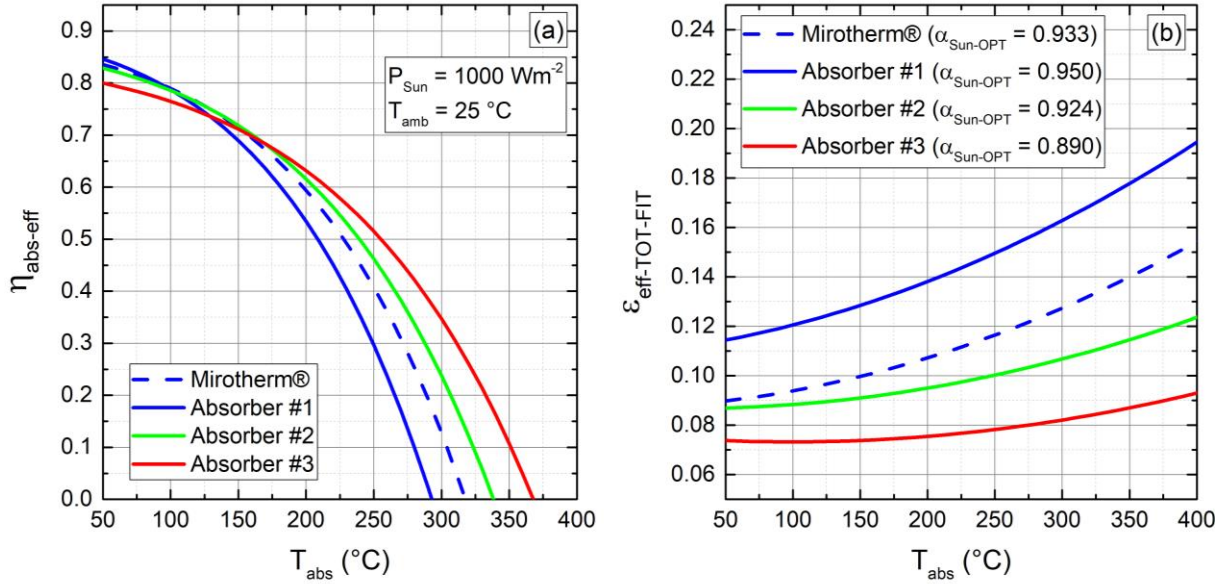


**Fig. 3.9** (a) The Effective Absorber Efficiency, as expressed in eq. 3.7, is shown for the three proposed absorbers and the commercial Mirotherm® at solar irradiance of  $1000 \text{ Wm}^{-2}$  and ambient temperature of  $25 \text{ °C}$ . The radiative properties used to calculate such an efficiency derive from the optical analysis and the calorimetric testing (b).

The proposed analysis of the Effective Absorber Efficiency has some intrinsic limits, and the real potential of the proposed absorbers has not yet been accurately assessed. Eq. 3.6 returns exclusively the absorber efficiency for a fixed solar irradiation, while the overall efficiency of the collector deals with a transient solar irradiation, conductive thermal losses due to contact of the absorber with its supporting structure and with the exit ports of the pipeline, and its net absorbing surface is a fraction of the gross area of the collector due to the holes to host the pin rack structure and the needed space for the frame of the envelope.

Here, a novel expression of the panel efficiency  $\eta_{\text{panel}}$  is proposed, written as eq. 3.7, to consider not only the radiative properties of the absorber, but also all the mentioned aspects that have a role for the overall conversion efficiency. The light absorption mechanism is modelled as the product between the solar absorptance  $\alpha_{\text{Sun}}$  and the glass transparency  $\tau_{\text{gla}}$ , corrected by the fraction of the net absorbing area on the gross surface by the ratio  $A_{\text{net}}/A_{\text{gross}}$ . There are two thermal loss terms, the first is the radiative emission of the absorber and depends on the effective total emittance  $\epsilon_{\text{eff-TOT}}$  multiplied to the difference of the fourth power of the absorber and envelope temperatures, respectively  $T_{\text{abs}}$  and  $T_{\text{amb}}$ , counting only for the net area. The other is a conduction contribution and is governed by a single parameter  $K_{\text{cond}}$  which group all the conductive losses of the absorber and multiplies  $T_{\text{abs}} - T_{\text{amb}}$ . These two losses are normalized to the incident solar power over the gross area of the panel by the product  $P_{\text{Sun}} \times A_{\text{gross}}$ .

$$\eta_{\text{panel}} = \frac{A_{\text{net}}}{A_{\text{gross}}} \alpha_{\text{Sun}} \tau_{\text{gla}} - \frac{A_{\text{net}} \epsilon_{\text{eff-TOT}} \sigma (T_{\text{abs}}^4 - T_{\text{amb}}^4) + K_{\text{cond}} (T_{\text{abs}} - T_{\text{amb}})}{P_{\text{Sun}} A_{\text{gross}}} \quad 3.7$$

To calculate the panel efficiency according to eq. 3.7, we need first to define the parameters  $\tau_{\text{gla}}$ ,  $A_{\text{net}}$ ,  $A_{\text{gross}}$  and  $K_{\text{cond}}$ . They strictly depend on the design of the collector, but not on the type of adopted absorber. This means that the substitution of the commercial absorber with one of the proposed would, in first approximation, change only the radiative properties of the absorber notwithstanding the others. The comparison of Mirotherm<sup>®</sup> with the three proposed absorbers is extended to the panel efficiency  $\eta_{\text{panel}}$  assuming as evacuated flat envelope of reference that from TVP Solar SA, the only available on the market [9].  $A_{\text{net}}$ ,  $A_{\text{gross}}$ , and  $\tau_{\text{gla}}$  were revealed by the company as equal to 1.96 m<sup>2</sup>, 1.72 m<sup>2</sup> and 0.925, respectively, whereas no information was revealed about  $K_{\text{cond}}$ . Fortunately, the datasheet of the panel shows the certified overall efficiency according to EN ISO 9806:2013 and ICC 901/SRCC 100-2015 with the collector equipped with Mirotherm<sup>®</sup>, so it is possible to extrapolate  $K_{\text{cond}}$  by comparison of the formulated panel efficiency of eq. 3.7 (adopting all the information we have about the commercial absorber and the features of the panel) with the certified curve.

In Fig. 3.10, the certified panel efficiency (dashed blue line) is reported for  $P_{\text{Sun}} = 1000 \text{ Wm}^{-2}$  and for  $T_{\text{amb}} = 25 \text{ °C}$  as function of the absorber temperature  $T_{\text{abs}}$  in the range 50-210 °C. For sake of comprehension, the effective absorber efficiency of eq. 3.6 (black dot-dash line) is reported too and, as expected, has values higher than the panel efficiency. Assumed a value of  $K_{\text{cond}}$  of  $0.70 \text{ WK}^{-1}$  and the temperature of the envelope equal to  $T_{\text{amb}}$ , the overall panel efficiency modelled by eq. 3.7 (red solid line) perfectly matches the certified curve. This means that a single parameter can be used to group together all the thermal losses not related to radiation, validating the proposed formulation of panel efficiency.

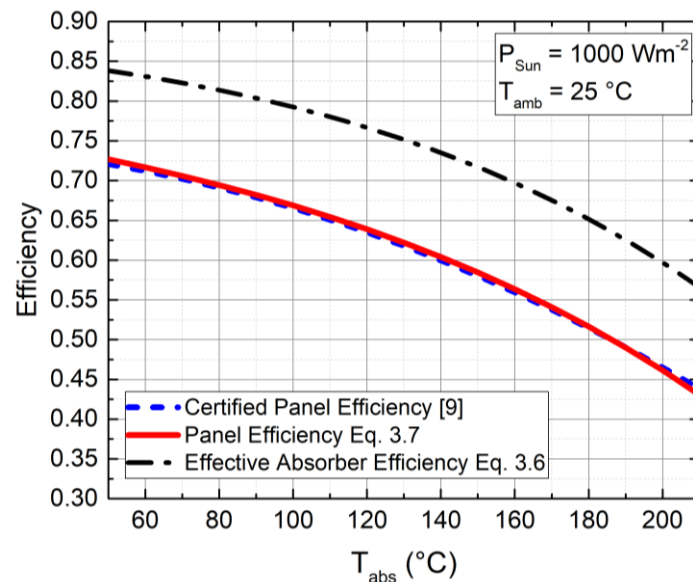


**Fig. 3.10** The certified panel efficiency declared by TVP Solar SA [9] is compared to the Effective Absorber Efficiency, eq. 3.6, and to the proposed formulation of the panel efficiency, eq. 3.7, adopting  $K_{\text{cond}} = 0.70 \text{ WK}^{-1}$  as conduction parameter to model the conductive thermal losses.

Once the conductive term  $K_{\text{cond}}$  has been calibrated to  $0.70 \text{ WK}^{-1}$  through to the certified panel efficiency, calculations of the expected panel efficiency with the adoption of the

proposed absorbers were carried out by means of eq. 3.7. In **Fig. 3.11**, the calculated panel efficiency is reported as function of the operating absorber temperature  $T_{\text{abs}}$  for the adoption of the three proposed absorbers and Mirotherm® at three different solar power irradiances  $P_{\text{Sun}} = 200 \text{ Wm}^{-2}$ ,  $500 \text{ Wm}^{-2}$  and  $1000 \text{ Wm}^{-2}$ . **Fig. 3.11(a)** stands for  $P_{\text{Sun}} = 200 \text{ Wm}^{-2}$  and because of the low solar irradiance, the panel efficiency shows a fast drop with temperature for all the four absorbers and none of them reaches the threshold of  $200 \text{ }^\circ\text{C}$  of operating temperature. In addition, in the range  $50 \text{ }^\circ\text{C} - 75 \text{ }^\circ\text{C}$ , they return roughly the same response, and no significant difference can be observed. This is consequence of the increased importance of thermal emittance over the solar absorptance when the irradiation is low, combined to the fact that the absorbers with the highest absorptances have also the highest emittances. In the same range of temperature, the increase of the solar irradiance to **(b)**  $500 \text{ Wm}^{-2}$  and **(c)**  $1000 \text{ Wm}^{-2}$  reveals panel efficiencies following the same trend of the solar absorptances, similarly to what observed for the absorber efficiency. On the other hand, for each fixed solar irradiance, the increase of temperature returns panel efficiencies shaped by the thermal emittances.

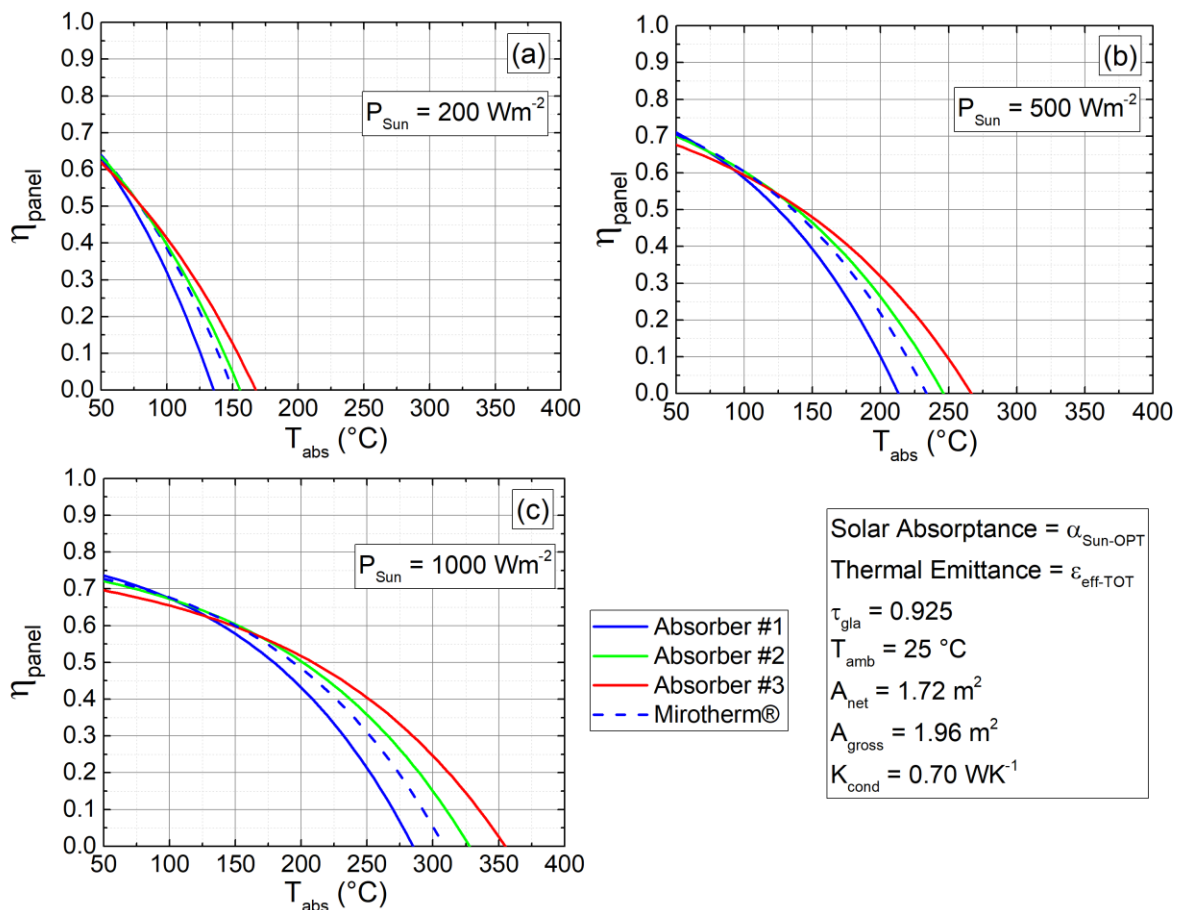


**Fig. 3.11** The panel efficiency calculated through equation 3.7 is reported for three different solar power irradiances (a)  $200 \text{ Wm}^{-2}$ , (b)  $500 \text{ Wm}^{-2}$  and (c)  $1000 \text{ Wm}^{-2}$ . The details of the calculation are shown in a table in the figure. The behaviour of the three proposed absorbers is similar what seen with the Effective Absorber Efficiency, but for lower values of efficiency. As the solar power reduces, the panel efficiency drops faster with the operating temperature.

The temperature at which all the efficiency meet increases as the solar irradiance increases, being 75 °C at  $P_{\text{Sun}} = 200 \text{ Wm}^{-2}$ , 90 °C at  $P_{\text{Sun}} = 500 \text{ Wm}^{-2}$  and 130 °C at  $P_{\text{Sun}} = 1000 \text{ Wm}^{-2}$ . Comparing the performances in the temperature range 150 °C – 200 °C of the peak irradiance (c) with the reduced value of (b)  $500 \text{ Wm}^{-2}$ , the benefit of using absorber #3 instead of Mirotherm® is less pronounced. Indeed, at  $500 \text{ Wm}^{-2}$ , the improvement with respect to Mirotherm® in that  $T_{\text{abs}}$  range is of the order of 15%, whereas at  $1000 \text{ Wm}^{-2}$  it reduces to a few percent. The use of one of the three proposed absorbers in place of the commercial solution impacts positively or negatively on the panel efficiency depending on the absorber temperature and the level of solar irradiance. To consider all these aspects simultaneously and give them the right weight, simulations of the annual converted energy are proposed when the four absorbers are adopted for the evacuated panel.

The proposed analysis is based on eq. 3.7 of panel efficiency combined with the data of annual solar irradiance available online from the European Commission website [88]. The database provides detailed information about the net solar irradiance incident over a panel and the mean temperature of the atmospheric air when it is placed in a specific city with a fixed tilt and azimuth angles. These data are discretized for each hour of the day, and there are twelve averaged days, one for each month. The year is the succession of twelve different characteristic days repeated in groups like the months.

Based on this discretization, **Fig. 3.12(a)** is the total solar energy incident over the panel for every month of the year when it is installed in Naples (40° 51' N, 14° 18' E - Italy) with a 35° of tilt angle and 0° azimuth. As seen previously, the panel efficiency at a certain temperature is positive only when the solar irradiance reaches a value high enough. For instance, at irradiance of  $200 \text{ Wm}^{-2}$  none of the proposed absorbers could bring the panel to a working temperature as high as 200 °C, see previous **Fig. 3.11(a)**. This means that not all the incident solar energy can be effectively converted, since part of it hits the panel with a power not large enough to sustain the desired temperature, like at the first and latest hours of each day. When this happens, we assume that the panel is not operative during the whole hour. In **Fig. 3.12(b)**, the resulting mean panel efficiency is calculated for each month adopting the three proposed absorbers and Mirotherm®, imposing that the envelope temperature is equal to the ambient at each specific hour, and that the operating temperature is fixed at 200 °C. The four absorbers return a positive panel efficiency for every month of the year, with lower values in those months when the solar irradiance is lower. The monthly irradiated energy in July and August is maximum, while it reaches the minimum in January and December. The reduction of irradiation from  $800 \text{ MJm}^{-2}$  of the two summer months to  $350 \text{ MJm}^{-2}$  of those of winter is not matched by the change of the monthly panel efficiency for each absorber. Indeed, they reveal a stronger reduction of efficiency from summer to winter, consequence of the reduction of solar power intensity and number of irradiation hours when shifting from summer to winter days. Each absorber experiences a different level of reduction. Mirotherm® shifts from 0.35 of monthly panel efficiency in summer to 0.12 of winter, a third of the value. On the contrary, Absorber #3 passes from 0.40 to 0.20, keeping the same 2:1 ratio of the solar irradiance. This is possible thanks to the lower thermal emittance of absorber #3 than Mirotherm®, allowing to work with sensibly higher efficiency under low and medium solar irradiances, as seen in **Fig. 3.11(b)**. Absorber #2 has a monthly efficiency that is intermediate between absorber #3 and Mirotherm®, while absorber #1 has the lowest efficiency in every month and its variation from summer and winter months is the highest, from 0.28 to 0.04.

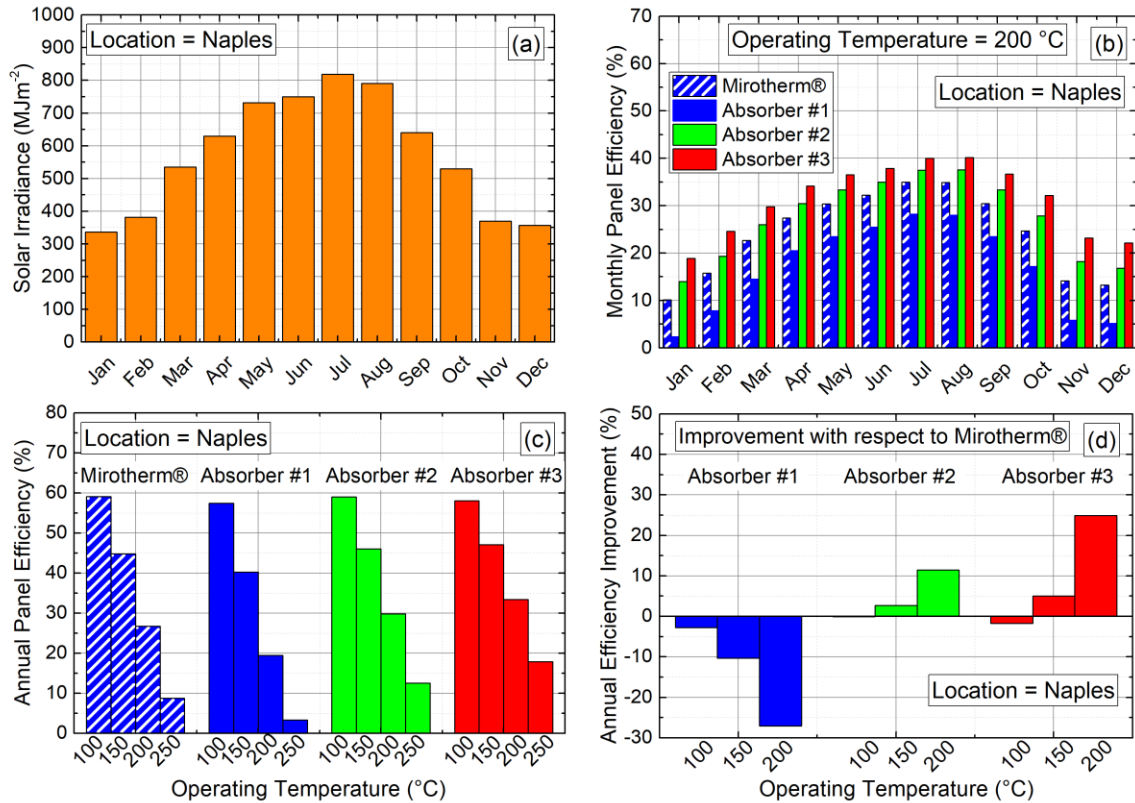


**Fig. 3.12** Simulations of the panel efficiency through eq. 3.7 on a monthly and annual basis for the three proposed absorbers and the commercial Mirotherm<sup>®</sup>. The location is Naples (Italy), tilt angle 35° and azimuth 0°. (a) Sola energy incident over the panel on a monthly basis [88]. (b) Monthly panel efficiency for an operating temperature of 200 °C. (c) Annual panel efficiency for 100-150-200-250 °C of operating temperatures. (d) Relative percentage improvement of annual panel efficiency with respect to Mirotherm<sup>®</sup> for 100-150-200 °C of working temperature.

Repeating the calculation for a set of operating temperatures, 100 – 150 – 200 – 250 °C, the annual efficiency of the panel can be calculated and is reported in **Fig. 3.11(c)**, while **Fig. 3.11(d)** is the relative percentage improvement by use of absorber #1, #2 and #3 with respect to Mirotherm<sup>®</sup>. 100 °C of working temperature returns a converted energy comparable for all the four absorbers, with deviations from Mirotherm<sup>®</sup> within -3% (panel efficiency of 0.590 for Mirotherm<sup>®</sup>, 0.575 for absorber #1, 0.590 for absorber #2, and 0.580 for absorber #3).

At increased operating temperatures the scenario is different. Absorber #1 returns an annual panel efficiency lower than Mirotherm<sup>®</sup>, while absorbers #2 and #3 show a better response. At 150 °C of operating temperature, Mirotherm<sup>®</sup> gives 0.451 of efficiency, while absorber #1 returns 0.406 (-10% compared to Mirotherm<sup>®</sup>), absorber #2 0.461 (+2.5%), and absorber #3 0.473 (+ 5.1%). A further increase of the working temperature would emphasize these differences, indeed, at 200 °C Mirotherm<sup>®</sup> shows an efficiency of 0.268, absorber #1 0.195 (-27.2%), absorber #2 0.298 (+11.2%), and absorber #3 0.335 (+ 24.9%).

The negative response of absorber #1 with respect to Mirotherm<sup>®</sup> is to be addressed to the deposited layers thicknesses which were chosen to maximize the solar absorptance at the expense of thermal emittance. Its nominal operation was assumed to be at low temperatures

(< 100 °C), range not investigated due to the interest on mid-temperatures for the evacuated flat panel.

The improvement on panel efficiency thanks to absorber #2 in the range 100 °C – 150 °C is minimal, of the order of a few percent, then even surpassed at 150 °C by absorber #3 with an increased annual efficiency of +5.1% with respect to Mirotherm®. The benefit of using absorber #3 instead of the commercial is substantial (+24.9%) at operating temperature as high as 200 °C. A lower solar radiation absorptance (0.933 for Mirotherm® and 0.890 for absorber #3) is fully compensated by an extremely contained value of thermal emittance at that temperature (0.1069 for Mirotherm® and 0.0755 for absorber #3) allowing an annual panel efficiency of 0.335 against 0.268 of the commercial solution.

A working temperature of 250 °C would make the annual efficiency for all the four absorbers too low to be effectively used (< 0.10 for Mirotherm® and absorber #1, around 0.15 for absorber #2 and #3). The relative increase with respect to the commercial solution at 250 °C is not reported in **Fig. 3.11(d)** for sake of easiness, since the improvement of absorber #3 is +100% (0.18 against 0.09), but not interesting for its low absolute annual value.

The original aim of producing and characterize a solar thermal absorber properly designed to work at mid-temperatures (100 °C – 200 °C) for the evacuated flat panel has been achieved. The results confirmed the benefit of reducing the absorber's thermal emittance at the expense of a less absorptive coating. The choice of the proper absorber depends on the specific mid-temperature interval of application, 100 °C – 150 °C or 150 °C – 200 °C, since the whole mid-temperature range 100 °C – 200 °C is relatively too wide for one type of absorber. Indeed, the weighting factor  $w$  moves from 0.65 at 100 °C to 2.4 at 200 °C, meaning that the role of absorptance and emittance completely changes at the extremes. Contextually, the two sub-intervals of temperatures belong to different industrial applications, allowing the net distinction between the two types of panels (the same vacuum envelope could be equipped with absorber #2 or #3), each designed to work for its specific temperature range.

## 4. Coating Deposition by Roll-to-Roll Sputtering Machine

The aim of this section is to demonstrate the feasibility to deposit the proposed coating at industrial scale. This part of the activity has been conducted at TVP Solar SA in Geneva (Switzerland) as period abroad during my PhD course.

In the first section 4.1, the industrial experimental setup used to carry out sputtering depositions of the selective coating is described. In the following section 4.2, there is the design and testing of a novel magnet pack that overcomes all the technical limits of the current commercial solution. In the last paragraph 4.4, the top layer of the coating, antireflective SiO<sub>2</sub>, was deposited both by RF 13.56 MHz sputtering and DC reactive from the Si target, demonstrating the applicability of the DC reactive technology at industrial scale.

The outcome of this activity is to prove that the full selective coating can be fully deposited by use of two targets, Cr and Si, in DC reactive sputtering mode, reducing costs and experimental setup of the dedicated industrial deposition machine.

### 4.1. Roll-to-Roll Industrial Sputtering Machine

The adopted industrial machine is depicted in **Fig. 4.1**. Originally the machine was designed to deposit getter materials for vacuum applications, such as Titanium, Vanadium and Zirconium, over aluminium ribbons in DC Magnetron Sputtering starting from the proper metallic target. **Fig. 4.1(a)** is the picture of the machine from the external as it was set in the laboratory. The system was surrounded by a protective structure against possible injuries for the operators due to the high voltages and hot surfaces. The vacuum chamber was a cylindrical body with two targets set on two opposite sides of its lateral surfaces, and the ribbon is placed internally on a cart which sustained and moved the ribbon thanks to a roll-to-roll architecture. The cart is attached to the entry flange, and when the cart is inserted into the chamber, the flange closes the cylindrical body with Viton gaskets. The scheme of the rolling system mounted on the cart is shown in **Fig. 4.1(b)**. The deposition over the moving substrate in front of the targets was possible by unrolling the uncoated ribbon, point A, and directing it through the rolling bars, from point B to G, and then the coated substrate was rolled in H. The bar C was the only equipped with a load cell to keep the foil of the ribbon in tension, flat and parallel to the target. Thanks to this specific roll-to-roll architecture, the two targets deposited simultaneously over the two sides of the foil.

The scope of our activity was different from the nominal usage of the machine, as we needed to deposit coatings for solar thermal applications over copper ribbons (and not getters over aluminium), but the installation of the copper ribbon (50 m long, 1 m wide and 0.2 mm thick) and of the proper targets was easy allowing the effective usage of this industrial machine for our tests. **Fig. 4.1(c)** is the picture of the copper ribbon mounted on the bar A with the entry flange open. When the mounting procedure of the foil from bar A to H was done, the cart was pushed inside with the flange closing the chamber. Similarly to the batch laboratory machine showed before, also here there was a quartz view port to observe the plasma induced during the process, see **Fig. 4.1(d)**.

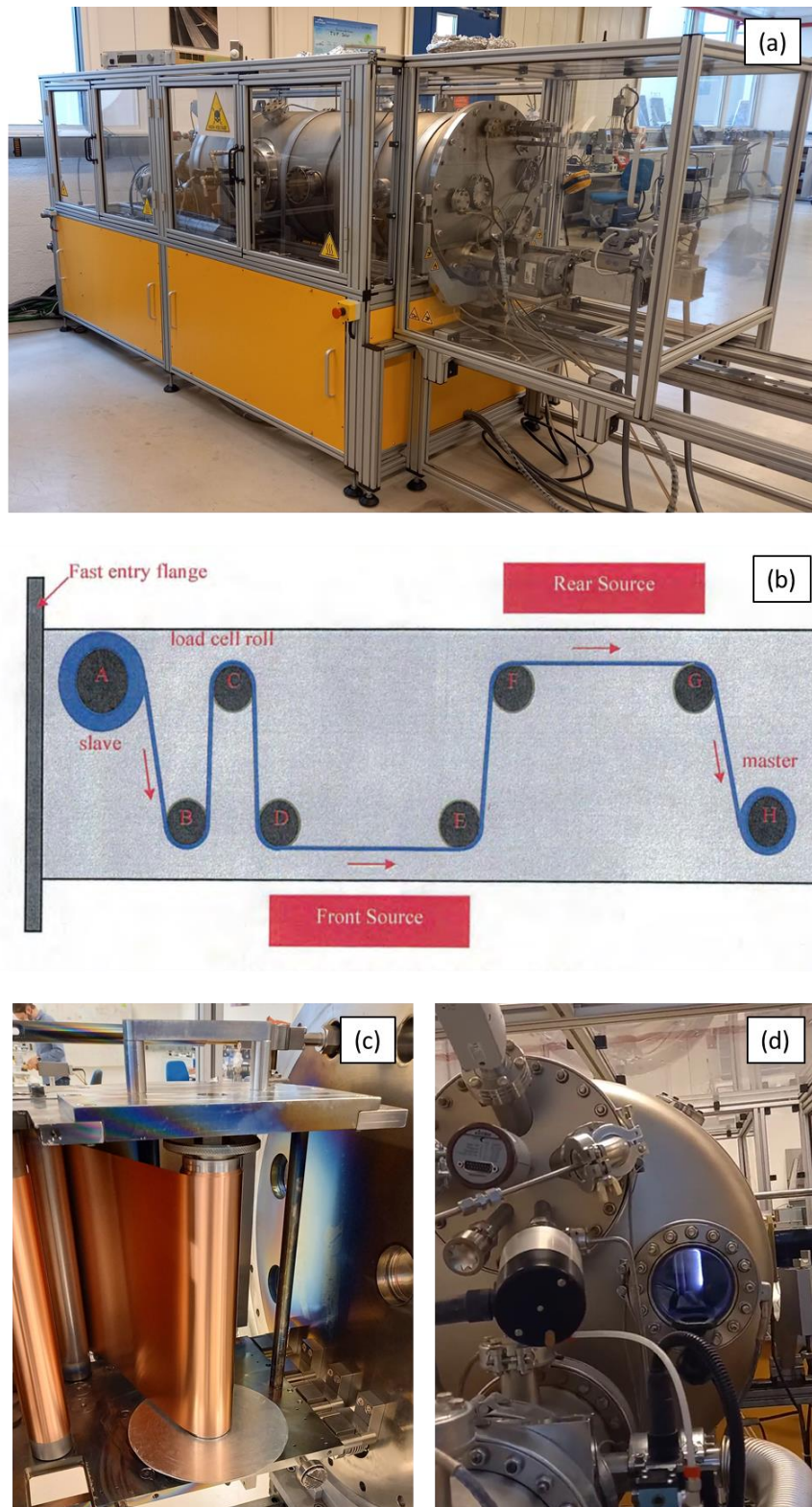


**Fig. 4.1** Pictures of the experimental setup of the industrial roll-to-roll sputtering machine. (a) The external of the machine with its protective structure. (b) Scheme of operation of the rolling system. (c) Roll "A" with the copper ribbon correctly installed on the cart. (d) Picture of the plasma induced by the sputtering process through a quartz view port.

The chamber was evacuated by a pumping system analogous to that seen with the laboratory batch machine, rotative and turbomolecular pump in series, but here there were two different strategies to reduce the flux collected by the turbopump during the injection of the process gases. One was to pump the chamber through the main gate with the turbopump at half of its rotational speed, from the maximum value of 833 Hz to 417 Hz. The other was to pump the chamber through a bypass pipeline whose flow conductance was one order of magnitude lower than the nominal 500 l/s of the turbopump. This double chance allowed two pumping modes, the first for high and the second for low pumping speed.

In **Fig. 4.2** there are pictures of the target and its supporting structure.

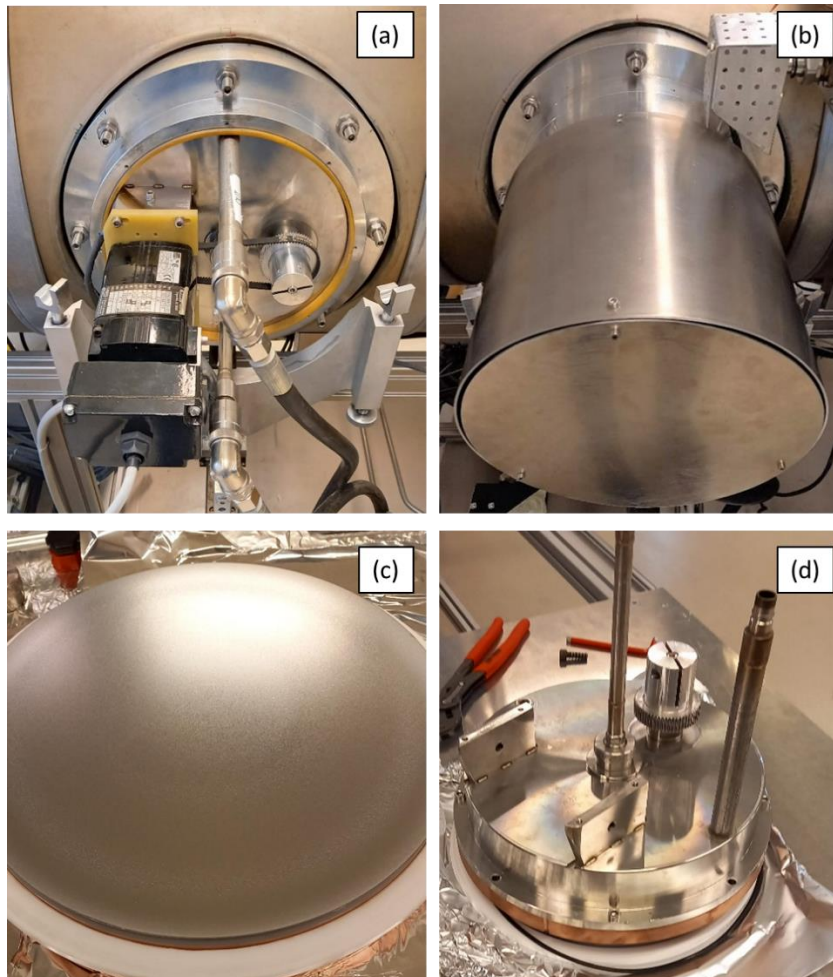


**Fig. 4.2** Pictures of the target holder. (a) The holder is mounted on the lateral wall of the vacuum chamber. The electric motor moves a gear to guarantee the rotation of magnet pack, there are inlet and outlet pipes for the cooling water. The power supply is electrically connected to the holder. (b) The back of the target holder is covered with a grounded aluminium shield for the safety of operators. (c) The sputtered surface of the Cr target of 10 inches of diameter. (d) The target is stuck to a copper support which is fastened to a stainless-steel body to host the rotating magnet pack.

**Fig. 4.2(a)** shows the back of one of the two the target holders where it is possible to see the piping system for the cooling water (inlet and outlet ports), and the electric motor moving a gear through a rubber belt to rotate the magnet pack inside the target holder. The back of

the target holder was electrically connected to the power supply, so the proper electrical insulation from the rest of the grounded chamber was guaranteed by plastic gaskets (the yellow ring in (a) and the white in (c)).

To guarantee the safety of the personnel in the laboratory, the back of the target holder is covered with a grounded aluminium shield to avoid the risk of contact with electrically charged surfaces, as shown in Fig. 4.2(b). A picture of the Cr target is reported in Fig. 4.2(c). It is a disc of 10 inches of diameter stuck on the copper support which in turn is fastened to the stainless-steel back-cover of the holder, see Fig. 4.2(d). Between the back of the copper holder and the stainless-steel support was inserted the magnet pack. It was connected to the gear for a continuous rotation while immersed in the cooling water. Such a water cooled both the target and the magnet pack, avoiding potential damages due to high temperatures.

In Fig. 4.3 the magnet pack is shown. It is a commercial device properly designed for circular targets with diameter of 10 inches. Fig. 4.3 (a) is the frontal view of the device which was composed of permanent magnets (mainly trapezoidal) arranged in a heart-shaped configuration, embedded in an epoxy matrix to guarantee the water resistance. More about this geometry is discussed in the next section 4.2. The magnet pack has a central hole with a pentagon-like shape to allow the water to enter and radially move within the interspace between the pack and the rear of the target holder. The central metallic ring that can be seen in (a) is a part of the stainless-steel support that fixes the pack with the water pipe. In Fig. 4.3(b), the picture of the rear of the magnet pack is reported with its support and water pipe mounted on the copper of the target holder. Because of the working conditions of the magnet pack (2 Hz of continuous rotation immersed in a flux of cooling water), it undergoes a severe erosion process, see Fig. 4.3(c). After a few thousand hours of operation, the erosion of the water opened some cracks into the epoxy and penetrated oxidating the magnets. The degradation of the magnets could cause the change of the deposition conditions (for the reduction of the magnetic field intensity), or even the blockage of the pack due to friction between the epoxy and the copper support for the protrusion caused by the oxidated magnets.

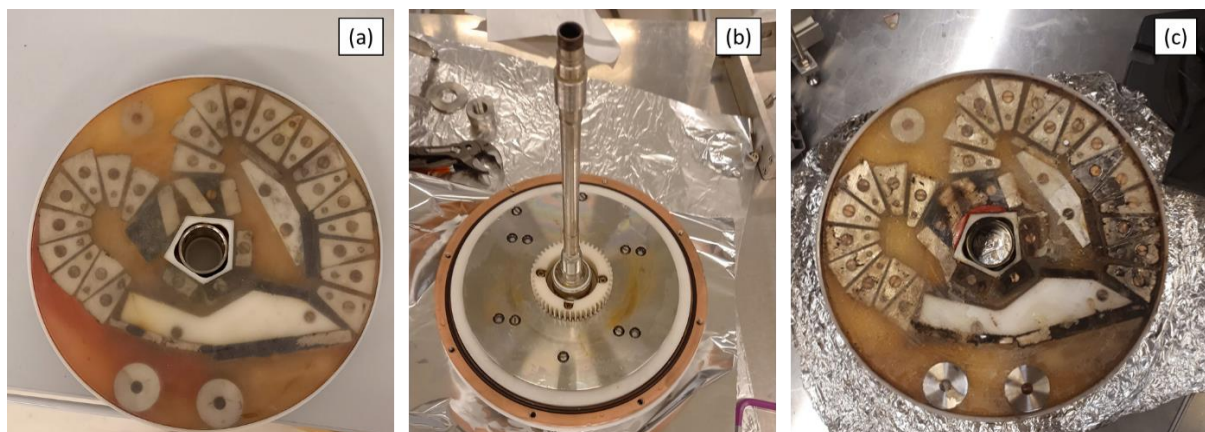


**Fig. 4.3** The commercial magnet pack adopted for the industrial deposition machine is shown. (a) Frontal view of the magnet pack after the regular maintenance procedure. (b) Back of the magnet pack when installed on the back of the copper support of the target. (c) The magnet pack damaged by the erosion of the cooling water. The top layer of the epoxy is partially removed, and some magnets are oxidized.

To overcome these issues, the maintenance of this device is mandatory and consists of the mechanical removal of the top epoxy layer and of the oxide, then dried of eventual residuals of water and covered again by an extra epoxy. These processes are time consuming and not always easy to perform. For instance, the removal of the damaged epoxy is critical with high probability to destroy some of the magnets, since the manufacturing tools are metallic and tend to be attracted by the magnetic field. Then, the additional epoxy should be degassed before the application (air bubbles are potential cause of the cracks), and after the application the curing of the epoxy consists of leaving the manufactured piece in oven at temperature of 75 °C for not less than 3 hours. So that, before any deposition test, the research activity was focused on the design of a novel magnet pack able to overcome all the maintenance issues and be a perfect alternative to the commercial solution already in use. Then, the whole deposition activity was performed using the novel pack.

The described roll-to-roll machine was already equipped with the 10 inches Cr target, the injection lines of Ar and O<sub>2</sub>, and with the DC power supply, so it was ready for deposition tests of the Cr and Cr<sub>2</sub>O<sub>3</sub> layers from the same target, as done previously with the batch machine in laboratory. On the other hand, the industrial machine was not designed to deposit materials such as SiO<sub>2</sub> and the needed adjustments are discussed in the paragraph 4.4.

#### 4.2. *Design of the Novel Magnet Pack*

Magnetron Sputtering is a deposition technique well known in literature and it has been developed for various applications. The magnetic field is needed to sustain the ionization of the process gas, in our case Ar, when the pressure in chamber is as low as 10<sup>-3</sup> mbar. When the magnetic field is not strong enough, the ionization cascade is unstable, and an increased pressure of the process gas is needed to sustain the continuity. As explained in the previous section 3.3, the component of magnetic field parallel to the target surface is cause of the increased path of the electrons, giving them a helicoidal displacement in place of the straight direction driven by the negative potential of the target. The enhanced probability of interaction of electrons with the Argon particles increases the number of produced ions Ar<sup>+</sup>, allowing the stability of the process.

The magnetic field is commonly provided by permanent magnets, and, depending on how they are placed with respect to the plane of the target, they provide a different parallel component of the magnetic field. In **Fig. 4.4**, the two possible configurations are reported. The dashed line represents the plane of the target and, when the polarization of the magnets is orthogonal to this plane, the parallel component of the field can be maximized by use of two magnets with reversed polarization and close enough to properly curve the lines of the magnetic field. When the polarization is parallel, a single magnet is enough to locally provide the parallel field, but shape and intensity reduce faster with the distance. In general, there is no rule to suggest which of the two is the best solution, but it must be chosen according to geometrical constraints, maximum allowable pressure, and the required erosion uniformity for each specific sputtering application.

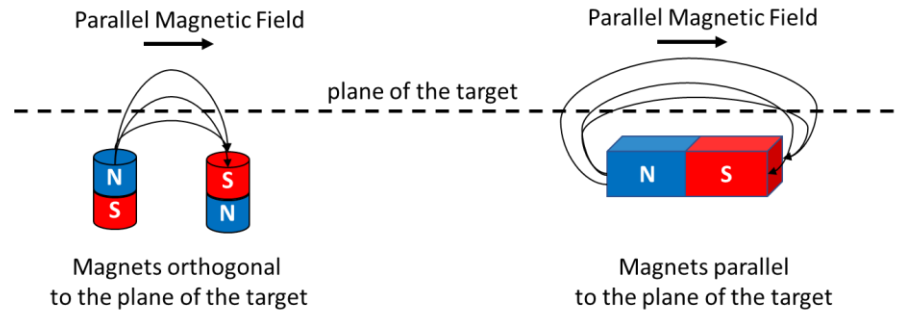


**Fig. 4.4** The component of the magnetic field parallel to the plane of the target can be obtained by two approaches. One is the couple of magnets with orthogonal polarization to the target plane (on the left). The other consists of a magnet polarized parallelly to the plane (on the right).

The problem of the optimal geometrical shape of the parallel component of the magnetic field is well known in literature [89]. There are multiple aspects to fulfil simultaneously, such as the uniformity of the deposited coating, uniformity of the target erosion and the low operating pressure. The first two are strictly linked to the geometry of the magnetic field, whereas the last on the intensity, typically in the range 0.01 T - 0.1 T.

As regards the geometry of the parallel component of the magnetic field, there are two optimal solutions for the circular target and are reported in **Fig. 4.5(a)** and **Fig. 4.5(b)** as result of the analytical constrained optimization [90]. In **(a)**, the optimal layout of the parallel component for small scale targets is a concentric circle. This architecture provides a good uniformity of the deposited coating, whereas the target utilization is poor since the centre and the borders are not sputtered. This is not a limit when the device is aimed at research activities, like the batch machine presented previously, where the amount of sputtered material from the same target in its whole service life is very low. The circular shape of the magnetic field is obtained by small magnets typically placed orthogonally to the target plane, meeting the reduced space due to the small target diameter, forming two concentric rings with opposite polarizations.

Completely opposite scenario is the industrial scale, where the target utilization is very important as it loads on the final cost of the deposition process. The larger size of the target makes easier the achievement of the maximization of the target utilization, also allowing the rotation of the magnet pack during the process (as done for the roll-to-roll machine described before). The optimal solution for the rotating circular magnet pack is the characteristic heart shape, see **Fig. 4.5(b)**, its analytical formula is expressed in [90]. The main limit of this analytical result is the need to reach the centre of the target, in other words, it is assumed the chance to put some magnets right in the centre, as shown in **(b)**, but this is not always possible.

The described commercial magnet pack had a central hole for the cooling water, with no chance to reach the centre, while the magnets were arranged emulating the heart shape as suggested by the optimal analytical solution, as visible in **Fig. 4.3**. Its overall performance was good for all the three parameters (uniformity of the target erosion and of the coating, and the reachable levels of low pressures), but the complexity of its maintenance procedure could be solved by proposing a novel architecture.

In **Fig. 4.5(c)**, the proposed pattern of the parallel component of the magnetic field is shown. It is a circle eccentric to the target, i.e., eccentric to the central hole of the cooling water,

with magnets arranged parallelly to the target plane. Since it is impossible to physically reach the centre, we choose to compensate by strengthening the field using bigger magnets close to the hole, as shown in (c). Simulations and experimental results validate the effectiveness of this architecture.

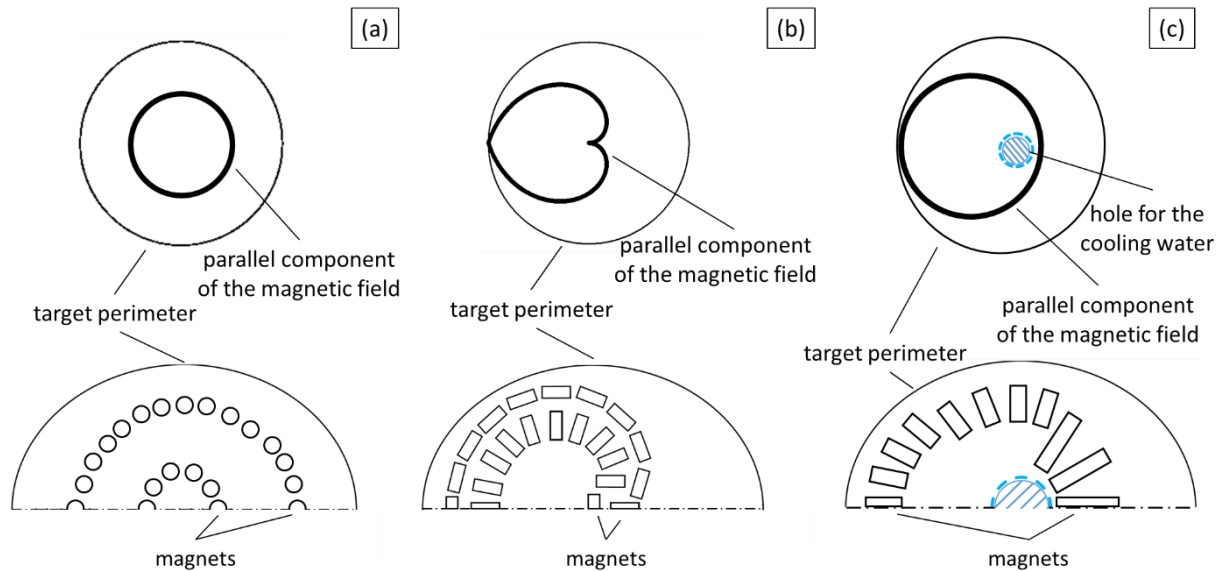


**Fig. 4.5** Positioning of the permanent magnets and patterns of the component of the magnetic field parallel to the target. (a) The optimal solution for small laboratory targets is a concentric circle. (b) Larger targets, such as for industrial applications, allows the rotation of the magnet pack and the optimal solution is a heart-shaped pattern. (c) The proposed architecture for the rotating magnet pack. Instead of trying to emulate the heart shape, the proposed pattern is a circle but eccentric with respect to the target.

The CAD of the proposed magnet pack is reported in **Fig. 4.6**. It consists of a cylindrical plastic body whose dimensions are the same of the commercial pack (diameter = 10 inches and height = 26 mm) with commercial cylindrical magnets (diameter = 9/16 inches and height 1 inch) radially arranged. The chosen material for the body is Delrin for its hardness and chemical stability in water. The radial distribution of the magnets is possible due to 24 radial holes, 12 have a length double than the others, and the long-short alternation allows the access towards the centre avoiding two adjacent holes to interfere each other, see the section view in **Fig. 4.6(c)**. The magnets closer to the centre are inserted only into the longer holes, while the adjacent stay empty. To guarantee the right positioning of the magnets, some plastic spacers are used, and their screwed axial holes are useful to ease the extraction during the maintenance procedure. The water resistance is guaranteed by 24 M20 stud screws that encapsulate each radial hole pushing a rubber o-ring, see **Fig. 4.6(d)**. The adopted permanent magnets are commercial and are made in Neodymium with N42 axial magnetization (1.32 T). They are all inserted into each hole with the same pole directed to the centre. The longer magnets close to the centre are obtained just by two magnets inserted in series, allowing the use of only one type of magnets for the whole pack. The central hole for the cooling water is round, and not pentagon like the commercial solution, with the water fluxing through a bush

with three slots at  $120^\circ$  to enhance the speed of the water for a more efficient cooling. There are six M4 holes on one of the two sides of the body, visible in **Fig. 4.6(a)**, to fasten the same support used for the commercial pack, seen previously in **Fig. 4.3(b)**.

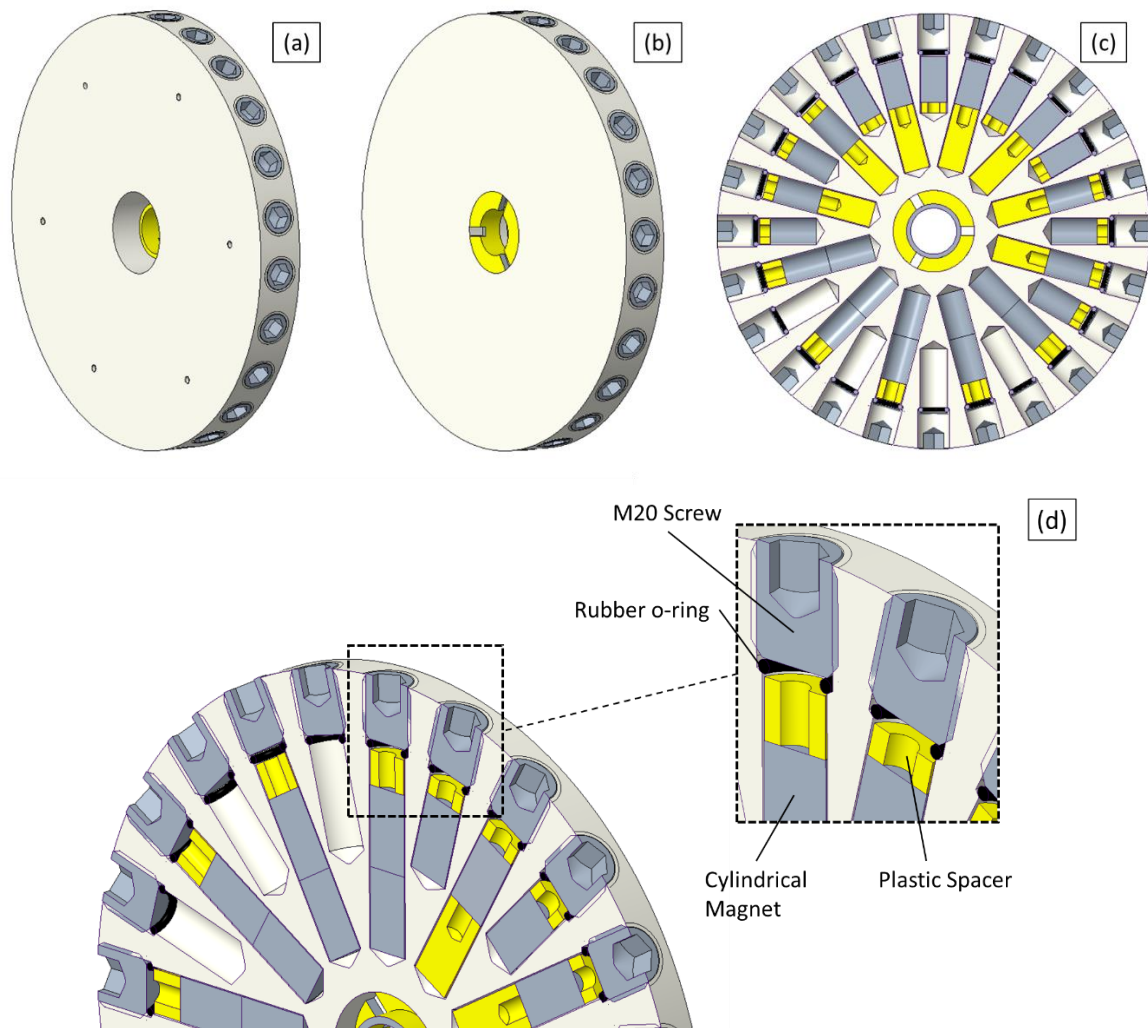


**Fig. 4.6** 3D CAD of the proposed design of the magnet pack. (a) Rear view with the six M4 holes to fasten the pack to the support already in use for the commercial device. (b) The front view of the pack. The central bush has three slots at  $120^\circ$  to allow the cooling water to distribute uniformly on the front surface. (c) The section view of the device. The magnets, the spacers and the holes are visible. (d) A detail of the proposed pack is shown. The water tightness is guaranteed by stud screws pushing rubber o-rings.

If the cooling water might reach some magnets provoking their oxidation, the maintenance procedure is very quick and easy. It is possible to realize which of the 24 holes has the water penetration by use of an external magnet, since oxidized magnets produce a smaller magnetic force. Then, the stud screw of the hole hosting the damaged magnet can be unscrewed, the magnet removed and substituted. This procedure is extremely easier and faster than that needed for the commercial pack.

To assess the shape and intensity of the magnetic field  $B$  provided by the magnets, numerical 3D simulations were performed by means of Comsol Multiphysics. In **Fig. 4.7(a)**, the geometry of the simulated 3D model is reported. Because of the intrinsic symmetry, half of the pack is representative of the whole through the boundary condition  $\nabla B = 0$ . Each cylindrical magnet has an axial magnetic flux density of 1.32 T (corresponding to the standard magnetization N42). The geometry of the simulation contains just the magnets and the surrounding space to integrate the magnetic field, any other mechanical detail is superfluous since the magnetic response of plastics and stainless-steel of the stud screws is negligible. It is worth noticing that there are three characteristic positions of the magnets. There are those inserted in series to form the longer magnets close to the central hole, and two other positions of single magnets with two different radial distances. These positions are respected by use of the proper combination of spacers (not simulated for their null magnetic response). The discretization of the 3D domain follows a regular mesh for the magnets, while the irregular shapes of the surrounding space needed the tetrahedral cells, as showed in **Fig. 4.7(b)**. The outcome of the simulation is reported in **Fig. 4.7(c)** in terms of parallel component of the magnetic flux density distribution at 40 mm of distance. As it can be seen the eccentric ring has been obtained, the two-magnets series is effective for providing the maximum intensity of the field ( $> 0.035$  T), whereas at the diametrically opposite position the field provided by the single magnet is lower (0.030 T).

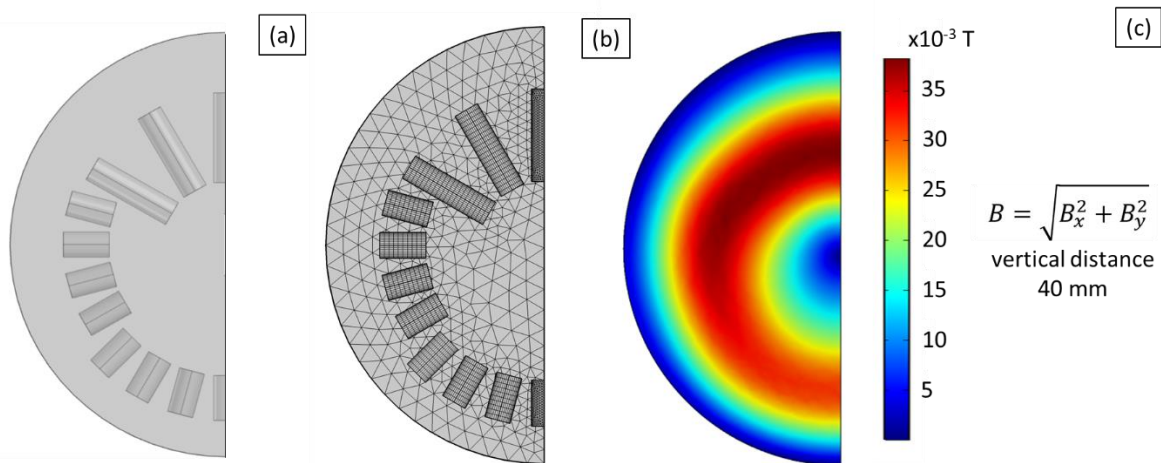


**Fig. 4.7** Numerical 3D simulations of the proposed magnet pack. (a) The symmetrical geometrical sketch considers only the magnets at three different radial distances, while neglected all the other components of the pack. (b) The discretization of the domain follows a regular mesh for the cylinders and tetrahedral for the surrounding space. (c) The numerically simulated parallel component of the magnetic field returns the eccentric ring imposed by the eccentric position of the magnets.

The simulated values of the induced magnetic field are interesting and feasible for magnetron sputtering. To better understand the quality of the proposed architecture in terms of intensity, the 3D numerical simulation is proposed also for the commercial solution. The

adopted trapezoidal magnets installed into the commercial pack are custom made and not purchasable in commerce as a standard shape. Their geometry was numerically reproduced and some of them were simulated as a portion of the whole to speed up the computational time. In addition, two symmetry planes were imposed to guarantee a conservative result in terms of field intensity. The numerical 3D model and the calculated parallel magnetic field at 40 mm of distance is reported in **Fig. 4.8** together with the simulation of the proposed solution under the hypothesis of the same magnetization grade N42 for both the types of magnets. What emerges is that the magnetic fields induced by the two solutions are comparable, around 0.030 T, with a slightly enhanced intensity for the proposed solution in correspondence of the two-series magnets.

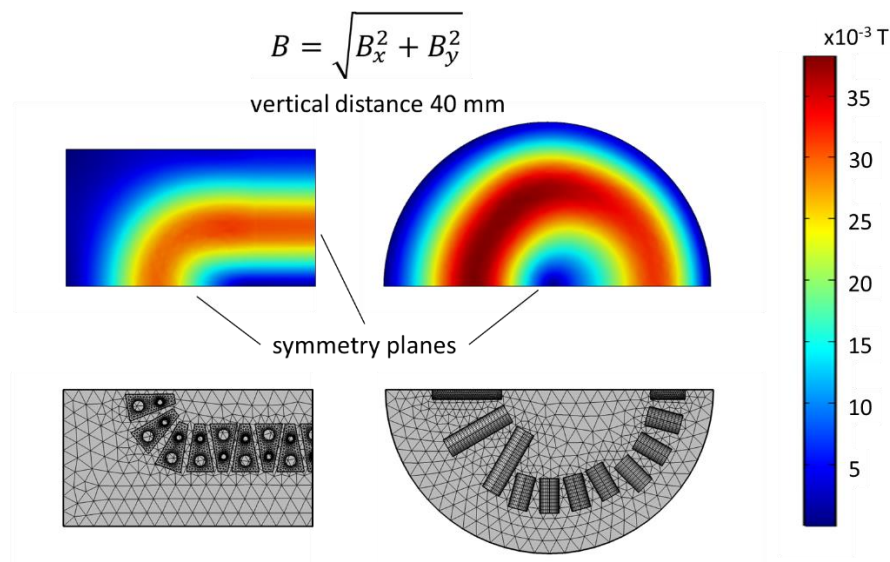


**Fig. 4.8** Comparison of the simulated parallel component of the magnetic field at 40 mm of distance for the model representative of the commercial solution (on the left) and the proposed solution (on the right) under the hypothesis of magnets with the same magnetization N42.

Once the intensity of the induced magnetic field seems to reach, or even overcome, the level of the commercial device, the analysis must focus on the target uniformity. In the following **Fig. 4.9(a)**, the erosion profile induced by the commercial pack is obtained by measurements of the valley depths on a target in advanced state of erosion. For comparison, in **Fig. 4.9(b)** there is the expected erosion by the simulation of the proposed pack. The shapes of the erosion profile are completely different, the commercial pack generates a double ring with the external deeper than the internal, while the proposed solution a single ring with intermediate diameter and a wider aperture. This result is very interesting because the proposed solution has a better target utilization, as the main issue related to the double ring of the commercial solution is the higher speed of progression of the outer valley, that makes the target no longer usable while the inner ring could still virtually continue the deposition. A single ring with a wider aperture is surely better than the two-speed double ring configuration.

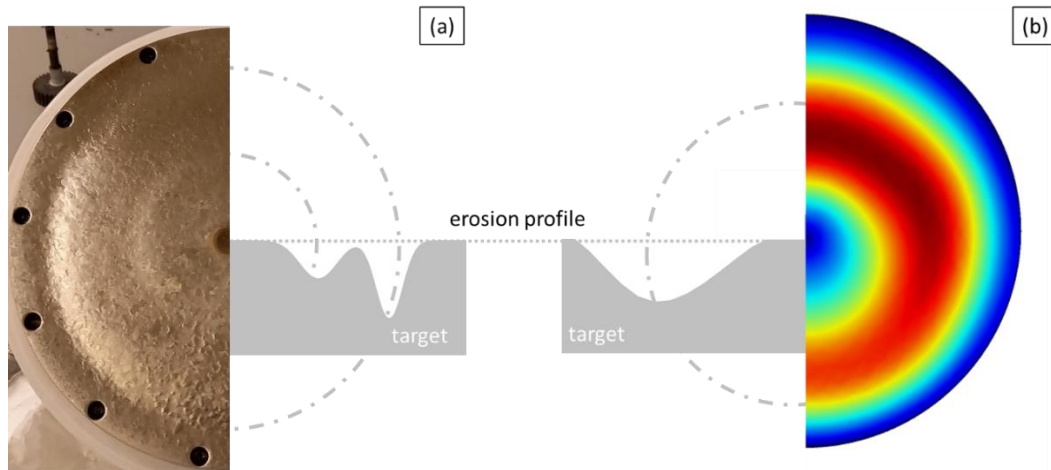


**Fig. 4.9** Target erosion profiles for the 10 inches cathode of the roll-to-roll sputtering machine. (a) The erosion profile induced by the commercial magnet pack was measured from a target with an advanced erosion state. It shows a double peak profile. (b) The simulated target erosion of the proposed magnet pack returns a better response with a single ring with wider aperture.

### 4.3. Tests of the Proposed Magnet Pack for Cr and Cr<sub>2</sub>O<sub>3</sub> Layers

The proposed magnet pack was manufactured and assembled. The radial distribution of the holes and regularity of all the geometrical details allowed the production of the body by CNC technique. In **Fig. 4.10** there are pictures of the proposed solution. The stud screws were wrapped with Teflon tape to further enhance the water resistance, see **Fig. 4.10(a)**, the commercial cylindrical magnets as arrived are shown in **(b)**. The installation was easy, and every hole was closed by its own screw, even those without magnets inside, **Fig. 4.10(c)**. Thanks to the partial transparency of plastic body, the actual position of the magnets of the assembly can be seen by use of a lamp, see **Fig. 4.10(d)**.

The next step was the experimental testing of the proposed magnet pack to qualify its performance. We conducted deposition tests in DC reactive mode of the Cr target, adopting first the commercial and then the proposed pack. In this way two goals could be achieved simultaneously, testing the novel magnet pack and verifying if stable deposition conditions could be achieved in DC reactive. Such deposition tests consisted in reproducing the characteristic oxidation curve of the Cr<sub>2</sub>O<sub>3</sub> by DC reactive sputtering, analogously to that observed with the batch laboratory machine. The oxidation curve for the batch machine consisted in the required voltage to sustain the set current at fixed Ar flow while changing progressively the O<sub>2</sub> flux from 0 sccm to the maximum, then back to zero. The resulting hysteretic behaviour of the voltage, already described in section 3.3, was useful only for its only de-oxidation phase as it generated the optimal deposition condition of Cr<sub>2</sub>O<sub>3</sub>. For this reason, the initial oxidation did not need to be progressive during the pre-sputtering process and the maximum flux of O<sub>2</sub> was immediately set, then progressively reduced to the point of interest.

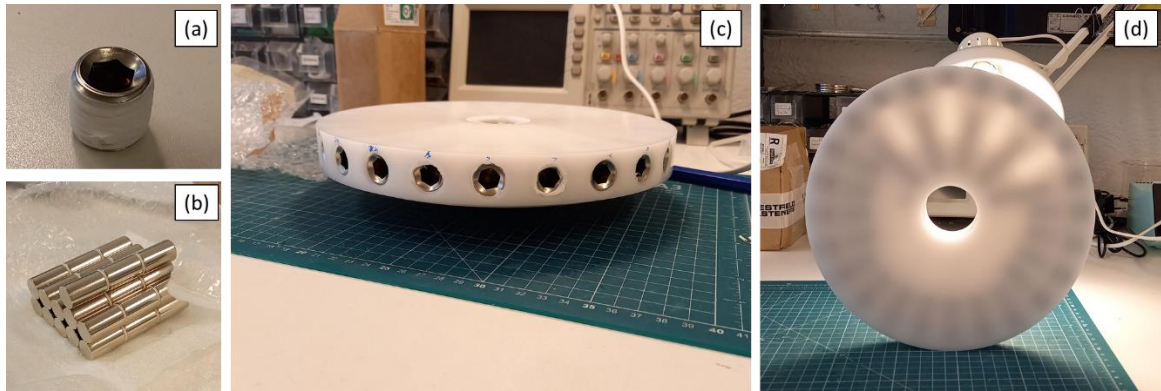


**Fig. 4.10** Pictures of the proposed magnet pack. (a) The stud screws are wrapped in Teflon tape to further improve the water resistance. (b) The cylindrical magnets as they arrived. (c) Lateral view of the mounted pack. (d) The partial transparency of the plastic body allows to see the actual position of the magnets of the assembly.

For the industrial machine the characteristic oxidation curve was obtained fixing the power instead of the current. This approach differs from the laboratory standard but leans on the fact that during industrial processes it is suggested to always control the power delivered by the supply, otherwise, in case of change of the deposition condition, the required power might rise uncontrollably. The results of the tests conducted with the two magnet packs are reported in **Fig. 4.11** for the only de-oxidation phase, showing the voltage and the pressure as function of the  $O_2$  flux at set power of 200 W and Ar flux of 40.0 sccm.

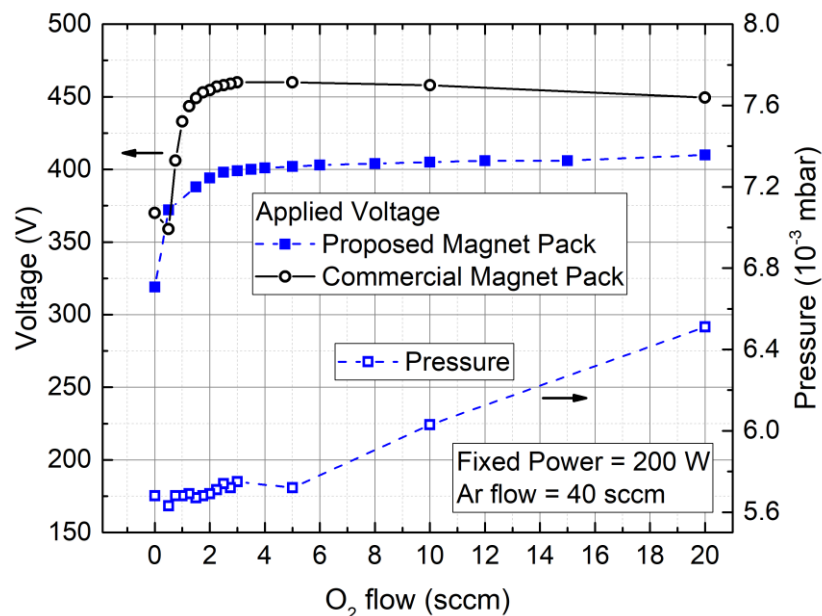


**Fig. 4.11** Characteristic de-oxidation curves of Cr during the DC reactive sputtering with the roll-to-roll industrial machine equipped with the commercial and the proposed magnet pack. The lower values of needed voltage to sustain the power of 200 W and the same optimal  $O_2$  flow of 3.0 sccm are indications of the quality of the proposed magnet pack. The provided magnetic field by the proposed solution is stronger and/or more extensive, keeping unchanged the dynamic of oxidation.

During the sputtering process, the pumping system was set with the turbomolecular pump at half of its rotational speed, as the other way (pumping through the bypass line) did not guarantee a stable process (the voltage changed continuously while fixed the other parameters). This result confirmed the known behaviour of DC reactive processes which require the highest possible pumping speed to stabilize the reactive sputtering [80]. The base pressure without any injected gas was  $5.0 \times 10^{-6}$  mbar, then the turbopump was set at its half speed of 417 Hz, the Argon flow fixed at 40 sccm and the first deposition point of the graph was for the maximum O<sub>2</sub> flow of 20 sccm. This and all the other subsequent points were the result of 2 minutes of stable deposition under constant deposition. The needed voltage to sustain the setpoint power at O<sub>2</sub> flux = 20 sccm is higher for the commercial than the proposed pack, 450 V against 409 V. The progressive reduction of the Oxygen flow to 3.0 sccm slightly changes the voltage of deposition for the proposed pack (from 409 V to 400 V) and of the commercial with an increase to 460 V. A further reduction of the O<sub>2</sub> flow provoked a rapid decrease of the voltage for both the magnet packs, and the total voltage drop was roughly of 200 V at the zero of Oxygen flow, i.e., when only Cr is deposited. The pressure response of the two processes is similar and only one of the two is reported. During the reduction of the Oxygen flow from 20 sccm to 5.0 sccm, the pressure changes linearly from  $6.5 \times 10^{-3}$  mbar to  $5.7 \times 10^{-3}$  mbar, then keeps stable at lower O<sub>2</sub> flows.

The fact that the proposed solution, under the same deposition conditions, requires a lower voltage to sustain the same power of 200 W means that the induced magnetic field is stronger and/or more extensive over the target's surface than that provided by the commercial magnet pack. The optimal O<sub>2</sub> flux to deposit the most stoichiometric Cr<sub>2</sub>O<sub>3</sub> is the last before the drop of the voltage, and it is very interesting to note that this occurred at the same value of 3.0 sccm for both magnet packs, meaning that the dynamic of the oxidation process was unchanged.

The outcome of these tests were the deposition conditions of Cr and Cr<sub>2</sub>O<sub>3</sub> for both the magnet packs. Apart from the different voltages demanded to the power supply, all the other parameters were the same, and they are reported in the following **Tab. 4.1**. The deposition of Cr, without injection of O<sub>2</sub>, was performed for a power of 100 W, half of that used for Cr<sub>2</sub>O<sub>3</sub>, because of the high deposition rate of the metal, since for preliminary tests a slower process was preferred. In table, the column of the needed voltage has two values, the first is higher than the second as they refer to the deposition by use of the commercial and the proposed magnet pack, respectively. The pressure in chamber for the Cr deposition was  $3.7 \times 10^{-3}$  mbar, lower than  $5.7 \times 10^{-3}$  mbar of Cr<sub>2</sub>O<sub>3</sub> thanks to a lower amount of injected Ar flow, 25 sccm against 40 sccm. The base pressure was  $5.0 \times 10^{-6}$  mbar, an order of magnitude higher than that read with the laboratory machine. This level of vacuum was obtained pumping the chamber from the afternoon to the next morning, analogously as the laboratory machine, but the larger extension of the industrial chamber would have needed more time to reach the same level of pressure. This difference is not relevant since the base pressure is at least three orders of magnitudes lower than the operating, meaning that during the sputtering process the dominant gas is still Argon. The deposition rates have the same magnitude of those measured with the laboratory machine, but due to completely different sizes and geometries of the components, no direct comparison can be made. The deposition rate of the metal is sensibly higher than the oxide, 18 nm/min versus 4.2 nm/min, and no difference was measurable from the use of one or the other magnet pack.

**Tab. 4.1** Deposition condition of Cr and Cr<sub>2</sub>O<sub>3</sub> for the industrial roll-to-roll sputtering machine for both the commercial and proposed magnet pack. They share all the deposition parameters but differ only for the required voltage, as the commercial pack needs an increased value.

Material	Sputtering Mode	Ar flow (sccm)	O <sub>2</sub> flow (sccm)	Pressure (mbar)	Power (W)	Voltage (V)	Dep. Rate (nm/min)
Cr	DC	25.0	0.0	$3.7 \times 10^{-3}$	100	364/313	18
Cr <sub>2</sub> O <sub>3</sub>	DC Reactive	40.0	3.0	$5.7 \times 10^{-3}$	200	460/400	4.2

Base pressure =  $5.0 \times 10^{-6}$  mbar

Assessed the deposition conditions of Cr and Cr<sub>2</sub>O<sub>3</sub>, the next step is to verify the quality of the deposited materials in terms of radiative response and uniformity over the copper substrate. Two nominally identical absorber samples were deposited, one with the commercial magnet pack and the other with the proposed solution. Then they were calorimetrically tested, and the results compared, see **Fig. 4.12**. These depositions were performed with stopped rolls to not waste meters of copper ribbon as the calorimetric test facility could host samples not larger than 140 mm × 150 mm. The deposited coating was a bilayer structure, Cr<sub>2</sub>O<sub>3</sub> – Cr over copper with thicknesses of 45 nm and 10 nm respectively. The choice to deposit only a part of full multilayer coating came from the need to emphasize any potential difference between the deposited material by the two packs, whereas the deposition of the full coating might have had an unpredicted compensation effect on the light absorptance and/or the thermal emittance due to the presence of repeated layers.

In **Fig. 4.12(a)** there is a picture of one of the deposited samples with the central and the peripheral holes for the thermocouple and for the stainless-steel springs, respectively, needed to carry the calorimetric test. Thanks to the 10 inches diameter of the target, the 10% non-uniformity was guaranteed over the demanded 140 mm × 150 mm area of copper substrate, depositing the full-sized absorber sample. The calorimetric tests were conducted indoor with the LED light power density of 1040 Wm<sup>-2</sup>, set the control voltage of 6.5 V. The resulting values of LED light absorptance  $\alpha_{LED}$  and thermal emittance  $\epsilon_{eff-TOT}$  are shown in **Fig. 4.12(b)**. The absorptances of the two samples are close, 0.915 for the commercial magnet pack and 0.938 for the proposed one, with a relative deviation of 2.5% that is in line with the reproducibility range of the calorimetric test facility. For sake of clearness of **Fig. 4.12(b)**, the thermal emittance of the sample obtained with the commercial magnet pack is reported for its fitted value  $\epsilon_{eff-FIT-TOT}$ , and the emittance  $\epsilon_{eff-TOT}$  obtained by the calorimetric equation for the other. They are in good agreement, with relative deviation of less than 2%. It is worth noticing that the reported radiative performances could suggest this bilayer absorber as candidate for our solar purpose of mid-temperature solar absorber. The not bad light absorptance, above 0.90, must be considered only for the limited visible range of the adopted LED lamps, whereas in the whole solar range its value does not reach 0.75 being not suitable for solar thermal applications.

The accordance of the radiative performances of the two samples was evidence of the positive response of the proposed magnet pack in terms of quality and uniformity of the deposited layers. Then, the lower required voltage of the novel solution suggested a magnetic field intensity higher than that provided by the commercial device. So that, the proposed pack could be used in place of the commercial for all the following tests. Contextually to those

preliminary tests, were also found stable deposition conditions of Cr and Cr<sub>2</sub>O<sub>3</sub> for the industrial machine.

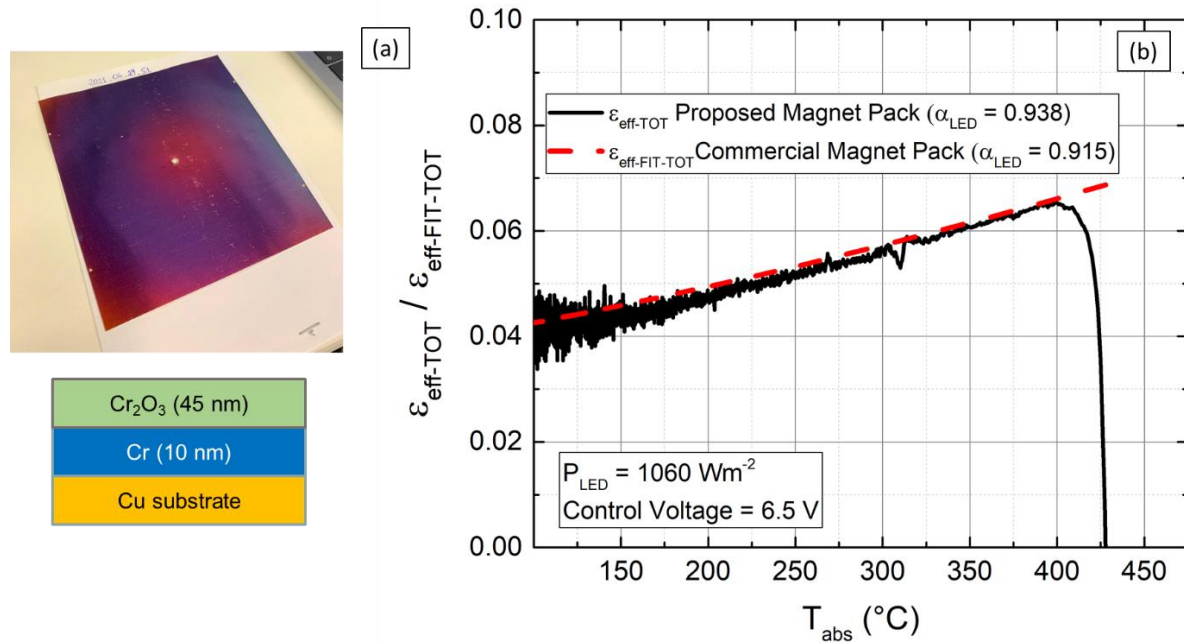


**Fig. 4.12** A bilayer coating, Cr<sub>2</sub>O<sub>3</sub> – Cr, was deposited with the roll-to-roll industrial machine over the copper substrate, once with the commercial magnet pack and then with the proposed solution. (a) A picture and the thicknesses of the 140 mm x 150 mm sample are reported. (b) The radiative properties of the two absorber samples were measured through the calorimetric test facility in indoor configuration under 1060 Wm<sup>-2</sup> of LED light power density. The accordance between the two samples validates the performance of the proposed magnet pack.

#### 4.4. SiO<sub>2</sub> Deposition: RF and DC Reactive Sputtering

The deposition of thin layers of Cr and Cr<sub>2</sub>O<sub>3</sub>, respectively via DC and DC reactive sputtering, are processes well known in literature and the conducted experimental tests demonstrated the feasibility to easily obtain Cr<sub>2</sub>O<sub>3</sub> in reactive mode even with an industrial machine. There is another known way to deposit Cr<sub>2</sub>O<sub>3</sub> by sputtering and consists of using an RF 13.56 MHz power supply starting from the Cr<sub>2</sub>O<sub>3</sub> target with no injection of O<sub>2</sub>. The main drawback of RF sputtering is the demanded electric power to sustain a certain deposition rate that is larger than the DC reactive alternative. This can be explained by the fact that, when the power supply provides an alternating potential, more energy is needed to switch the polarity, and the times when the potential applied to the target is positive are not effective to erode the target, but only to repulse the undesired positive charges from the target surface.

When the target has a good electric conductivity, it is always possible to deposit oxides by DC reactive sputtering, like metallic targets with a good reactivity to Oxygen. On the contrary, when the target has a limited electric conductivity, the RF mode is mandatory, such as the case of SiO<sub>2</sub> (top antireflective layer of the proposed coating architecture). Its DC reactive sputtering process would have the target of Si, that is a semi-conductor, sputtered

while injecting  $O_2$  into the chamber, and no trace of this kind of deposition is available in literature. In this section we want to experimentally demonstrate the feasibility to deposit  $SiO_2$  films by DC reactive sputtering, as it would give the chance to deposit the whole coating just with DC power suppliers, impacting positively on the required electrical energy and on the costs of the equipment. The tests were conducted with the roll-to-roll sputtering machine and the commercial copper foil was used as substrate. The scope was to sputter an Si target in DC reactive mode with  $O_2$  injection, then validate the quality of the deposited  $SiO_2$  film by comparison with that obtained by an  $SiO_2$  target sputtered in RF 13.56 MHz mode.

The first goal of this activity was to improve the setup of the industrial sputtering machine allowing the RF mode, since it had been designed and fully equipped only for DC sputtering. A small laboratory RF generator from Advanced Energy with a maximum power of 500 W was used, and the output RF power cable was connected the Matching Box. This device was needed to adjust the impedance of the load detected by the power supply to the setpoint value of  $50 \Omega$ , minimizing the reflected power from the target to the generator. It is composed of inductors and capacitors with variable inductance and capacitance, respectively, to match the required complex impedance of the load. An automatic controlling system adjusted the position of the armatures and/or of the solenoids in real time protecting the RF generator from overheating by the amount of reflected power. Then, the output of the matching box was an RF power cable to be connected to the target holder, and their relative position must be as close as possible to minimize the losses through the connection. From this brief description of the RF equipment, it is possible to realize the superior level of complexity of this technology when compared to the DC, justifying higher costs of almost an order of magnitude.

The second step of this activity was the supply of the target materials, Si for DC and  $SiO_2$  for RF, and their installation on the holder. In the market there are several companies selling high purity circular targets of different materials, thicknesses, and diameters for sputtering applications, and some of them provide even the service of sticking of the target over the desired holder. Unfortunately, the purchase and sticking of those targets was not compatible with the temporal extension of the activity in TVP Solar SA since the estimated delivery time of several quotations was more than 3 months. To overcome this issue, the experimental tests were conducted adopting as Si target a circular silicon wafer for electronics application of 8 inches of diameter and 1 mm of thickness, highly doped with a resistivity of  $10 \Omega\text{cm}$ , which was already available at the laboratory. As  $SiO_2$  target we used a disc of Pyrex with the same diameter and 6 mm of thickness cut out of a glass plate by a glassworker close around the TVP Solar SA laboratory. The doped silicon is an interesting alternative to traditional Si targets for sputtering applications because the introduction of controlled impurities can significantly enhance the electric conductivity, still guaranteeing the dominant presence of Si of more than 99.9%. On the other hand, Pyrex is a borosilicate glass where the  $SiO_2$  concentration is of the order of 80% and must be considered an  $SiO_2$  target with extremely low purity. Even if the adopted target were not properly designed for sputtering applications, the experimental results would reveal their effectiveness.

The next step was the sticking of the targets to the holder. In **Fig. 4.13(a)** there is the picture of the target holder with the side exposed to the vacuum tilted upward. To guarantee the proper sticking over the bare copper surface of the holder, the Indium/Gallium alloy was adopted. It is the perfect solution for this kind of application because at room temperature it is liquid, very low degassing in high-vacuum, and, being a metal, its surface tension, thermal and electrical conductivity are extremely high. The In/Ga alloy was put and spread over the target holder covering a central circle of 8 inches, leaving uncovered the remaining holder

surface (being designed to host targets of 10 inches), see **Fig. 4.13(b)**. Then the target was attached to the holder and a custom-made Teflon ring was installed, **Fig. 4.13(c)**, to keep the target always centred, cutting out any transversal motion, and shielding the bare part of the holder from the  $\text{Ar}^+$  ion current.

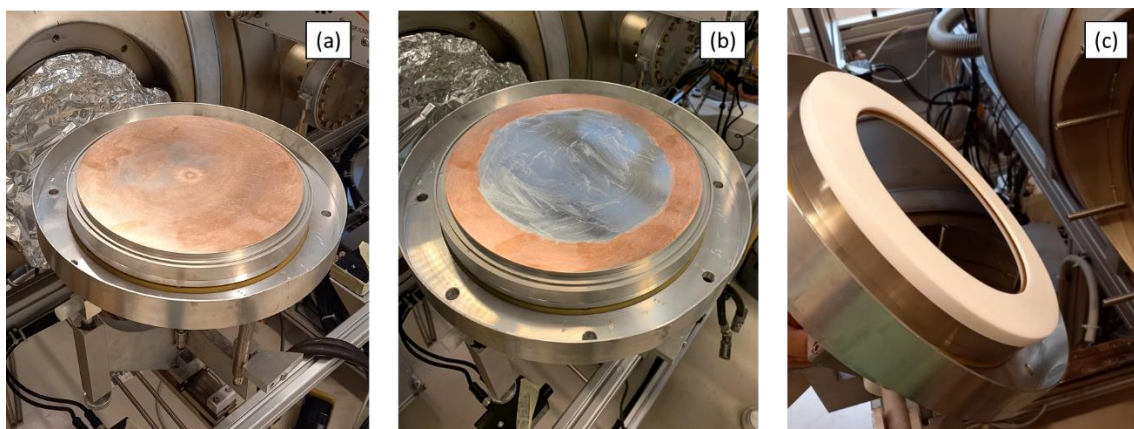


**Fig. 4.13** Pictures of the target holder during the sticking procedure with In/Ga alloy used for the silicon wafer and fused silica glass discs adopted as target. (a) The bare copper holder put upwards. (b) In/Ga is spread over the holder for a diameter of 8 inches. (c) The silicon wafer is mounted, and a custom-made Teflon ring was used to shield the bare surface of the holder and to avoid any translational motion of the target along the vertical direction.

Once the mounting procedure of the targets was proved to be effective, deposition tests were performed by use of the proposed magnet pack, DC reactive for the silicon wafer and RF 13.56 MHz for Pyrex. First, we started with the DC reactive sputtering of Si, and its characteristic oxidation curves are reported **Fig. 4.14(a)** and **(b)** where each point of the graphs corresponds to 2 minutes of stable deposition. The difference between these graphs is the volumetric flow rate of the pumping system. As explained previously, the roll-to-roll machine had two possible modes for the pumping system, one is pumping through the bypass line **(a)** reducing the flow rate of an order of magnitude, the other is pumping through the main gate with the turbomolecular pump at half speed **(b)**. In both cases, the introduction of injected gases would not overload the turbopump.

Contrarily to what happened for the Cr target, the Si experienced a DC reactive process steady even with the chamber evacuated through the bypass pipeline, **Fig. 4.14(a)**. The power was fixed at 100 W and, to keep the needed voltage around 500 V, the Ar flow was set 8.0 sccm obtaining an operating pressure as high as  $1.8 \times 10^{-2}$  mbar. This pressure is sensibly higher than that used for the Cr and  $\text{Cr}_2\text{O}_3$ , roughly  $5 \times 10^{-3}$  mbar, being evidence of the limits of the ionization process when the target is not as conductive as a metal. The increase of the  $\text{O}_2$  flow up to the maximum of 20 sccm, then the decrease back to zero return always a linear variation of the pressure and no hysteretic behaviour can be observed. The voltage has a similar linear response and none of the typical hysteretic features of the DC reactive sputtering could be detected.

Repeating the same test but with the turbopump at half speed, the experimental points are reported in **Fig. 4.14(b)** for the same fixed power of 100 W and Ar flow set 100 sccm. Such a high value of flux was needed to guarantee an operating pressure high enough to keep the

maximum voltage not exceeding 500 V. The first point of the test was null O<sub>2</sub> flow and 466 V of needed potential, then with the increase of the Oxygen flow, the voltage had a decrease to 440 V for 2.0 sccm. A further increase of the O<sub>2</sub> flow produced the rise of the voltage up to the maximum value of 500 V is at 20 sccm. The reduction of the reactive flux did not change the response of the deposition, keeping constant the needed voltage up to 5 sccm, where a slight decrease was observed. With the reduction of the flux from 5.0 sccm to 1.0 sccm there was a progressive decrease of the voltage to 490 V. The total removal of the reactive flow showed an unexpected instability of the plasma, and no steady points could be observed (not reported in figure). The pressure changed linearly with the O<sub>2</sub> flux, but the slope of the decrease is slightly lower than the increase. The points at 1.0 sccm had pressures of  $1.85 \times 10^{-2}$  mbar and  $1.93 \times 10^{-2}$  mbar at the oxidation and de-oxidation phases, respectively. This difference was of the order of  $10^{-3}$  mbar, being significant and not negligible.

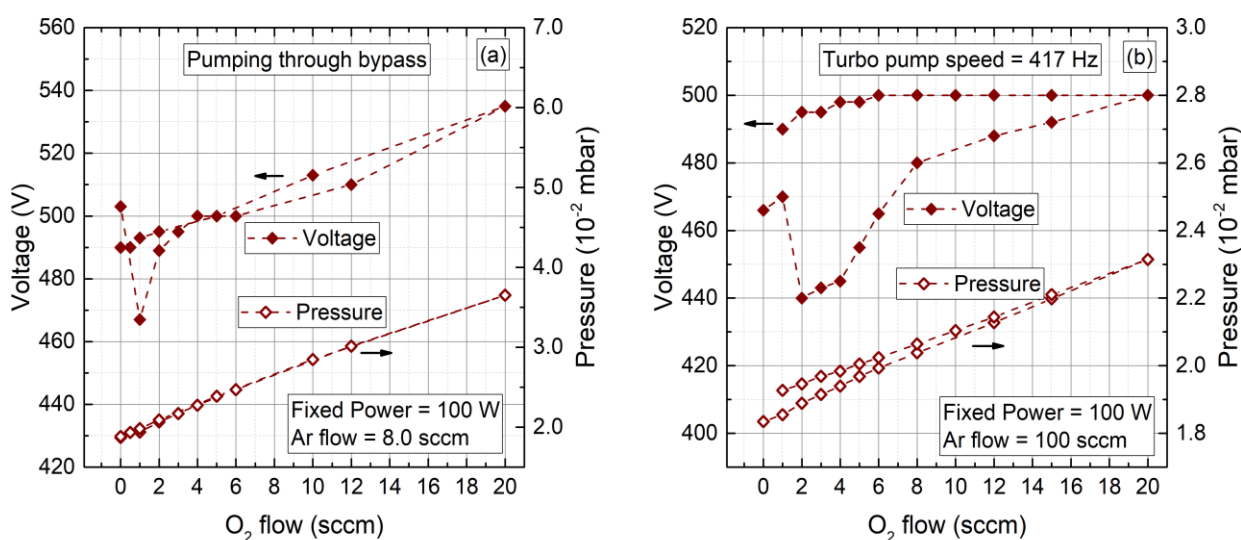


**Fig. 4.14** Oxidation curves of the Si target during DC reactive sputtering with O<sub>2</sub> injection in chamber for a set power of 100 W. The values of pressure are higher than those used for the Cr<sub>2</sub>O<sub>3</sub>, roughly one order of magnitude, to limit the maximum value of the applied voltage around 500 V. (a) Oxidation curve when the chamber is evacuated through the bypass line. (b) Oxidation curve when the evacuation is performed through the main gate with the turbopump at half speed.

The hysteretic behaviour of the voltage in **Fig. 4.14(b)** had features similar to those seen during the Cr<sub>2</sub>O<sub>3</sub> in DC reactive sputtering, and because of this, the optimal deposition condition of SiO<sub>2</sub> in DC reactive mode must be chosen among those points. In literature there was no data about hysteretic response of the Si oxidation during DC reactive sputtering, so nothing was known about the stoichiometry of the deposited oxide in each of the points of **Fig. 4.14(b)**. For the Cr<sub>2</sub>O<sub>3</sub> in DC reactive mode, it was known that stoichiometry was reached by the point of the de-oxidation phase that anticipated the fast drop of the voltage, but unfortunately, for the Si target there was just a slight decrease of voltage from 500 V to 490 V, then followed by an unexpected unsteady deposition condition of the bare Si with no O<sub>2</sub> flow. At this point, the only information we could use was the O<sub>2</sub> flux for the stoichiometric Cr<sub>2</sub>O<sub>3</sub>, 3.0 sccm, and it was chosen as first guess point to test the deposited Silicon Oxide. The related

deposition condition is summarized in **Tab. 4.2**, and a deposition rate of 2.4 nm/min was measured.

The other parallel test, RF sputtering of the Pyrex target, was carried out with the chamber evacuated through the bypass, since the dominant parameter for this process is only the Ar pressure and, thanks to a minimized pumping rate, the required Ar flow injected in chamber was minimal. In the **Tab. 4.2** are reported details of the RF deposition too. The needed Ar flow to guarantee a pressure of  $8.78 \times 10^{-3}$  mbar was just 3.0 sccm and the power was set to 400 W to return the same deposition rate of 2.4 nm/min of the DC reactive mode. This is the experimental evidence that the RF sputtering deposition is less efficient than the DC reactive sputtering, because to sustain the same deposition rate, the required power for the RF power supply is four times bigger.

**Tab. 4.2** Deposition parameters for the roll-to-roll industrial machine of the SiO<sub>2</sub> film obtained by DC reactive sputtering (Si target + O<sub>2</sub> injection) and RF 13.56 MHz sputtering of the Pyrex target.

Material	Sputtering Mode	Ar flow (sccm)	O <sub>2</sub> flow (sccm)	Pressure (mbar)	Power (W)	Voltage (V)	Dep. Rate (nm/min)
SiO <sub>2</sub>	DC Reactive	100	3.0	$1.97 \times 10^{-2}$	100	490	2.4
SiO <sub>2</sub>	RF 13.56 MHz	3.0	0.0	$8.78 \times 10^{-3}$	400	N.A.	2.4

Base pressure =  $5.0 \times 10^{-6}$  mbar

The adopted experimental procedure to qualify the SiO<sub>2</sub> layer deposited by DC reactive sputtering from the Si target consisted of depositing some mono-layer samples of SiO<sub>2</sub>, or presumed, over copper substrate to be calorimetrically tested indoor. The resulting LED light absorptance was compared to that obtained by similar mono-layer samples of SiO<sub>2</sub> by RF deposition over copper. In other words, the adopted parameter used to quantitatively define the quality of the deposited SiO<sub>2</sub> was the LED light absorptance of a single layer over the copper substrate, and the samples made by RF deposition were our reference benchmarks.

At this stage, we did not know what SiO<sub>2</sub> thickness would have maximized the change of absorptance into the LED spectrum, and, in order to minimize the number of deposited and calorimetrically tested samples, a series of simulations was conducted in advance. IMD [91] is a software that simulates 1-D optical structures starting from the refractive index, extinction coefficient and thicknesses of each material composing the sequence and returns the spectral emissivity into the wavelength range of interest. The spectral emissivity of several mono-layer structures was simulated into the LED wavelength interval and the expected absorptance was integrated through eq. 1.9. The simulated SiO<sub>2</sub> thickness ranged from 0 nm (not coated copper) to 150 nm, while the substrate was a copper layer of 0.20 mm. Refractive indices and extinction coefficients were taken from literature, Gao et al. (2012) for the SiO<sub>2</sub> [73] and Ordal et al. (1985) for Cu [77]. The outcome of the numerical simulations was the LED light absorptance  $\alpha_{LED}$  function of the thickness of the SiO<sub>2</sub> top layer over copper, see **Fig. 4.15**.

Since the SiO<sub>2</sub> deposited by DC reactive sputtering could not have been stoichiometric, potentially SiO<sub>x</sub> due to vacancy of Oxygen, in the same figure together with the simulations of SiO<sub>2</sub> there are also those with SiO and Si over the copper substrate. Their refractive indices and extinction coefficients referred to literature, SiO from [92, p. 19] and Si from [93].

The simulated  $\alpha_{LED}$  for the bare copper, i.e., for 0 nm of top layer, is 0.323 and it is in perfect accordance with the calorimetric measurement of the bare substrate reported previously in Fig. 3.7(c). All the three curves start from that value of simulated  $\alpha_{LED}$  but have three completely different trends and values when the thickness of the top layer increases. The SiO<sub>2</sub> layer would increase  $\alpha_{LED}$  from 0.323 up to 0.492 for a thickness of 59 nm and any thinner or thicker layer would reduce it. This was promising because that value of thickness is perfectly compatible to our deposition setup and the change of LED light absorptance is sensible and could be effectively measured with the calorimetric test facility. For the other materials, SiO and Si, there is an increase of  $\alpha_{LED}$  too, but it occurs to different thicknesses and higher values than SiO<sub>2</sub>. Indeed, Si reaches a narrow maximum of 0.855 at 12 nm of thickness, but at 40 nm  $\alpha_{LED}$  reduces with almost unchanged value with respect to the bare copper. At 78 nm there is a secondary maximum of 0.634, and a secondary minimum at 120 nm of 0.558. On the contrary, SiO has a different response with a maximum at 40 nm of 0.641 which slightly reduces to 0.615 up to 150 nm. The optical simulations of SiO<sub>2</sub> over copper revealed that tens of nanometres are enough to experimentally observe a substantial increase of the LED light absorptance during the calorimetric tests. The simulations of SiO and Si over copper confirmed that, if the DC reactive sputtering had deposited silicon not fully oxidated, it was calorimetrically measurable.

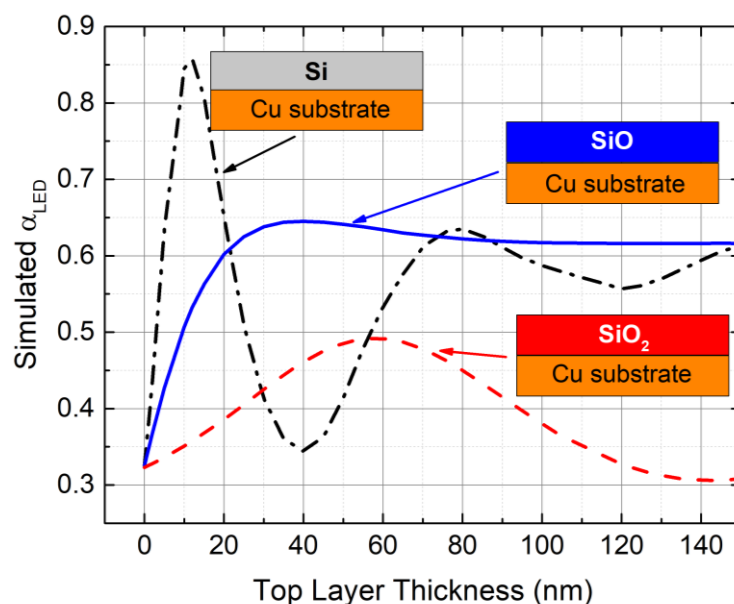


**Fig. 4.15** Simulated LED light absorptance  $\alpha_{LED}$  of single layers of Si, SiO and SiO<sub>2</sub> over the copper substrate as function of the thickness. These simulations were performed thanks to a 1-D software [91] that returns the spectral emissivity curve of multi-layered structures starting from refractive indices, extinction coefficients and thicknesses of the sequence. Then, thanks to eq. 1.9,  $\alpha_{LED}$  was calculated over the spectrum of the LEDs used for the solar simulator of the calorimetric facility. The three curves are completely different, and the calorimetric tests is enough to qualify the deposited silicon oxide by DC reactive sputtering.

We deposited four samples with the DC reactive process (thicknesses 30 nm, 50 nm, 67 nm, and 90 nm) and three with the RF (thicknesses 28 nm, 57 nm, and 86 nm), then cut 140

mm x 150 mm samples to be calorimetrically tested indoor. In **Fig. 4.16** the experimental  $\alpha_{LED}$  of the deposited samples are compared to the simulations. The point at 0 nm referred to the test of the bare copper and it matched the simulations with a deviation below 1%. With the increase of the deposited thickness, the experimental points followed the SiO<sub>2</sub> simulation with a deviation below 2% for both DC and RF sputtering (apart from the sample deposited in RF with thickness of 86 nm, its deviation was 5%). These results confirmed the good quality of the deposited SiO<sub>2</sub> in DC reactive mode, since it behaved like that obtained by the traditional RF process, that in turn corresponded to simulations based on optical properties of the materials of literature.

This means that our guess of O<sub>2</sub> flux equal to 3.0 sccm was right to deposit stoichiometric SiO<sub>2</sub> by DC reactive sputtering from the Si target. The lack of additional experimental data would limit the effectiveness of this deposition recipe only to this industrial machine, and no general correlation could be extrapolated. Even if we do not have yet a general rule to describe this kind of deposition, we proved that there is at least one stable condition for a good quality SiO<sub>2</sub> by use of DC reactive sputtering.

In addition, the target used to deposit SiO<sub>2</sub> in RF was a Pyrex glass and surely it could be classified as a low purity target for sputtering depositions (purity of 80% against a value of more than 98.0% for commercial SiO<sub>2</sub> targets available in the market). The fact that there is accordance between experimental and simulated  $\alpha_{LED}$  is interesting, meaning that high purity of the target is not mandatory for this kind of applications, explaining eventually the slightly bigger deviation from the simulation of the thickest sample made in RF mode.

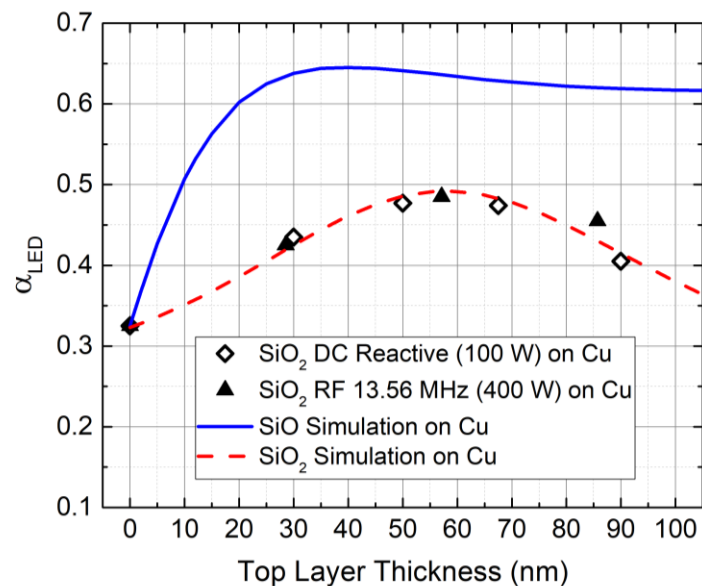


**Fig. 4.16** Simulated LED light absorptance of single layer samples over copper substrates of SiO and SiO<sub>2</sub> are compared to calorimetric experimental results of SiO<sub>2</sub> deposited over the copper foil by both DC reactive and RF sputtering. The good accordance between the experimental data with the numerical results confirms the success of the deposition of SiO<sub>2</sub> via DC reactive sputtering starting from the Si target while injecting O<sub>2</sub> into the chamber during the process.

## Conclusion

The evacuated flat panel for solar thermal applications working unconcentrated under high-vacuum insulation (pressure below  $10^{-4}$  mbar) is the new frontier to renewably produce industrial process heat in the mid-temperature range  $100\text{ }^{\circ}\text{C} - 200\text{ }^{\circ}\text{C}$ . The annual demand for heat in this specific interval is substantial and reaches 21% of the total produced industrial heat and cooling in Europe. The evacuated flat panel overcomes all the limits typical of concentrated tube receivers, such as the need for solar tracking, large acceptance angle of the light, and higher fill fraction of the net absorbing surface. It returns unrivalled conversion efficiency at mid-temperatures, but a sensible improvement could be achieved if the proper absorber was adopted. The high vacuum insulation cuts out even the conduction contribution of the internal air, bringing the main mechanism of thermal loss to the radiative emission of the absorber. This completely changes the demanded absorber's features, as thermal emittance becomes the new key parameter controlling the panel efficiency.

TVP Solar SA is the only company still active producing commercial high-vacuum unconcentrated flat panels designed to operate at mid-temperature applications. Due to the lack of availability of commercial absorbers properly designed, such collectors are equipped with the same absorbers adopted to operate at low temperatures (below  $100\text{ }^{\circ}\text{C}$ ). The aim of this work was producing a novel absorber to better match the requirements of this relatively new solar receiver, resulting in a sensible improvement of the performance.

The first challenge of the activity was the reliable measurement of the radiative properties of the absorber, since the optical analysis of reflectivity is commonly conducted at room temperature and pressure, whereas the real operation is under high vacuum and at temperatures up to  $200\text{ }^{\circ}\text{C}$ , potentially returning a different radiative response. A novel calorimetric test facility was designed to measure the radiative properties of the absorber reproducing the real operating conditions of the evacuated flat panel. It consisted in a panel-like vacuum chamber with the absorber heated by the exposure to the solar irradiation (outdoor testing configuration) or to the LED based solar simulator properly designed for the scope (indoor testing configuration). Calorimetric tests were conducted to assess the radiative properties of the absorber, and discrepancies on the thermal emittance with respect to the optical response were observed only at temperatures above  $150\text{ }^{\circ}\text{C}$ , reaching +9% at  $300\text{ }^{\circ}\text{C}$ . On the other hand, the optical emittances corrected by the analytical model of infinite parallel plates, to simulate the interaction with glass and vessel, underestimated the emittance over all the investigated temperature range, with -11% below  $100\text{ }^{\circ}\text{C}$  and reduced to -8% at  $300\text{ }^{\circ}\text{C}$ . Good agreement was found between the calorimetrically measured solar and LED light absorptance, respectively during outdoor and indoor tests, with those measured optically within a deviation of the order of 2%.

Once a reliable measurement procedure of the radiative properties was established, the activity moved to the production of the novel absorber. The chosen architecture was the multi-layered coating of nanometric films deposited via Magnetron Sputtering over a commercial copper substrate. This solution is perfectly in line with the current industrial production of commercial low-T absorbers. The adopted multilayer was Chromium based with the alternation of the metal and its  $\text{Cr}_2\text{O}_3$  oxide with a top antireflective layer of  $\text{SiO}_2$ . Three multilayers with the same sequence of materials but with different thicknesses were selected to be deposited. The decrease of the thicknesses from absorber #3 to #1 was expected to slightly reduce solar absorptance in favour of a strong reduction of thermal emittance. They were

produced with a laboratory sputtering machine, then calorimetric and optical tests confirmed the expected trend of radiative properties with the deposited thicknesses, such as solar radiation absorptance of 0.950, 0.924, 0.890, and total thermal emittance at 200 °C of 0.137, 0.095, 0.075 respectively for absorbers #1, #2, and #3, against absorptance of 0.933 and emittance of 0.107 of the commercial absorber used as benchmark. Simulations of the annual efficiency of the TVP Solar SA panel mounted in a city with medium solar irradiation (Naples, Italy) showed the benefit of employing absorber #2 and #3 in the mid-temperature range, whereas absorber #1 was not suited for this application. The benefit of using absorber #2 in place of the adopted commercial for the 100 °C – 150 °C range was minimal (of the order of 2%), while absorber #3 showed a substantial increase of the annual efficiency of +5% at 150 °C and +25% at 200 °C of operating temperature.

During my experience abroad at TVP Solar SA laboratories in Geneva (Switzerland), deposition tests of the materials of interest were conducted with an industrial roll-to-roll sputtering machine. Cr and Cr<sub>2</sub>O<sub>3</sub> were deposited through Direct Current processes starting from the Cr target, the second with additional injection of O<sub>2</sub> into the chamber, as done with the small-scale laboratory machine. The top SiO<sub>2</sub> antireflective layer was deposited both by Radio Frequency 13.56 MHz sputtering from the SiO<sub>2</sub> target and by Direct Current from the Si target coupled to the O<sub>2</sub> injection. It was demonstrated the chance to deposit the whole coating structure by means of DC power supply, which proved to be more energetically efficient and cost effective than the RF alternative. Part of the activity was the design of a novel magnet pack for the industrial sputtering machine. An innovative geometry of the parallel component of the induced magnetic field was introduced, overcoming all the maintenance limits of the commercial alternative. Experimental sputtering tests validated the simulated performances and qualified its use in place of the commercial device.

The research activity reported in this thesis has interesting future developments. One is to overcome the need for the industrial copper substrate, substituting it with any other cheaper metallic substrate (such as aluminium) thanks to the deposition of a thick film of copper. A thickness above 150 nm of copper on both sides of the coil before the deposition of the absorbing multilayer coating has a positive impact on costs with no difference in terms of performance. The designing of a proper diffusion barrier to limit the inter-diffusion mechanisms is needed, being the core of the novel development. The possibility to adopt any kind of substrate makes the proposed multilayer coating even more appealing and versatile. The other future activity is to test the full scale evacuated panel equipped with the proposed absorber under controlled boundary conditions to assess the novel formulation of the overall panel efficiency. Contextually, an innovative procedure to test flat plate evacuated panels would be established as the current international methodology is not suited for evacuated devices due to the limited temperature of the tests.

## Bibliography

- [1] Heat Roadmap Europe 4, 'Heating and Cooling: facts and figures. The transformation towards a low-carbon Heating & Cooling sector.', 2017. Accessed: Sep. 05, 2021. [Online]. Available: <https://www.euroheat.org/publications/heating-cooling-facts-figures/>
- [2] S. H. Farjana, N. Huda, M. A. P. Mahmud, and R. Saidur, 'Solar process heat in industrial systems – A global review', *Renewable and Sustainable Energy Reviews*, vol. 82, pp. 2270–2286, Feb. 2018, doi: 10.1016/j.rser.2017.08.065.
- [3] S. Gorjian, H. Ebadi, F. Calise, A. Shukla, and C. Ingraio, 'A review on recent advancements in performance enhancement techniques for low-temperature solar collectors', *Energy Conversion and Management*, vol. 222, p. 113246, Oct. 2020, doi: 10.1016/j.enconman.2020.113246.
- [4] V. Pranesh, R. Velraj, S. Christopher, and V. Kumaresan, 'A 50 year review of basic and applied research in compound parabolic concentrating solar thermal collector for domestic and industrial applications', *Solar Energy*, vol. 187, pp. 293–340, Jul. 2019, doi: 10.1016/j.solener.2019.04.056.
- [5] C. B. Eaton and H. A. Blum, 'The use of moderate vacuum environments as a means of increasing the collection efficiencies and operating temperatures of flat-plate solar collectors', *Solar Energy*, vol. 17, no. 3, pp. 151–158, Jul. 1975, doi: 10.1016/0038-092X(75)90053-5.
- [6] N. Benz and T. Beikircher, 'High efficiency evacuated flat-plate solar collector for process steam production', *Fuel and Energy Abstracts*, vol. 40, no. 5, p. 342, Sep. 1999, doi: 10.1016/S0140-6701(99)91217-1.
- [7] R. Moss, S. Shire, P. Henshall, F. Arya, P. Eames, and T. Hyde, 'Performance of evacuated flat plate solar thermal collectors', *Thermal Science and Engineering Progress*, vol. 8, pp. 296–306, Dec. 2018, doi: 10.1016/j.tsep.2018.09.003.
- [8] C. Benvenuti, 'The SRB solar thermal panel', *Europhysics News*, vol. 44, no. 3, pp. 16–18, May 2013, doi: 10.1051/epn/2013301.
- [9] TVP Solar SA, 'MT-Power: Thermal Applications 100°C To 180°C', 2017. Accessed: Aug. 19, 2021. [Online]. Available: <https://www.tvpsolar.com/products.html>
- [10] D. Gao *et al.*, 'Experimental and numerical analysis of an efficiently optimized evacuated flat plate solar collector under medium temperature', *Applied Energy*, vol. 269, p. 115129, Jul. 2020, doi: 10.1016/j.apenergy.2020.115129.
- [11] Alanod, 'Alanod Surfaces - Mirotherm', *www.alanod.com*, 2021. <https://alanod.com/en/products/our-surfaces> (accessed Apr. 02, 2021).
- [12] F. Arya, R. Moss, T. Hyde, S. Shire, P. Henshall, and P. Eames, 'Vacuum enclosures for solar thermal panels Part 1: Fabrication and hot-box testing', *Solar Energy*, vol. 174, pp. 1212–1223, Nov. 2018, doi: 10.1016/j.solener.2018.10.064.
- [13] R. W. Moss, P. Henshall, F. Arya, G. S. F. Shire, P. C. Eames, and T. Hyde, 'Simulator testing of evacuated flat plate solar collectors for industrial heat and building integration', *Solar Energy*, vol. 164, pp. 109–118, Apr. 2018, doi: 10.1016/j.solener.2018.02.004.
- [14] Y. Fang, F. Arya, T. J. Hyde, and N. Hewitt, 'A Novel Building Component Hybrid Vacuum Glazing – A Modelling And Experimental Validation', vol. 119, p. 13, 2013.

- [15] F. Arya *et al.*, 'Fabrication analysis of flat vacuum enclosures for solar collectors sealed with Cerasolzer 217', *Solar Energy*, vol. 220, pp. 635–649, May 2021, doi: 10.1016/j.solener.2021.02.040.
- [16] Z. Wang, Z. Gao, J. Chu, D. Qiu, and J. Niu, 'Low Temperature Sealing Process and Properties of Kovar Alloy to DM305 Electronic Glass', *Metals*, vol. 10, no. 7, p. 941, Jul. 2020, doi: 10.3390/met10070941.
- [17] V. Palmieri, 'Vacuum Solar Thermal Panel', USOO81 6 1965B2, 2012
- [18] J. Jeans, *An Introduction to the Kinetic Theory of Gases*, 1st ed. Cambridge University Press, 1982. doi: 10.1017/CBO9780511628849.
- [19] S. Dushman, Research Staff of General Electric Research Laboratory, and S. C. Brown, 'Scientific Foundations of Vacuum Technique', *American Journal of Physics*, 1949.
- [20] T. Beikircher, N. Benz, and W. Spirkl, 'Gas Heat Conduction in Evacuated Flat-Plate Solar Collectors: Analysis and Reduction', *Journal of Solar Energy Engineering*, vol. 117, no. 3, pp. 229–235, Aug. 1995, doi: 10.1115/1.2847807.
- [21] S. A. Sakhaei and M. S. Valipour, 'Performance enhancement analysis of The flat plate collectors: A comprehensive review', *Renewable and Sustainable Energy Reviews*, vol. 102, pp. 186–204, Mar. 2019, doi: 10.1016/j.rser.2018.11.014.
- [22] B. Liu *et al.*, 'Optical properties and thermal stability evaluation of solar absorbers enhanced by nanostructured selective coating films', *Powder Technology*, vol. 377, pp. 939–957, Jan. 2021, doi: 10.1016/j.powtec.2020.09.040.
- [23] K. Xu, M. Du, L. Hao, J. Mi, Q. Yu, and S. Li, 'A review of high-temperature selective absorbing coatings for solar thermal applications', *Journal of Materiomics*, vol. 6, no. 1, pp. 167–182, Mar. 2020, doi: 10.1016/j.jmat.2019.12.012.
- [24] Almeco Group, 'Almeco', *www.almecogroup.com*, 2021. *www.almecogroup.com* (accessed Sep. 10, 2021).
- [25] F. Cao, K. McEnaney, G. Chen, and Z. Ren, 'A review of cermet-based spectrally selective solar absorbers', *Energy Environ. Sci.*, vol. 7, no. 5, p. 1615, 2014, doi: 10.1039/c3ee43825b.
- [26] M. Bello and S. Shanmugan, 'Achievements in mid and high-temperature selective absorber coatings by physical vapor deposition (PVD) for solar thermal Application-A review', *Journal of Alloys and Compounds*, vol. 839, p. 155510, Oct. 2020, doi: 10.1016/j.jallcom.2020.155510.
- [27] P. Bermel, J. Lee, J. D. Joannopoulos, I. Celanovic, and M. Soljacic, 'SELECTIVE SOLAR ABSORBERS', *Annual Rev Heat Transfer*, vol. 15, no. 15, pp. 231–254, 2012, doi: 10.1615/AnnualRevHeatTransfer.2012004119.
- [28] Ocean Optics, 'Ocean Insight', *www.oceaninsight.com*, 2021. *www.oceaninsight.com* (accessed Sep. 14, 2021).
- [29] K. Zhang, Y. Zhao, K. Yu, and Y. Liu, 'Development of experimental apparatus for precise emissivity determination based on the improved method compensating disturbances by background radiation', *Infrared Physics & Technology*, vol. 92, pp. 350–357, Aug. 2018, doi: 10.1016/j.infrared.2018.06.031.
- [30] L. Mercatelli, M. Meucci, and E. Sani, 'Facility for assessing spectral normal emittance of solid materials at high temperature', *Appl. Opt.*, vol. 54, no. 29, p. 8700, Oct. 2015, doi: 10.1364/AO.54.008700.
- [31] T. Echániz, I. Setién-Fernández, R. B. Pérez-Sáez, C. Prieto, R. E. Galindo, and M. J. Tello, 'Importance of the spectral emissivity measurements at working temperature to determine the efficiency of a solar selective coating', *Solar Energy Materials and Solar Cells*, vol. 140, pp. 249–252, Sep. 2015, doi: 10.1016/j.solmat.2015.04.009.

- [32] J. Jyothi, A. Soum-Glaude, H. S. Nagaraja, and H. C. Barshilia, 'Measurement of high temperature emissivity and photothermal conversion efficiency of TiAlC/TiAlCN/TiAlSiCN/TiAlSiCO/TiAlSiO spectrally selective coating', *Solar Energy Materials and Solar Cells*, vol. 171, pp. 123–130, Nov. 2017, doi: 10.1016/j.solmat.2017.06.057.
- [33] K. Niranjana, A. Soum-Glaude, A. Carling-Plaza, S. Bysakh, S. John, and H. C. Barshilia, 'Extremely high temperature stable nanometric scale multilayer spectrally selective absorber coating: Emissivity measurements at elevated temperatures and a comprehensive study on ageing mechanism', *Solar Energy Materials and Solar Cells*, vol. 221, p. 110905, Mar. 2021, doi: 10.1016/j.solmat.2020.110905.
- [34] J. R. Howell, M. P. Mengüç, K. J. Daun, and R. Siegel, *Thermal radiation heat transfer*, Seventh edition. Boca Raton: CRC Press / Taylor & Francis Group, 2021.
- [35] H. Willrath and R. B. Gammon, 'The measurement of optical properties of selective surfaces using a solar calorimeter', *Solar Energy*, vol. 21, no. 3, pp. 193–199, 1978, doi: 10.1016/0038-092X(78)90021-X.
- [36] D. Kraemer, K. McEnaney, F. Cao, Z. Ren, and G. Chen, 'Accurate determination of the total hemispherical emittance and solar absorptance of opaque surfaces at elevated temperatures', *Solar Energy Materials and Solar Cells*, vol. 132, pp. 640–649, Jan. 2015, doi: 10.1016/j.solmat.2014.10.026.
- [37] L. Granados *et al.*, 'Direct Determination of Total Hemispherical Emittance of Perovskite and Silicon Solar Cells', *Cell Reports Physical Science*, vol. 1, no. 1, p. 100008, Jan. 2020, doi: <https://doi.org/10.1016/j.xcrp.2019.100008>.
- [38] F. Arya, R. Moss, T. Hyde, S. Shire, P. Henshall, and P. Eames, 'Vacuum enclosures for solar thermal panels Part 2: Transient testing with an uncooled absorber plate', *Solar Energy*, vol. 174, pp. 1224–1236, Nov. 2018, doi: 10.1016/j.solener.2018.10.063.
- [39] V. Esen, Ş. Sağlam, and B. Oral, 'Solar Irradiation Fundamentals and Solar Simulators', in *A Practical Guide for Advanced Methods in Solar Photovoltaic Systems*, A. Mellit and M. Benghaneim, Eds. Cham: Springer International Publishing, 2020, pp. 3–28. doi: 10.1007/978-3-030-43473-1\_1.
- [40] International Electrotechnical Commission, *IEC 60904-9:2020 Photovoltaic devices - Part 9: Classification of solar simulator characteristics*. 2020. [Online]. Available: <https://webstore.iec.ch/publication/28973>
- [41] X. Dong, Z. Sun, G. J. Nathan, P. J. Ashman, and D. Gu, 'Time-resolved spectra of solar simulators employing metal halide and xenon arc lamps', *Solar Energy*, vol. 115, pp. 613–620, May 2015, doi: 10.1016/j.solener.2015.03.017.
- [42] G. Dibowski and K. Esser, 'Hazards Caused by UV Rays of Xenon Light Based High Performance Solar Simulators', *Safety and Health at Work*, vol. 8, no. 3, pp. 237–245, Sep. 2017, doi: 10.1016/j.shaw.2016.12.002.
- [43] L. Martínez-Manuel *et al.*, 'A 17.5 kWel high flux solar simulator with controllable flux-spot capabilities: Design and validation study', *Solar Energy*, vol. 170, pp. 807–819, Aug. 2018, doi: 10.1016/j.solener.2018.05.088.
- [44] A. M. Bazzi, Z. Klein, M. Sweeney, K. P. Kroeger, P. S. Shenoy, and P. T. Krein, 'Solid-State Solar Simulator', *IEEE Trans. on Ind. Applicat.*, vol. 48, no. 4, pp. 1195–1202, Jul. 2012, doi: 10.1109/TIA.2012.2199071.
- [45] G. Grandi, A. Ienina, and M. Bardhi, 'Effective Low-Cost Hybrid LED-Halogen Solar Simulator', *IEEE Trans. on Ind. Applicat.*, vol. 50, no. 5, pp. 3055–3064, Sep. 2014, doi: 10.1109/TIA.2014.2330003.

- [46] M. Tavakoli, F. Jahantigh, and H. Zarookian, 'Adjustable high-power-LED solar simulator with extended spectrum in UV region', *Solar Energy*, p. S0038092X20305818, Jun. 2020, doi: 10.1016/j.solener.2020.05.081.
- [47] E. Lopez-Fraguas, J. M. Sanchez-Pena, and R. Vergaz, 'A Low-Cost LED-Based Solar Simulator', *IEEE Trans. Instrum. Meas.*, vol. 68, no. 12, pp. 4913–4923, Dec. 2019, doi: 10.1109/TIM.2019.2899513.
- [48] A. Y. Al-Ahmad *et al.*, 'Modular LED arrays for large area solar simulation', *Prog Photovolt Res Appl*, vol. 27, no. 2, pp. 179–189, Feb. 2019, doi: 10.1002/pip.3072.
- [49] R. W. Moss, G. S. F. Shire, P. C. Eames, P. Henshall, T. Hyde, and F. Arya, 'Design and commissioning of a virtual image solar simulator for testing thermal collectors', *Solar Energy*, vol. 159, pp. 234–242, Jan. 2018, doi: 10.1016/j.solener.2017.10.044.
- [50] M. Y. Soh, T. H. Teo, W. X. Ng, and K. S. Yeo, 'Review of High Efficiency Integrated LED lighting', p. 5, 2017.
- [51] Wood, D., *Optoelectronic semiconductor devices; Prentice-Hall international series in optoelectronics, Prentice Hall PTR*, 1994, 3rd ed. Boston: McGraw-Hill, 2003.
- [52] CREE, 'CREE XLamp CXA3590 LED', *XLampQR CXA3590 LED Datasheet.*, 2014. [www.cree.com/XLamp](http://www.cree.com/XLamp)
- [53] Mean Well, 'Mean Well LED Driver ELG-200-C-S1750B'. 2020. [Online]. Available: <https://www.meanwell-web.com/content/files/pdfs/productPdfs/MW/ELG-200-C/ELG-200-C-spec.pdf>
- [54] Analog Device, 'Precision Thermocouple Amplifiers with Cold Junction Compensation', *Datasheet*, 2018. [www.analog.com/media/en/technical-documentation/data-sheets/ad8494/8495/8496/8497.pdf](http://www.analog.com/media/en/technical-documentation/data-sheets/ad8494/8495/8496/8497.pdf)
- [55] ARCTIC, 'Alpine 11 PLUS', *Cooler description*, 2011. [https://www.arctic.ac/eu\\_en/alpine-11-plus.html](https://www.arctic.ac/eu_en/alpine-11-plus.html)
- [56] C. D'Alessandro *et al.*, 'Low cost high intensity LED illumination device for high uniformity solar testing', *Solar Energy*, vol. 221, pp. 140–147, Jun. 2021, doi: 10.1016/j.solener.2021.04.017.
- [57] H. Masuda and M. Higano, 'Transient calorimetric technique for measuring total hemispherical emissivities of metals with rigorous evaluation of heat loss through thermocouple leads', *J. Opt. Soc. Am. A*, vol. 2, no. 11, p. 1877, Nov. 1985, doi: 10.1364/JOSAA.2.001877.
- [58] Z. Y. Nuru, D. E. Motaung, K. Kaviyarasu, and M. Maaza, 'Optimization and preparation of Pt–Al<sub>2</sub>O<sub>3</sub> double cermet as selective solar absorber coatings', *Journal of Alloys and Compounds*, vol. 664, pp. 161–168, Apr. 2016, doi: 10.1016/j.jallcom.2015.12.201.
- [59] R. Kumar and S. Kumar Verma, 'Review based on the absorber plate coating for solar air heater applications', *IOP Conf. Ser.: Mater. Sci. Eng.*, vol. 1116, no. 1, p. 012053, Apr. 2021, doi: 10.1088/1757-899X/1116/1/012053.
- [60] K. G. Ramanathan and S. H. Yen, 'High-temperature emissivities of copper, aluminum, and silver', *J. Opt. Soc. Am.*, vol. 67, no. 1, p. 32, Jan. 1977, doi: 10.1364/JOSA.67.000032.
- [61] H. C. Barshilia, N. Selvakumar, K. S. Rajam, and A. Biswas, 'Structure and optical properties of pulsed sputter deposited Cr<sub>x</sub>O<sub>y</sub>/Cr/Cr<sub>2</sub>O<sub>3</sub> solar selective coatings', *Journal of Applied Physics*, vol. 103, no. 2, p. 023507, Jan. 2008, doi: 10.1063/1.2831364.
- [62] W.-X. Zhou *et al.*, 'Nano-Cr-film-based solar selective absorber with high photo-thermal conversion efficiency and good thermal stability', *Opt. Express*, vol. 20, no. 27, p. 28953, Dec. 2012, doi: 10.1364/OE.20.028953.

- [63] F.-D. Lai and W.-Y. Li, 'SiO<sub>2</sub>/Ti/SiO<sub>2</sub> Three-layer Films Used as Solar Selective Absorber Layer in Heat Energy Collector', *Integrated Ferroelectrics*, vol. 145, no. 1, pp. 158–164, Jan. 2013, doi: 10.1080/10584587.2013.789289.
- [64] S. Abedini Dereshgi, A. Ghobadi, H. Hajian, B. Butun, and E. Ozbay, 'Ultra-Broadband, Lithography-Free, and Large-Scale Compatible Perfect Absorbers: The Optimum Choice of Metal layers in Metal-Insulator Multilayer Stacks', *Sci Rep*, vol. 7, no. 1, p. 14872, Dec. 2017, doi: 10.1038/s41598-017-13837-8.
- [65] F.-D. Lai, 'Effect of the thickness of the individual layers in Al<sub>2</sub>O<sub>3</sub>/Pt/Al<sub>2</sub>O<sub>3</sub> solar absorber films on the photo-thermal conversion efficiency for rapid industrial production', *Surface and Coatings Technology*, vol. 389, p. 125503, May 2020, doi: 10.1016/j.surfcoat.2020.125503.
- [66] Y. Tian, X. Liu, A. Ghanekar, and Y. Zheng, 'Scalable-manufactured metal–insulator–metal based selective solar absorbers with excellent high-temperature insensitivity', *Applied Energy*, vol. 281, p. 116055, Jan. 2021, doi: 10.1016/j.apenergy.2020.116055.
- [67] C.-D. Wen and I. Mudawar, 'Modeling the effects of surface roughness on the emissivity of aluminum alloys', *International Journal of Heat and Mass Transfer*, vol. 49, no. 23–24, pp. 4279–4289, Nov. 2006, doi: 10.1016/j.ijheatmasstransfer.2006.04.037.
- [68] L. De Los Santos Valladares *et al.*, 'Crystallization and electrical resistivity of Cu<sub>2</sub>O and CuO obtained by thermal oxidation of Cu thin films on SiO<sub>2</sub>/Si substrates', *Thin Solid Films*, vol. 520, no. 20, pp. 6368–6374, Aug. 2012, doi: 10.1016/j.tsf.2012.06.043.
- [69] S.-K. Lee, H.-C. Hsu, and W.-H. Tuan, 'Oxidation Behavior of Copper at a Temperature below 300 °C and the Methodology for Passivation', *Mat. Res.*, vol. 19, no. 1, pp. 51–56, Feb. 2016, doi: 10.1590/1980-5373-MR-2015-0139.
- [70] D. J. Elliott, 'Annealing and Planarizing', in *Ultraviolet Laser Technology and Applications*, Elsevier, 1995, pp. 209–250. doi: 10.1016/B978-0-12-237070-0.50011-X.
- [71] S. Bull, 'Techniques for improving thin film adhesion', *Vacuum*, vol. 43, no. 5–7, pp. 517–520, May 1992, doi: 10.1016/0042-207X(92)90068-8.
- [72] P. E. Ciddor, 'Refractive index of air: new equations for the visible and near infrared', *Appl. Opt.*, vol. 35, no. 9, p. 1566, Mar. 1996, doi: 10.1364/AO.35.001566.
- [73] L. Gao, F. Lemarchand, and M. Lequime, 'Exploitation of multiple incidences spectrometric measurements for thin film reverse engineering', *Opt. Express*, vol. 20, no. 14, p. 15734, Jul. 2012, doi: 10.1364/OE.20.015734.
- [74] M. F. Al-Kuhaili and S. M. A. Durrani, 'Optical properties of chromium oxide thin films deposited by electron-beam evaporation', *Optical Materials*, vol. 29, no. 6, pp. 709–713, Feb. 2007, doi: 10.1016/j.optmat.2005.11.020.
- [75] A. D. Rakić, A. B. Djurišić, J. M. Elazar, and M. L. Majewski, 'Optical properties of metallic films for vertical-cavity optoelectronic devices', *Appl. Opt., AO*, vol. 37, no. 22, pp. 5271–5283, Aug. 1998, doi: 10.1364/AO.37.005271.
- [76] D. Tahir and S. Tougaard, 'Electronic and optical properties of Cu, CuO and Cu<sub>2</sub>O studied by electron spectroscopy', *J. Phys.: Condens. Matter*, vol. 24, no. 17, p. 175002, May 2012, doi: 10.1088/0953-8984/24/17/175002.
- [77] M. A. Ordal, R. J. Bell, R. W. Alexander, L. L. Long, and M. R. Querry, 'Optical properties of fourteen metals in the infrared and far infrared: Al, Co, Cu, Au, Fe, Pb, Mo, Ni, Pd, Pt, Ag, Ti, V, and W', *Appl. Opt.*, vol. 24, no. 24, p. 4493, Dec. 1985, doi: 10.1364/AO.24.004493.
- [78] P. Khwansungnoen, T. Chaiyakun, S. Suwanboon, and T. Rattana, 'The influence of nitrogen partial pressure on visible-light-driven photocatalytic activity of sputtered

- titanium oxynitride thin films', *Vacuum*, vol. 193, p. 110540, Nov. 2021, doi: 10.1016/j.vacuum.2021.110540.
- [79] C. L. Arnold *et al.*, 'Composition, dielectric breakdown, and bandgap of ultra-thin amorphous boron oxynitride produced by magnetron sputtering', *Vacuum*, vol. 188, p. 110211, Jun. 2021, doi: 10.1016/j.vacuum.2021.110211.
- [80] K. Strijckmans, R. Schelfhout, and D. Depla, 'Tutorial: Hysteresis during the reactive magnetron sputtering process', *Journal of Applied Physics*, vol. 124, no. 24, p. 241101, Dec. 2018, doi: 10.1063/1.5042084.
- [81] G. Contoux, F. Cosset, A. Célérier, and J. Machet, 'Deposition process study of chromium oxide thin films obtained by d.c. magnetron sputtering', *Thin Solid Films*, vol. 292, no. 1–2, pp. 75–84, Jan. 1997, doi: 10.1016/S0040-6090(96)08941-9.
- [82] 'KME - Engineering Copper Solutions'. <https://www.kme.com>
- [83] K. H. Guenther, 'Physical and chemical aspects in the application of thin films on optical elements', *Appl. Opt.*, vol. 23, no. 20, p. 21, Oct. 1984, doi: doi.org/10.1364/AO.23.003612.
- [84] B. Carlsson, K. Moeller, U. Frei, and M. Koehl, 'Accelerated life testing of solar absorber coatings', Freiburg, Federal Republic of Germany, Sep. 1994, pp. 79–90. doi: 10.1117/12.185359.
- [85] C. Loka, 'Preparation of TiO<sub>2</sub>/Ag/TiO<sub>2</sub> (TAT) multilayer films with optical and electrical properties enhanced by using Cr-added Ag film', *Applied Surface Science*, p. 8, 2017.
- [86] M. Köhl, M. Heck, S. Brunold, U. Frei, B. Carlsson, and K. Möller, 'Advanced procedure for the assessment of the lifetime of solar absorber coatings', *Solar Energy Materials and Solar Cells*, vol. 84, no. 1–4, pp. 275–289, Oct. 2004, doi: 10.1016/j.solmat.2004.01.041.
- [87] A. Caldarelli *et al.*, 'Characterization and thermal aging tests of Cr based multilayer for unconcentrated solar thermal applications', *Thin Solid Films*, vol. 735, p. 138870, Oct. 2021, doi: 10.1016/j.tsf.2021.138870.
- [88] European Commission, 'Photovoltaic Geographical Information System', [https://re.jrc.ec.europa.eu/pvg\\_tools/it/#DR](https://re.jrc.ec.europa.eu/pvg_tools/it/#DR), 2021. [https://re.jrc.ec.europa.eu/pvg\\_tools/it/#DR](https://re.jrc.ec.europa.eu/pvg_tools/it/#DR) (accessed Oct. 01, 2021).
- [89] 'Chapter 4 The planar magnetron', in *Thin Films*, vol. 26, Elsevier, 1999, pp. 87–101. doi: 10.1016/S1079-4050(99)80007-6.
- [90] S. Belikov, 'Constrained optimization of rotating magnetron in low-pressure plasma sputtering', in *2013 American Control Conference*, Washington, DC, Jun. 2013, pp. 6661–6666. doi: 10.1109/ACC.2013.6580885.
- [91] D. L. Windt, 'IMD—Software for modeling the optical properties of multilayer films', *American Institute of Physics*, 1998, [Online]. Available: <https://aip.scitation.org/doi/abs/10.1063/1.168689>
- [92] G. Hass and C. D. Salzberg, 'Optical Properties of Silicon Monoxide in the Wavelength Region from 0.24 to 140 Microns\*', *J. Opt. Soc. Am.*, vol. 44, no. 3, p. 181, Mar. 1954, doi: 10.1364/JOSA.44.000181.
- [93] M. A. Green, 'Self-consistent optical parameters of intrinsic silicon at 300K including temperature coefficients', *Solar Energy Materials and Solar Cells*, vol. 92, no. 11, pp. 1305–1310, Nov. 2008, doi: 10.1016/j.solmat.2008.06.009.